# Development of an X-ray prism for a combined diffraction enhanced imaging and fluorescence imaging system

A Thesis Submitted to the College of

Graduate Studies and Research

in the Partial Fulfillment of the Requirements

for the Degree of Doctor of Philosophy

in the

Department of Physics and Engineering Physics

University of Saskatchewan

Saskatoon

by

**Brian E. Bewer**

Saskatoon, SK

Canada

To my loving wife Amanda.

Your unwavering support through the years of my Ph.D. gave me much needed

inspiration and hope.

# Abstract

Analyzer crystal based imaging techniques such as diffraction enhanced imaging (DEI) and multiple imaging radiography (MIR) utilize the Bragg peak of perfect crystal diffraction to convert angular changes into intensity changes. These X-ray techniques extend the capability of conventional radiography, which derives image contrast from absorption, by providing a large change in intensity for a small angle change introduced by the X-ray beam traversing the sample. Objects that have very little absorption contrast may have considerable refraction and ultra small angle X-ray scattering (USAXS) contrast thus improving visualization and extending the utility of X-ray imaging. To improve on the current DEI technique this body of work describes the design of an X-ray prism (XRP) included in the imaging system which allows the analyzer crystal to be aligned anywhere on the rocking curve without moving the analyzer from the Bragg angle. By using the XRP to set the rocking curve alignment rather than moving the analyzer crystal physically the needed angle sensitivity is changed from $\mu$radians for direct mechanical movement of the analyzer crystal to milliradian control for movement the XRP angle. In addition to using an XRP for the traditional DEI acquisition method of two scans on opposite sides of the rocking curve preliminary tests will be presented showing the potential of using an XRP to scan quickly through the entire rocking curve. This has the benefit of collecting all the required data for image reconstruction in a single fast measurement thus removing the occurrence of motion artifacts for each point or line used during a scan. The XRP design is also intended to be compatible with combined imaging systems where more than one technique is used to investigate a sample. Candidates for complimentary techniques are investigated and measurements from a combined X-ray imaging system are presented.

# Contents

# List of Figures

xiv

# List of Tables

# List of Abbreviations

| | |
|---|---|
| ABI | Analyzer Based Imaging |
| BMIT | Biomedical Imaging and Therapy Beamline |
| CLS | Canadian Light Source |
| CR | Computed Radiography |
| DAQ | Data Acquisition System |
| DCM | Double Crystal Monochromator |
| DEI | Diffraction Enhanced Imaging |
| FI | Fluorescence Imaging |
| FSI | Fluorescence Subtraction Imaging |
| FWHM | Full Width at Half Maximum |
| GEMS | Gene Expression Mapping Using Synchrotron Light |
| GFP | Green Fluorescent Protein |
| IDL | Interactive Data Language |
| KES | K-Edge Subtraction |
| LabVIEW | Laboratory Virtual Instrumentation Engineering Workbench |
| MIR | Multiple Image Radiography |
| NEMA | National Electrical Manufacturers Association |
| NIM | Nuclear Instrumentation Module |
| PID | Proportional Integral Derivative |
| PMMA | Polymethyl Methacrylate |
| POE | Primary Optical Enclosure |
| RMS | Root Mean Square |
| SAXS | Small Angle X-ray Scattering |
| SCA | Single Channel Analyzer |
| SyLMAND | Synchrotron Laboratory for Micro And Nano Devices |
| USAXS | Ultra Small Angle X-ray Scattering |
| VTF | Voltage To Frequency |
| WAXS | Wide Angle X-ray Scattering |
| XRP | X-Ray Prism |

# Chapter 1

# Introduction

## 1.1  Overview

Analyzer crystal based imaging techniques such as diffraction enhanced imaging (DEI) and multiple imaging radiography (MIR) utilize the Bragg peak of perfect crystal diffraction to convert angular changes into intensity changes. These X-ray techniques extend the capability of conventional radiography, which derives image contrast from absorption, by providing a large change in intensity for a small angle change introduced by the X-ray beam traversing the sample. Objects that have very little absorption contrast may have considerable refraction and ultra small angle X-ray scattering (USAXS) contrast thus improving visualization and extending the utility of X-ray imaging [Cha97, Wer03]. Applications of this method to biology and engineering have generated impressive gains in contrast indicating potential for use in medical imaging [Cha98; Pis00; Mue04; Li04; Con05]. To improve on the current DEI technique a new method of changing crystal angle alignment is needed which does not depend on moving an aligned crystal by direct mechanical control. A further improvement to DEI and MIR techniques would have all the requisite positions

on the rocking curve acquired in a single rapid measurement so that motion artifacts from separate scans at specific locations on the rocking curve are removed.

Unlike conventional attenuation based imaging which counts the number of X-rays that pass through an object and reach a detector element, the DEI method provides additional contrast by also determining the angle associated with the X-ray path when counted by the detector. All analyzer based imaging methods achieve X-ray angle sensitivity by using two or more crystals of the same material and lattice plane orientation. The first crystal (or crystals) chooses the X-ray energy that will be used in imaging and places a limit on the spread of angles that the X-ray beam may have (i.e. there is a bandwidth associated with crystal diffraction $\frac{\Delta\lambda}{\lambda}$ which implies a range of possible diffraction angles through Bragg's Law). The analyzer crystal (or crystals) is placed after the monochromator and object of interest and is of the same type as the monochromator crystal. It has the same energy bandwidth and range of angles if it is oriented to the same Bragg angle setting as the monochromator crystal. Consider any Bragg angle setting of the monochromator for a chosen wavelength $\lambda$. The range of X-ray diffraction angles is given by the reflectivity of the crystal. To get X-rays to a detector positioned after the analyzer crystal it is necessary to have the Bragg angle of the analyzer crystal set so that the possible diffraction angles of this crystal overlap with some or all of the angles allowed by the monochromator crystal. It is convenient to visualize the angle ranges of each crystal and how an object between the crystals could increase or decrease the amount of overlap by causing a refraction angle deviation in terms of a Venn diagram (See figure 1.1). By using the reflectivity of a crystal to vary the probability that an X-ray will arrive at the detector for a given angle, additional contrast is achieved in a DEI image beyond expected attenuation effects.
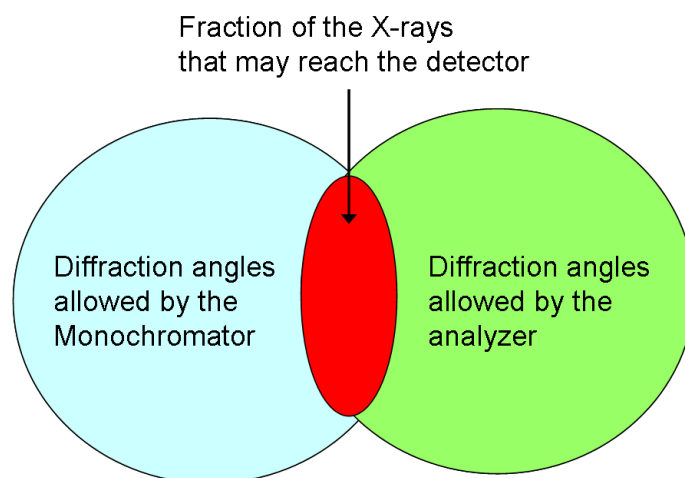
Figure 1.1: The Bragg angle setting of the monochromator and the Bragg angle setting of the analyzer each creates a range of angles for the respective crystals for which X-ray diffraction is allowed. For any X-rays to arrive at the detector after both crystals there must be overlap in the range of angles. Maximum intensity is achieved if both ranges completely overlap. If the crystals are aligned so there is only partial overlap it is possible for an object to cause refraction angle deviations that will cause addition overlap in one direction and less overlap in the other. This would cause measured intensity variations and contrast in the resulting image.

## 1.2   Objectives

The goal of the research presented is to investigate the improvements in technical capabilities of a DEI or MIR system by adding an X-ray prism (XRP) in the shape of a half cylinder for the application of biological and materials imaging, and the possibility of combining this new system with other forms of X-ray imaging such as Wide Angle X-ray Scattering (WAXS) or Fluorescence Imaging (FI). A successful XRP design must be able to replace the current tangent arm DEI setup with the following improvements: 1) the new setup must be light and easy to move to locations in the experimental hutch; 2) the XRP must be a bench top sized unit that does not require significant space; and 3) additional angle alignment sensitivity is desirable, but no loss in alignment resolution for the crystal angle is tolerable.

The first objective will be to determine the design parameters of the XRP which includes: 1) building materials; 2) tolerable absorption loss; 3) angle range of the refraction deviation; and 4) the geometry of the XRP. This will require use of theoretical principals to predict how the XRP will perform and adjust the design parameters to achieve a usable system.

The second objective will be to program motion control and data acquisition systems capable of performing the tasks necessary to complete the desired measurements. The system must be able to move several motors simultaneously for object and detector, record several scalar channels from reference ion chambers, and be capable of triggering external hardware and the opening and closing of shutters.

The third objective will be to test the finished XRP to determine if it performs to the intended specifications. This will involve confirming the absorption of the X-ray beam by the XRP and the magnitude of refraction deviation caused by the XRP at a variety of orientations using the BioMedical Imaging and Therapy (BMIT) beamline at the Canadian Light Source (CLS) .

The fourth objective will be to investigate the possibility of integrating the XRP version of a DEI system with other types of X-ray imaging like K-edge subtraction (KES), WAXS, and FI.

The fifth objective will be to test the rapid scanning potential of the XRP by measuring the whole rocking curve of a crystal reflection. A subsequent measurement could then be performed to look at the differences in the measured rocking curve

when phantom samples are inserted into the X-ray beam to mimic different levels of absorption and scattering.

The final objective will be to use the XRP in a combined imaging system and perform a test with a phantom sample.

## 1.3 Organization

The second chapter will focus on the interactions of photons with matter. An understanding of these theoretical properties will be required to predict the performance of the XRP. The third chapter will provide a review of sources of X-rays including X-ray tubes and synchrotron sources. An understanding of the source of X-rays will be necessary to determine the number of available photons and the dose to the sample. The fourth chapter will cover the esoteric physical principles of DEI and how absorption, refraction, and USAXS images are calculated. The fifth chapter will describe the early work during the development of the data acquisition system (DAQ) and motion control. The sixth chapter will describe WAXS tests performed at the BMIT beamline to determine if this imaging method could be combined with DEI. The seventh chapter will describe the commissioning process of the DEI system and test measurements to ensure it functioned properly. The eighth chapter will describe the XRP design, construction, and trial measurements. The ninth chapter will describe the combined DEI and FI apparatus and the first measurements conducted. The final chapter will be a discussion of the project results with comments made on future work.

# Chapter 2

# Interactions of Photons with Matter

## 2.1 The Photoelectric Effect

First discovered by Heinrich Rudolph Hertz in 1887 the photoelectric effect is the process by which an incident electromagnetic wave is absorbed by an electron causing the emission of that electron from the atom. Hertz observed that ultraviolet light affects the voltage at which sparking occurs between electrodes, however, the kinetic energy of the emitted electrons was not a function of the intensity of the incident light as was expected at the time. Philipp Lenard, an assistant to Hertz, performed a series of experiments that demonstrated conclusively that the kinetic energy of the electrons was independent of the intensity of the incident light [Nob67]. In 1905 Einstein proposed his theory of the photoelectric effect, which introduced the idea that light travels in packets, or quanta. Einstein proposed that the frequency of these individual quanta, or photons, determined the energy of the photoelectrons ejected from the atom (See figure 2.1). The energy of each quanta was defined by

the equation, $E = hf$, where h is Plank's constant, and f is the frequency of the photon. Increasing the number of photons that are incident on a surface will increase the number of photoelectrons that are emitted, but not the kinetic energy of the emitted electron. To increase the kinetic energy of the photoelectron the frequency of the incident photon must be increased. Einstein's theory of the photoelectric effect correctly described this natural phenomenon and he was awarded the Nobel Prize in Physics in 1921 [Nob67].
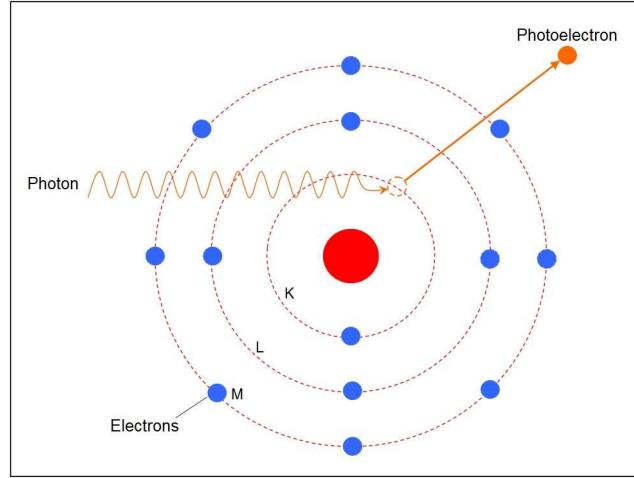


Figure 2.1: Diagram of the photoelectric effect. An incident photon is completely absorbed by an inner shell electron, which is freed from the atom with a kinetic energy equaling the incident photon energy minus the atomic binding energy.

The probability of photoelectric absorption occurring per unit mass is proportional to $Z^3/E^3$, where Z is the atomic number and E is the energy of the incident photon, except at the electron shell binding energies (e.g. $K_{1s}$) [Bus02]. The photoelectric process is the dominant contrast mechanism in conventional radiography. The number of photons absorbed may be calculated using Beer's Law, $I = I_o \exp(-\mu l)$, where I is the remaining number of photons after absorption, $I_o$ is the incident number of photons, $\mu$ is the linear attenuation coefficient of the absorber, and l is the path length through the absorber [Bee65]. The contrast in the limit of weak absorption

of an embedded object is equal to $C = (\frac{\mu}{\rho_o}\rho_o - \frac{\mu}{\rho_m}\rho_m)t_o$, where $\frac{\mu}{\rho_o}$ is the mass at-

tenuation coefficient of the embedded object, $\rho_o$ is the density of the object, $t_o$ is

the thickness of the embedded object, $\frac{\mu}{\rho_m}$ is the mass attenuation coefficient of the

surrounding material, and $\rho_m$ is the density of the surrounding material.
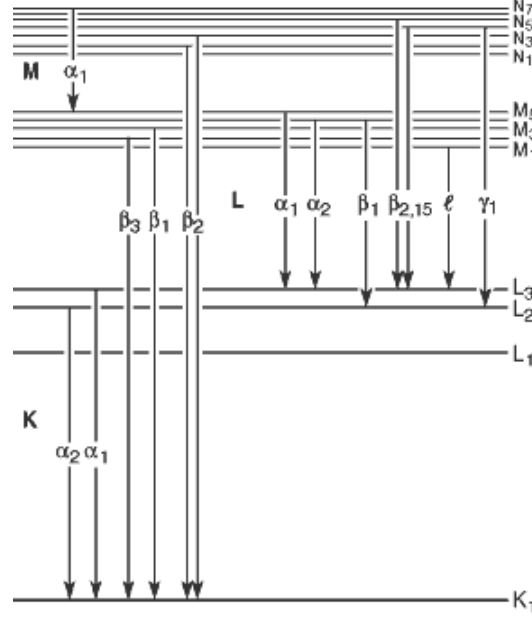


Figure 2.2: Electron transitions [Tho01].

By definition the byproducts of the photoelectric effect are ionized atoms making

exposure during radiological procedures a concern due to the health risks associated

with ionizing radiation and free radical formation. An additional result of photoelec-

tric absorption is fluorescence. The vacancy that is created with the escape of the

photoelectron from the atom is filled by an electron transitioning from a higher shell

(See figure 2.2). During the electron transition between shells a fluorescence photon

may be emitted with energy equal to the binding energy difference between the two

states and is emitted isotropically, or the electronic transition may result in further

ionization of the atom where more electrons are emitted and is called the Auger

effect [Hen02]. The probability of fluorescence is described by the fluorescence yield. Since electron binding energies are determined by the nuclear charge, fluorescence photons are unique for each element.

## 2.2 Inelastic Scattering

Inelastic scattering was first described by Arthur Compton in 1922. Compton observed an increase in wavelength of X-rays due to scattering of incident radiation by free electrons. The implication of this observation is that the scattered quanta have less energy than the quanta in the original beam. Arthur Compton was awarded the 1927 Nobel Prize in Physics for his work leading to the understanding of this process. A Compton scattering event can be described as a collision between an X-ray and an electron in the outer shell of an atom. The electron binding energy of outer electrons is minimal allowing the electron to be approximated as free ($E_{photon} \gg E_{binding\ energy}$). In this case the energy lost by the photon during the interaction with the electron is given to the electron as kinetic energy. This transfer of energy results in a photon with decreased energy, or increased wavelength, and the ejection of the impacted electron from the atom (See figure 2.3).

The Compton scattering equation used to calculate the change in wavelength is given by equation 2.1.

$$\lambda' - \lambda = \frac{hc}{m_e c^2}(1 - cos(\Theta))$$

(2.1)
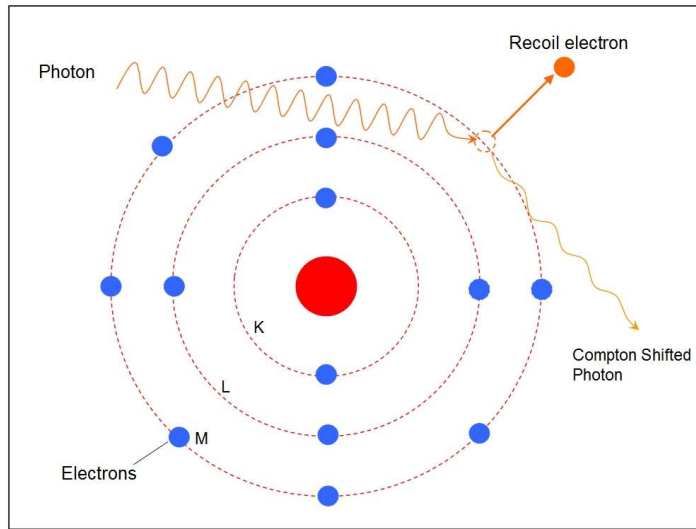
Figure 2.3: Diagram of Compton Scattering. An incident X-ray collides with an outer shell electron and transfers energy to the electron. A photon equal in energy to the difference of the original X-ray and the kinetic energy acquired by the electron emerges from the location of scatter with a different direction.

Where $\lambda$ is the incident photon wavelength, $\lambda'$ is the scattered photon wavelength, h is Plank's constant, $m_e$ the mass of the electron, c is the speed of light, and $\Theta$ the angle between the incident photon direction and the scattered photon direction.

There are no current clinical imaging methods based on Compton scatter, but it is an important component along with the photoelectric effect when determining the dose delivered to an object. In medical imaging procedures the Compton effect accounts for most of the scattering that occurs.

## 2.3   Elastic Scattering

Interactions that occur without a transfer of energy are elastic, and X-ray interactions that occur without an associated loss of energy in the incident photon are referred to as elastic scatter. In an elastic scattering event, the energy of the primary X-

ray photon is first completely absorbed and then re-emitted by oscillating atomic electrons (See figure 2.4). The direction of the re-radiated photons is not isotropic, with the forward angles being more probable. It is the elastic scattering effect that is responsible for the diffraction of X-rays from crystals.
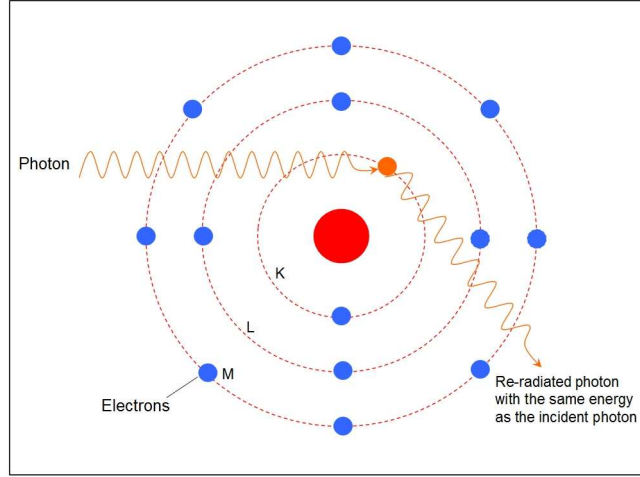


Figure 2.4: Diagram of Coherent Scattering. An X-ray is absorbed and re-radiated by the oscillating electric field of atomic electrons.

## 2.4   Refraction

The refraction of light as it passes from one medium to another was first described by Willebrord Snell, and the law that defines this process is known at Snell's law. Mathematically, this relationship is defined as $n_1 \sin(\theta_1) = n_2 \sin(\theta_2)$, where $n_1$ and $n_2$ are the refractive indices of the two materials that form a surface boundary, and $\theta_1$ and $\theta_2$ are the angles from the surface normals (See figure 2.5).

If the boundary is between air and a second material the angle change predicted is calculated using the following approximations, $\sin(t) = t$, $\cos(t) = 1$ for $t \approx 0$ , and
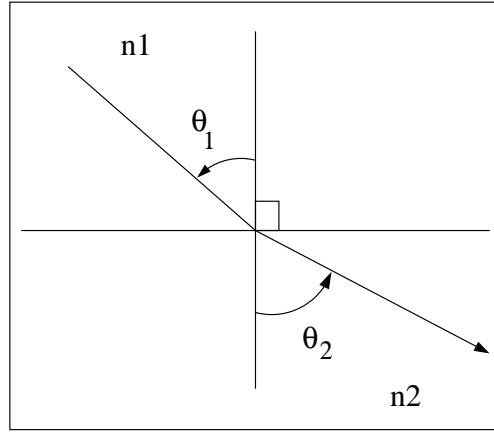
Figure 2.5: Refraction diagram of light at an interface of heterogeneous materials.

$(1 - n_{air}^{10-100keV} \ll 10^{-6})$

$$n \sin(\theta_r) = 1 \sin(\theta)$$

$$\Rightarrow (1 - \alpha)\sin(\theta + \Delta\theta) = \sin(\theta) \;\; ; \;\; \theta_r \equiv \theta + \Delta\theta$$

$$\Rightarrow (1 - \alpha)[\sin(\theta)\cos(\Delta\theta) + \sin(\Delta\theta)\cos(\theta)] = \sin(\theta)$$

$$\Rightarrow (1 - \alpha)[\sin(\theta) + \Delta\theta\cos(\theta)] = \sin(\theta)$$

$$\Rightarrow \sin(\theta) - \alpha\sin(\theta) - \alpha\Delta\theta\cos(\theta) + \Delta\theta\cos(\theta) = \sin(\theta)$$

$$\Rightarrow \Delta\theta\cos(\theta) = \alpha\sin(\theta)$$

$$\Rightarrow \Delta\theta = \alpha[\sin(\theta)/\cos(\theta)]$$

$$\Rightarrow \Delta\theta = \alpha \; \tan(\theta) \tag{2.2}$$

Where $\Delta\theta$ is the refraction angle, and $\alpha$ is the real part of the refractive index correction for the second material which is assumed to be small ($|\alpha| << 1$). The real part of the refractive index correction in the X-ray regime can be expressed as $\alpha = r_e\lambda^2\rho_e/2\pi$. Where $\rho_e$ is the electron density, $r_e$ is the classical electron radius, and $\lambda$ is the X-ray wavelength. The real part of the refractive index correction may be expressed in terms of the mass density by using the following substitution.

12

$$\rho = \frac{N_{atoms} \times A \times u_n}{V}$$

$$\Rightarrow \rho = \frac{N_{atoms} \times Z}{V} \times \frac{A \times u_n}{Z}$$

$$\Rightarrow \rho = \rho_e \times \frac{A \times u_n}{Z}$$

$$\Rightarrow \rho_e = \rho \times \frac{Z}{A \times u_n}$$

$$\alpha = \frac{r_e \lambda^2}{2\pi u_n} \frac{Z}{A} \rho \tag{2.3}$$

Where Z is the atomic number, A is the atomic mass, $\rho$ is the mass density, and $u_n$ the nucleon mass [Als01]. For X-rays in the diagnostic imaging regime the magnitude of alpha is on the $10^{-6} - 10^{-7}$ scale for low Z materials and has the opposite sign compared to visible light. A consequence of the negative real refractive index correction is that the angle deviation from refraction goes opposite to what would be expected for visible light (See figure 2.6).
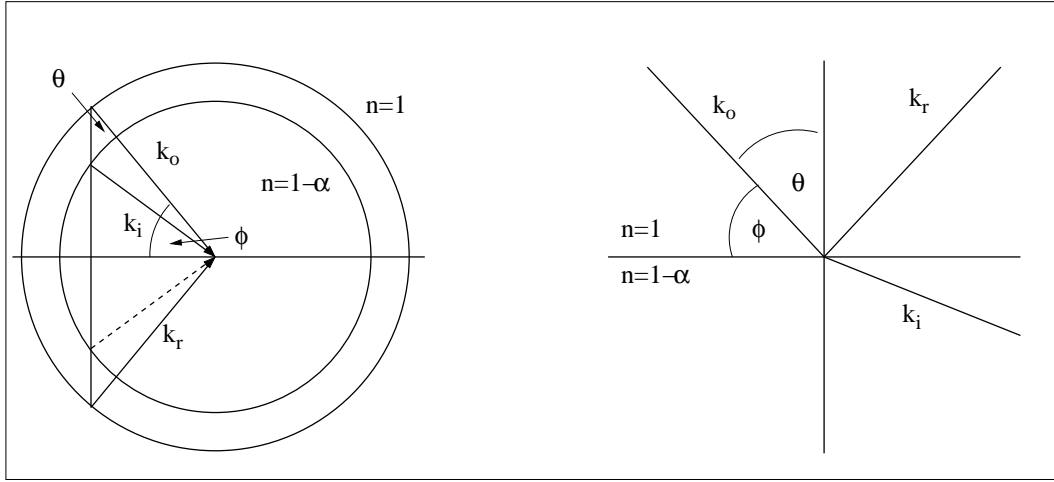


Figure 2.6: A dispersion surface diagram of refracting X-rays where the magnitude of the k vector is the radius of the respective circles. The diagram shows momentum conservation at a surface between two materials, where k $= \frac{2\pi}{\lambda}$, $k_o$ is the path of incident X-rays, $k_i$ is the path of refracted X-rays, and $k_r$ is the path of reflected X-rays.

# Chapter 3

# X-rays

## 3.1 X-ray production

Two sources of experimentally useful X-rays are X-ray tubes and synchrotrons. In either case the creation of X-rays come from the acceleration of electrons; either by electrons colliding with the anode in an X-ray tube creating bremßtrahlung radiation, or by the acceleration of highly relativistic electrons in a strong magnetic field in a synchrotron storage ring. Both have positive and negative attributes and will be briefly examined.

### 3.1.1 X-ray Tubes

X-rays were discovered by Wilhelm Conrad Röntgen while examining the light and other radiation associated with discharging electrodes in an evacuated glass tube. Using a fluorescent screen he was able to observe penetrating radiation that could go through paper and wood, but not metal. Even more importantly Röntgen was able to observe that these new higher energy rays could penetrate the soft tissues of the body, but not the bones. Replacing the fluorescent screen with film Röntgen

was able to capture a photograph of bones inside the human hand [Ron96].

In 1912 W.D. Coolidge from General Electric Research Laboratories developed the X-ray tube that would be the standard for decades. Electrons were produced from a glowing filament and accelerated by a high voltage towards a water cooled anode. The benefits of the new design were that the tube current and the accelerating voltage could be varied independently, and the intensity was limited only by the cooling efficiency. To increase the cooling efficiency in later X-ray tubes a rotating anode was included so that the power load was distributed over a larger area. This innovation increased the total power that the X-ray tube could produce, but did not come about until the 1960's. The delay was because a suitable vacuum tight seal that allowed a rotating shaft with water cooling lines needed to be engineered [Als01]. In figure 3.1 a diagram for a Coolidge tube and a later rotating anode X-ray tube are shown.
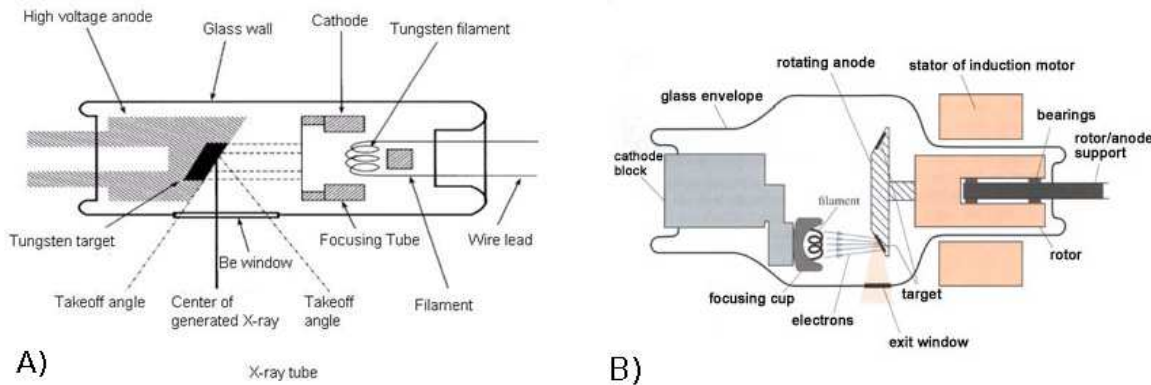
Figure 3.1: A) An early X-ray tube design. B) Design of a rotating anode X-ray tube.

The spectrum produced from energetic electrons impinging on an anode had two components, bremßtrahlung radiation, and anode element characteristic peaks. The bremßtrahlung radiation forms a continuous photon spectrum that has a high photon energy limit (in electron volts) ending at the accelerating high voltage value. Thus

for a 20kV accelerating voltage the highest photon energy produced would be 20keV. Within the continuous bremßtrahlung spectrum are characteristic peaks caused by incident electrons exciting inner shell atomic electrons creating a vacancy in a similar fashion as fluorescence described in section 2.1. The subsequent relaxation of an outer shell electron filling the vacancy produces a fluorescence X-ray unique to the anode material. Because all inner shell excitations are followed by only a few possible relaxation transitions intense peaks are produced in the X-ray spectrum at these fluorescence energies. Figure 3.2 shows a photon spectrum for a Molybdenum X-ray tube where the $K_\alpha$ and $K_\beta$ florescence energies are the most intense values above the continuous bremßtrahlung spectrum.
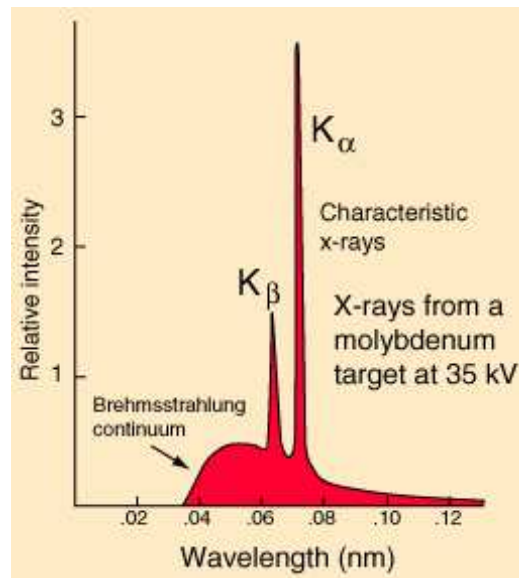


Figure 3.2: The continuous bremßtrahlung spectrum and fluorescence peaks from a Molybdenum X-ray tube [Opp05].

### 3.1.2 Synchrotron Sources

Synchrotron radiation, named after accelerators which synchronously changed magnetic field strength as electron energy was increased, refers to radiation caused by relativistic charged particles accelerated by a magnetic field (See figure 3.3). Synchrotron light was first reported in 1947 by General Electric's Research Laboratory using a 70MeV synchrotron with 0.81T peak magnetic field and 29.3cm orbit radius [Eld47]. In a 3rd generation storage ring synchrotron radiation not only comes from the bending magnets required to keep the electrons on a closed orbit, but from insertion devices such as wigglers and undulators that occupy straight sections in the storage ring. These devices have a repeating magnets with opposite polarity between adjacent magnets. The strength of the magnet and the path length through the magnetic field determine the defection of the electron beam and hence the resulting beam size. The most significant difference between the two types of devices is that undulators have coherence structure in the resulting energy spectrum where wigglers have a continuous spectrum of energies.

**Bending Magnet Beamlines**

Due to the relativistic energies of the electron, emitted radiation from the transverse acceleration caused by the magnetic field is forward focused. The radiation cone produced is defined by a $1/\gamma$ opening angle around the direction of motion, where $\gamma = 1/\sqrt{1 - \frac{\vec{v}^2}{c^2}}$, $\vec{v}$ is the velocity of the electron, and c is the speed of light in a vacuum (See figure 3.3). In a bending magnet the electron is swept through an arc creating a horizontal swath of radiation which has a $\sim 1/\gamma$ vertical opening angle. The photon flux from a bending magnet source in the plane of orbit expressed in

practical units is given by,

$$\frac{d^2\mathcal{F}_B}{d\theta d\psi}\bigg|_{\psi=0} = 1.327 \times 10^{13} E_r^2[\text{GeV}] I[\text{A}] H_2(y) \left[\frac{\text{photons}}{\text{s} \cdot \text{mr}^2 \cdot 0.1\% \text{ bandwidth}}\right] \quad (3.1)$$

where $E_r$ is the storage ring electron energy in GeV, I is the storage ring current in Amperes, $y = E_{ph}/E_c$ the photon energy of interest divided by the critical energy ($E_c[\text{keV}] = 0.665 \ E_r^2[\text{GeV}] B[\text{T}]$) with B equaling the magnetic field strength in Tesla, $H_2(y) = y^2 \ K_{2/3}^2(y/2)$ where $K_{2/3}$ is the K type Bessel function of 2/3 fractional order, $\theta$ horizontal angle measured from the direction of the electrons, and $\psi$ is the vertical angle measured from the direction of the electrons. [Tho01].

If the observation point is off the horizontal plane of orbit the photon flux from a bending magnet source is given by,

$$\frac{d^2\mathcal{F}_B}{d\theta d\psi} = 1.327 \times 10^{13} E_r^2[\text{GeV}] I[\text{A}] H(X, y) \left[\frac{\text{photons}}{\text{s} \cdot \text{mr}^2 \cdot 0.1\% \text{ bandwidth}}\right] \quad (3.2)$$

Where $H(X,y) = y^2(1 + X^2)^2 \left[K_{2/3}^2(\xi) + \frac{X^2}{1+X^2} K_{1/3}^2(\xi)\right]$, $X = \gamma\psi$, $\psi$ is the vertical angle from the orbital plane to the observation point, and $\xi = \frac{y}{2}(1 + X^2)^{3/2}$.

The vertically integrated flux over all angles of $\psi$ is proportional to $G_1(y) = y \int_y^\infty K_{5/3}(y')dy'$, where $K_{5/3}$ is the K type Bessel function of 5/3 fractional order. In practical units the vertically integrated flux is given by,

$$\frac{d\mathcal{F}_B}{d\theta} = 2.457 \times 10^{13} \ E^2[\text{GeV}] \ I[\text{A}] \ G_1(y) \left[\frac{\text{photons}}{\text{s} \cdot \text{mr} \cdot 0.1\% \text{ bandwidth}}\right] \quad (3.3)$$

For an energy of interest the angular width of the photon beam may be more precisely calculated than the $1/\gamma$ nominal width approximation in terms of the effective RMS

18

half-angle $\sigma_\psi$. Once this effective angle of divergence is known the photon flux may be calculated at any distance from the source of X-rays for a particular height above the orbital plane. In terms of equation 3.1 and equation 3.3 the effective RMS half-angle is given by [Tho01],

$$\frac{\mathrm{d}\mathcal{F}_\mathrm{B}}{\mathrm{d}\theta} \bigg/ \frac{\mathrm{d}^2\mathcal{F}_\mathrm{B}}{\mathrm{d}\theta\mathrm{d}\psi}\bigg|_{\psi=0} = \sqrt{2\pi}\sigma_\psi \qquad (3.4)$$
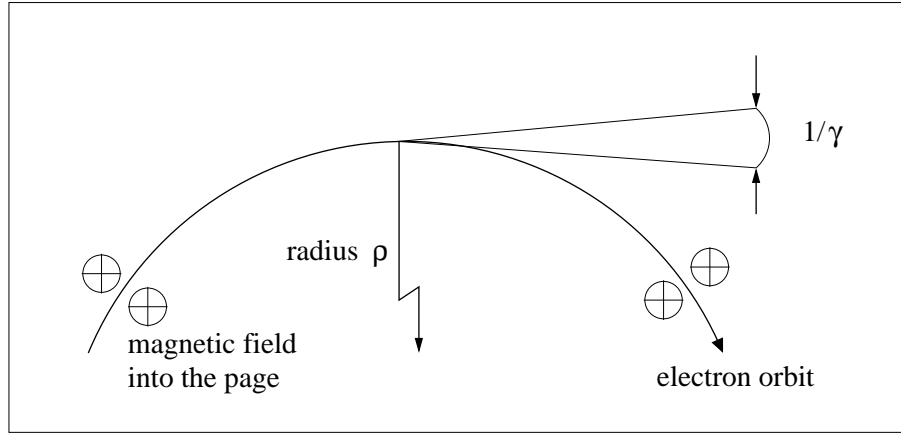


Figure 3.3: Diagram of an electron orbiting in a synchrotron storage ring and the $1/\gamma$ emission opening angle.

The power radiated by a bending magnet in practical units per horizontal angle is given by,

$$\frac{\mathrm{dP_B}}{\mathrm{d}\theta}[\mathrm{W/mr}] = 4.27\ \mathrm{E_r^3[GeV]\ B[T]\ A[I]} \qquad (3.5)$$

Where $\mathrm{E_r}$ is the storage ring electron energy in GeV, B is the bending magnet field strength in Tesla, and A is the current in the storage ring in Amperes [Tho01].

**Insertion Device Sources**

For insertion devices the K value defines the defection magnitude that an electron passing through the device would experience. Wigglers have larger K values and undulators have small K values ($K_{undulator} \approx 1$). For a magnetic period of $\lambda_u$, and a peak magnetic field strength of $B_o$, the deflection parameter K is given by $K = 0.934\lambda_u[cm]B_o[T]$. The opening angle of the emitted radiation in the plane of the electron orbit is $K/\gamma$ for wigglers and $1/\sqrt{N}\gamma$ for undulators, where N is the number of magnetic periods [Als01]. For both wigglers and undulators the vertical divergence of the emitted radiation is defined by a $1/\gamma$ opening angle as with bending magnets. For wigglers the photon flux may be calculated by multiplying the bending magnet formula by 2N, which is the number of magnetic poles. The observation angle does matter however, as the critical energy changes with the effective magnetic field that is at the source point of the X-rays being observed. The equation for how the critical energy changes with horizontal angle $\theta$ is given by equation 3.6.

$$E_c(\theta) = \sqrt{1 - \left(\frac{\theta}{K/\gamma}\right)^2} \tag{3.6}$$

Equation 3.5 can be used to incorporate the wiggler horizontal dependence into equations 3.1, 3.2, and 3.3 by redefining $y(\theta) \equiv \frac{E_{photon}}{E_c(\theta)}$. The power radiated by a periodic insertion device in practical units is given by,

$$P[kW] = 0.633 \; E_r^2[GeV] \; B_o^2[T] \; L[m] \; I[A]. \tag{3.7}$$

Where $E_r$ is the storage ring electron energy in GeV, $B_o$ is the bending magnet field strength in Tesla, L is the length of the undulator or wiggler ($N\lambda_u$), and A is the current in the storage ring in Amperes [Als01].

## 3.2 Ion Chambers

To confirm that the number of photons provided by the beamline matches the predicted value and to verify that the beamline is operating normally it is often necessary to measure the photon flux directly with an ion chamber. In the case where the ion chamber is measuring the incoming flux (i.e. $I_o$) a gas is chosen so that no more than a few percent of the beam is absorbed through the length of the ion chamber (See figure 3.4). If on the other hand the ion chamber is positioned at the back of the experiment to measure the transmission through a sample with the intent of Poisson statistics limited counting a gas would be chosen to stop as much of the beam as possible without causing a non-linear response.
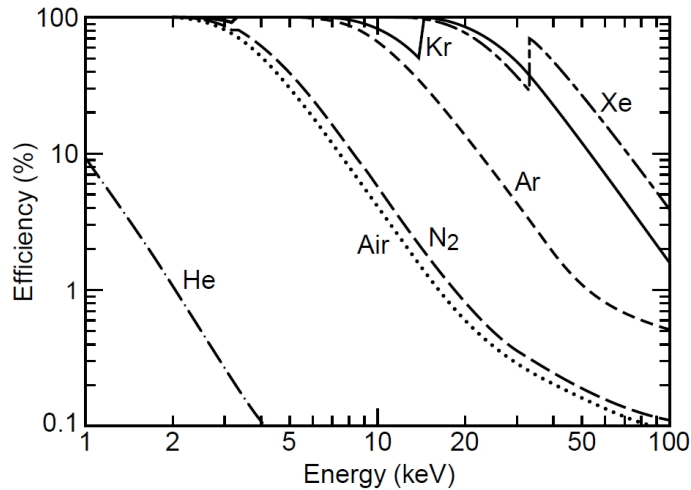


Figure 3.4: Absorption efficiency of a 10cm long gas ion chamber at normal pressure as a function of energy [Tho01].

For each gas and photon energy an ion chamber will have a unique value for the num-

ber of Coulombs of charge created in the chamber per photon that will be denoted as $\xi$. The value of $\xi$ is calculated by,

$$\xi = q_e \frac{E_o}{E_{ion}} \frac{\frac{\mu(E_o)}{\rho_{EA}}}{\frac{\mu(E_o)}{\rho_T}} \left(1 - \exp\left(-\frac{\mu(E_o)}{\rho_T}\rho L\right)\right) \tag{3.8}$$

Where $q_e$ is the charge of an electron, $E_o$ is the incident photon energy, $E_{ion}$ is the average energy required to produce an electron-ion pair (See table 3.1), $\mu/\rho_{EA(E_o)}$ is the mass energy absorption coefficient which is the part of the mass attenuation coefficient that leads to absorbed energy in the ion chamber gas (photoelectric and partial Compton scattering) at energy $E_o$, $\mu/\rho_{T(E_o)}$ is the total mass attenuation coefficient for the gas at energy $E_o$, the material density is $\rho$, and L is the plate length of the ion chamber. Equation 3.8 is applicable in the diagnostic X-ray energy regime where there is no charge loss from the system from the escape of high energy electrons. Once the ion chamber $\xi$ value is calculated with units of Coulombs per photon the number of incident photons can be determined by equation 3.9.

$$N_o = \frac{I_{ch}}{\xi} = \frac{G \times V}{\xi} \tag{3.9}$$

Where $I_{ch}$ is the current output of the ion chamber, G is the gain of the electrometer (typically in Volts per Ampere), and V is the voltage output of the electrometer.

## 3.3 Dose Calculations

When planning an experiment it is often important to predict the scan time required to acquire the desired image. Once the scan time is known the dose and dose rate delivered to the sample may be calculated to determine if it is reasonable. For the

| Gas | Energy (eV) |
|---------|------|
| Helium | 41 |
| Nitrogen | 36 |
| Air | 34.4 |
| Neon | 36.3 |
| Argon | 26 |
| Krypton | 24 |
| Xenon | 22 |

Table 3.1: List of the average energy required to produce an electron-ion pair in common ion chamber gases [Tho01].

diagnostic X-ray imaging regime the most important dose value to know is the equivalent dose for the surface of a homogeneous object as all other values beneath the surface will be lower than this entrance dose. Effective dose values for radiosensitive organs may be calculated from the effective dose surface value using an anatomical model. The discussion to follow is restricted to absorbed and equivalent dose as there are too many heterogeneous samples with unique tissue radiosensitive weighting factors to discuss briefly.

To calculate absorbed dose, here after referred to as dose, it is necessary to know the energy deposited and the mass of the material it was absorbed in. In simple terms this gives an equation,

$$\text{Dose} = \frac{\text{Energy Deposited}}{\text{Object Mass}}.$$

For a monochromatic beam the energy deposited is calculated by taking the number of photons stopped in the material times the energy of the photons. Recognizing the

energy dependence of the dose we can rewrite the equation as,

$$D(E_{ph}) = \frac{N_{abs} E_{ph}}{M}$$

Where $D(E_{ph})$ is the dose at the photon energy $E_{ph}$, $N_{abs}$ is the number of photons absorbed, and M is the mass involved in radiation absorption. The mass of the object is readily calculated by taking the area intersected by the beam (A) times the thickness of the material (L) times the density of the material ($\rho$), $A \cdot L \cdot \rho$. The number of photons that deposit energy in the object is given by Beer's law multiplied by a ratio to correct for the fact not all of the photons that are deviated while passing through the object will deposit all or some of their energy in the mass. For a voxel of mass beneath the surface as seen in figure 3.5 the number of photons that will be absorbed in this region that is embedded at a length x under the surface with thickness dx is,

$$dN_{abs} = N_o \times \exp\left(-\frac{\mu(E_{ph})}{\rho_T}\rho x\right) \times \left[1 - \exp\left(-\frac{\mu(E_{ph})}{\rho_{EA}}\rho \, dx\right)\right]$$

$$dN_{abs} \simeq N_o \times \exp\left(-\frac{\mu(E_{ph})}{\rho_T}\rho x\right) \times \frac{\mu(E_{ph})}{\rho_{EA}}\rho \, dx \tag{3.10}$$

If the absorption along the whole path is considered the equation becomes,

$$\int_0^L dN_{abs} = N_o \times \frac{\mu(E_{ph})}{\rho_{EA}}\rho \times \int_0^L \exp\left(-\frac{\mu(E_{ph})}{\rho_T}\rho x\right) dx$$

$$\text{let } u = -\frac{\mu(E_{ph})}{\rho_T}\rho x \Rightarrow du = -\frac{\mu(E_{ph})}{\rho_T}\rho dx \Rightarrow dx = \frac{1}{-\frac{\mu(E_{ph})}{\rho_T}\rho} \cdot du$$

$$N_{abs} = -N_o \left(\frac{\mu(E_{ph})}{\rho_{EA}} \cdot \rho \middle/ \frac{\mu(E_{ph})}{\rho_T} \cdot \rho\right) \times \int_0^L \exp(u) \ du$$

$$N_{abs} = -N_o \left(\frac{\mu(E_{ph})}{\rho_{EA}} \middle/ \frac{\mu(E_{ph})}{\rho_T}\right) \exp\left(-\frac{\mu(E_{ph})}{\rho_T}\rho \ x\right)\Bigg|_0^L$$

$$N_{abs} = N_o \left(\frac{\mu(E_{ph})}{\rho_{EA}} \middle/ \frac{\mu(E_{ph})}{\rho_T}\right)\left(1 - \exp\left(-\frac{\mu(E_{ph})}{\rho_T}\rho \ L\right)\right) \tag{3.11}$$

Where $N_{abs}$ is the number of absorbed photons, $N_o$ is the total number of incident photons, $E_{ph}$ is the incident photon energy, $\mu/\rho_{EA(E_{ph})}$ is the partial mass attenuation coefficient that leads to energy absorption, $\mu/\rho_{T(E_o)}$ is the total mass attenuation coefficient for the object, $\rho$ is the material density, and L is the X-ray path length through the object.
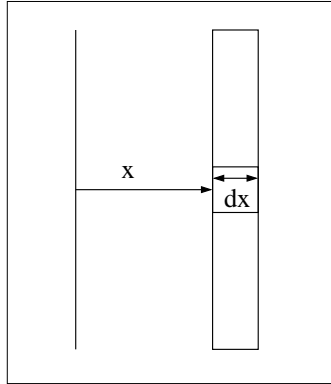


Figure 3.5: Diagram of a voxel beneath the surface. The photon count arriving at the voxel is attenuated by the layers above.

Substituting the expressions for mass and the number of absorbed photons into the

previous equation for dose gives,

$$D(E_{ph}) = E_{ph}N_o \left(1 - \exp\left(-\frac{\mu_{(E_{ph})}}{\rho_T}\rho L\right)\right) \cdot \left(\frac{\mu_{(E_{ph})}}{\rho_{EA}} \bigg/ \frac{\mu_{(E_{ph})}}{\rho_T}\right) \cdot (AL\rho)^{-1} \quad (3.12)$$

If the dose rate is desired equation 3.12 can be used by replacing the total number of incident photon term, $N_o$, for the number of photons per second, $\dot{N}$.

To calculate the surface dose the limit is taken as the thickness goes to zero and the exponential term is replaced by a first order expansion. The approximate surface dose is then given by,

$$D_s(E_{ph}) = \frac{N_o E_{ph}}{A} \frac{\mu(E_{ph})}{\rho_{EA}} \quad (3.13)$$

The units of absorbed dose are the Gray[J/kg] (Si unit) and Radiation Absorbed Dose (RAD)[100ergs/gram]. The units of equivalent dose are the Sievert (Si unit) and the Röntgen Equivalent Man (REM), which are equal to their respective absorbed dose values multiplied by a radiation weighting factor. For the photon the radiation weighting factor is equal to one so absorbed dose values in Grays are equivalent to equivalent dose values in Sieverts [Hen02].

# Chapter 4

# Diffraction Enhanced Imaging Principles

## 4.1 Bragg's Law of Diffraction

Most X-ray sources such as X-ray tubes and synchrotrons provide polychromatic beams for experimentation, however, for scientific measurements a monochromatic source of X-rays is frequently desirable. At a synchrotron facility a common way to monochromate the polychromatic beam is by using a double crystal Bragg monochromator to select the X-ray wavelength.

Bragg's Law states,

$$n\lambda = 2 \text{ d } \sin\theta \tag{4.1}$$

for an X-ray wavelength $\lambda$ (k $= 2\pi/\lambda$), a crystal lattice spacing d, an integer value n, and an angle $\theta$ between the incident beam and the crystal planes.

From figure 4.1 it is easy to derive Bragg's Law. If a condition is set that the sum of the extra path lengths is equal to an integer number of wavelengths the result is, $n\lambda = p_1 + p_2$. Both $p_1$ and $p_2$ are equal to the sine of the angle $\theta$ times the distance between lattice planes d. Substituting we then have $n\lambda = d \cdot \sin(\theta) + d \cdot \sin(\theta)$ and by simplifying this result we get equation 4.1 or Bragg's Law.
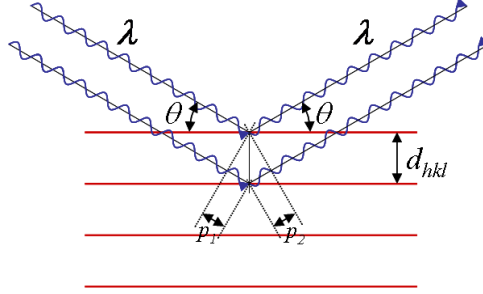


Figure 4.1: Diagram of the condition for X-ray diffraction off a crystal surface described by Bragg's Law.

## 4.2 Crystal Properties

From Bragg's Law it would appear that after crystal diffraction there will be only a single wavelength remaining from the original polychromatic beam. In reality due to crystal properties and divergence of the beam there will remain an energy bandwidth, $\Delta\lambda$, centered around $\lambda$. The bandwidth $\frac{\Delta\lambda}{\lambda} = \frac{1}{N}$, where N is the number of lattice planes that participate in forming the diffracted beam. To establish the properties of an X-ray beam prepared using a double crystal monochromator (DCM) a brief description of crystals follows.

## 4.2.1 Lattice Structure

The unique diffraction properties of a perfect crystal comes from the periodic structure of the atoms which it is composed of. Within the crystal volume if the location of one atom is known then another atom can be found by traveling an integer number of the lattice vectors $\vec{a_1}$, $\vec{a_2}$, and $\vec{a_3}$. The periodic structure of atoms means that the accompanying electrons, which are responsible for photon interactions in the X-ray energy regime, are also arranged in a periodic manner (See figure 4.2).
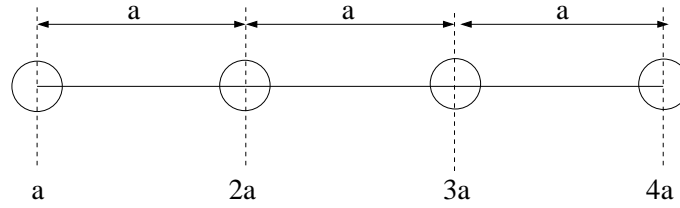


Figure 4.2: Fixed lattice spacings in a crystal places atoms and accompanying electrons at repeating intervals.

The electronic density may then be described as having the property $\rho_e(\vec{r}) = \rho_e(\vec{r} + n_1 \cdot \vec{a_1} + n_2 \cdot \vec{a_2} + n_3 \cdot \vec{a_3})$ and that the integral over one unit cell equals the number of atoms in the unit cell times the number of electrons per atom, $\int_{cell} \rho_e(\vec{r}) d^3r = Z_{cell}$. An incident X-ray at the appropriate Bragg angle will encounter a periodic electron density in the crystal lattice and will be absorbed and re-radiated. The bandwidth of the reflection is inversely proportional to the number of electrons in the crystal lattice planes that contribute to the diffracted beam or those electrons that scatter in phase. For perfect crystals the bandwidth can also be calculated from,

$$\frac{\Delta E}{E_{int}} = \frac{4d_{hkl}^2 r_e}{\pi V_c} \sqrt{|F_{hkl} F_{\overline{hkl}}|}.$$

Where $\frac{\Delta E}{E_{int}}$ is the intrinsic crystal bandwidth, $d_{hkl}$ is the crystal lattice spacing, $r_e$

is the classical electron radius, $V_c$ is the volume of the unit cell, and $F_{hkl}$ is the structure factor for the Miller indices hkl [Zac45]. It should be noted that only a few microns thickness is involved in diffraction of the incident beam using a perfect crystal. The depth into the crystal where the incident beam has been reduced by $1/e$ from diffraction is given by,

$$L_{ex} = \frac{2}{\pi} \frac{d_{hkl}}{\Delta E/E_{int}}.$$

To estimate the number of lattice planes involved in a reflection the extinction length $L_{ex}$ should be divided by the d-spacing.

## 4.2.2   Reciprocal Space

To determine the lattice spacing used in Bragg's equation an understanding of reciprocal space is needed. Using the periodicity of the electronic structure shown in figure 4.2 a Fourier series describing this space will need to be periodic over the length **a**. The sine and cosine functions of the Fourier series are naturally periodic over $2\pi$ so a term is needed to change that periodicity over length **a**. This is easily achieved by taking the reciprocal of **a** times $2\pi$. The function to describe the electron number in one dimension for the crystal structure can then be written as,

$$\rho_e(x) = \rho_o + \sum_{n>0} \left[ C_n \cos\left(\frac{2\pi nx}{a}\right) + S_n \sin\left(\frac{2\pi nx}{a}\right) \right]$$

where n is any positive integer, and $C_n$ and $S_n$ are real constants for the Fourier cosine and sine coefficients respectively [Kit86]. The $2\pi n/a$ terms are the points in the reciprocal lattice of the crystal which are the allowed terms in the Fourier series $\rho_e(x)$. A term is allowed only if it follows the periodicity of the crystal, while all

other points are not allowed. Before moving from a one dimensional representation to three dimensions it is convenient to start writing the Fourier series in terms of exponentials, $e^{ix} = \cos x + i \sin x$. For one dimension the function $\rho_e(x)$ becomes,

$$\rho_e(x) = \sum_n \rho_n \exp(i2\pi nx/a)$$

where the sum is over all integers, and the coefficients $\rho_n$ are complex numbers with the condition that the complex conjugate of $\rho_{-n}$ is equal to $\rho_n$ so that the function $\rho_e(x)$ remains real. To extend the Fourier analysis to three dimensions a set of vectors $\vec{G}$ must be found such that,

$$\rho(\vec{r}) = \sum_{\mathbf{G}} \rho_{\mathbf{G}} \exp(i\vec{G} \cdot \vec{r})$$

where $\rho_{\mathbf{G}}$ determines the X-ray scattering amplitude [Kit86]. To find the G vectors, reciprocal lattice basis vectors, $\vec{b_1}$, $\vec{b_2}$, and $\vec{b_3}$ are needed just as primitive lattice vectors, $\vec{a_1}$, $\vec{a_2}$, and $\vec{a_3}$, were needed in the crystal. For $\vec{G} = h\vec{b_1} + k\vec{b_2} + l\vec{b_3}$ we have the condition that $\vec{b_i} \cdot \vec{a_j} = 2\pi\delta_{ij}$. Thus all of the reciprocal lattice basis vectors are orthogonal to pairs of primitive lattice vectors. To find a system that satisfies these conditions a term $\alpha$ is introduced with the equations, $\vec{b_1} = \alpha(\vec{a_2} \times \vec{a_3}), \vec{b_2} = \alpha(\vec{a_3} \times \vec{a_1})$, and $\vec{b_3} = \alpha(\vec{a_1} \times \vec{a_2})$. We then take $\vec{b_1} \cdot \vec{a_1} = \alpha[\vec{a_1} \cdot (\vec{a_2} \times \vec{a_3})]$ and set it equal to $2\pi$ as per the previous stated conditions and solve. The result is,

$$\alpha = \frac{2\pi}{\vec{a_1} \cdot (\vec{a_2} \times \vec{a_3})}$$

With the expression for $\alpha$ the reciprocal lattice vectors are finalized as,

$$\vec{b_1} = \frac{2\pi(\vec{a_2} \times \vec{a_3})}{\vec{a_1} \cdot (\vec{a_2} \times \vec{a_3})} \tag{4.2}$$

$$\vec{b_2} = \frac{2\pi(\vec{a_3} \times \vec{a_1})}{\vec{a_1} \cdot (\vec{a_2} \times \vec{a_3})} \tag{4.3}$$

$$\vec{b_3} = \frac{2\pi(\vec{a_1} \times \vec{a_2})}{\vec{a_1} \cdot (\vec{a_2} \times \vec{a_3})} \tag{4.4}$$

For the cubic representation of the silicon crystal lattice the primitive vectors are, $\vec{a_1} = a_o\hat{x}$, $\vec{a_2} = a_o\hat{y}$, and $\vec{a_3} = a_o\hat{z}$. Substituting these values into the equations for the reciprocal lattice vectors gives, $\vec{b_1} = \frac{2\pi}{a_o}\hat{x}$, $\vec{b_2} = \frac{2\pi}{a_o}\hat{y}$, and $\vec{b_3} = \frac{2\pi}{a_o}\hat{z}$. Thus the magnitude of vector $\vec{G}$ is equal to, $|\vec{G}| = \frac{2\pi}{a_o}\sqrt{h^2 + k^2 + l^2}$. Using the wave vector description for crystal diffraction shown in figure 4.3 and Bragg's law we know that $|\vec{G}| = 2\pi/d_{hkl}$. It is then possible to arrive at the expression for the distance parameter for a cubic lattice,

$$d_{hkl} = \frac{a_o}{\sqrt{h^2 + k^2 + l^2}} \tag{4.5}$$
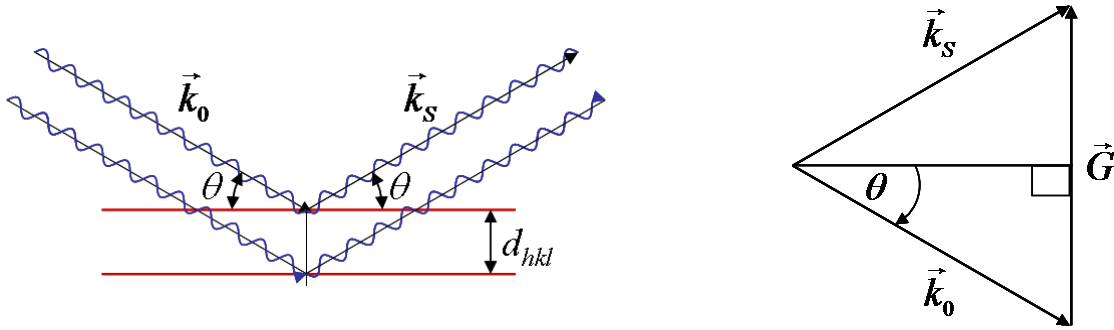


Figure 4.3: A wave vector description of crystal diffraction introduces a scattering vector $\vec{G}$ which is perpendicular to the hkl lattice plane.

To define a diffraction plane of interest the Miller indices are used. The indices describe the orientation of a family of parallel equidistant planes in the lattice of

32

a crystal [Cul56]. They are defined as the reciprocals of the fractional intercepts which the plane closest to the origin (but not including the origin) makes with the crystallographic axes. A plane with Miller indices of (h, k, l) makes fractional intercepts of $a_1/h$, $a_2/k$, $a_3/l$ with the axes $\vec{a_1}$, $\vec{a_2}$, and $\vec{a_3}$ where $a_1$, $a_2$, and $a_3$ are the unit axial lengths. In X-ray diffraction the diffraction order is given by the d-spacing and represented by the Miller indicies (hkl) thus removing the integer term n from Bragg's equation, $\lambda = 2d_{hkl} \sin\theta$.

### 4.2.3  Crystal Reflectivity and DuMond Diagrams

To understand how DEI works an overview of crystal reflectivity is necessary. From equation 4.1 it is expected that for a specific wavelength, $\lambda_x$, that the crystal will diffract incident photons only if the lattice planes are aligned to the Bragg angle, $\theta_x$. If the lattice planes are misaligned by $\Delta\theta_x$ and this misalignment is sufficiently small ($\sim 10^{-6}\mu radians$) there will also be significant crystal diffraction. This is due to the width of the crystal reflectivity (See figure 4.4), which is characterized by the Darwin width [Als01],

$$\omega_D = \frac{2hcr_e d_{hkl}|F_{hkl}|}{\pi E V_c \cos\theta_B}.$$

Where h is Planck's constant, c is the speed of light in a vacuum, $r_e$ is the classical electron radius, $d_{hkl}$ is the spacing of the lattice planes, $F_{hkl}$ is the structure factor, E is the photon energy, $V_c$ is the volume of the unit cell, and $\theta_B$ is the Bragg angle.

To keep the beam parallel with the incident X-ray direction a pair of crystals is commonly used and the intensity of diffracted X-rays follows the product of two single crystal reflectivity profiles with the possibility of an angular mismatch. When
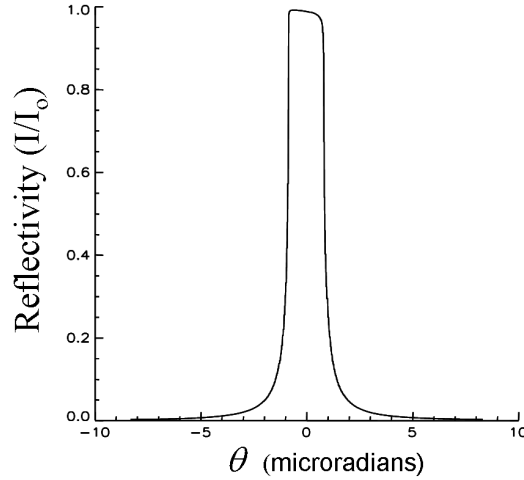
Figure 4.4: Reflectivity profile for a single Si[4,4,0] crystal at 40keV with near unity maximum value. The Bragg angle is the center of the peak and deviations in angle lower or higher are measured from this location.

one of the crystals is rocked in angle relative to the other the result is the convolution of the two profiles and is called the rocking curve. For a simplified rocking curve where the single crystal reflectivity is rectangular the rocking curve width is equal to the Darwin width as shown in figure 4.5a. In the case of two perfect crystals the reflectivities convolve to a rocking curve width that is close to the Darwin width and is illustrated in figure 4.5b. It is this perfect crystal rocking curve that is used to encode information in the DEI technique. Any refraction deviation or scattering that occurs in the sample will cause small changes in the X-ray path altering the probability that the X-ray will be diffracted off of the analyzer crystal and be detected. Assuming a DEI system where the analyzer crystal has been aligned to the Bragg angle and a refraction deviation from an interface between two heterogeneous regions within the sample was to cause a deviation in the X-ray path of $\Delta\theta_{\mathrm{dv}} = \frac{1}{2}\omega_{\mathrm{D}}$, the probability of those X-rays being diffracted to the detector would be half as much as X-rays that did not experience the deviation $\Delta\theta_{\mathrm{dv}}$. The loss of half the X-rays caused by refraction at the interface between the heterogeneous regions would then have

significant contrast in the image compared to surroundings that caused no refraction deviation at all and have double the photon count. The contrast value in this case would be,

$$C = \frac{N_{background} - N_{interface}}{N_{background}} = \frac{1 - 1/2}{1} = \frac{1}{2}$$
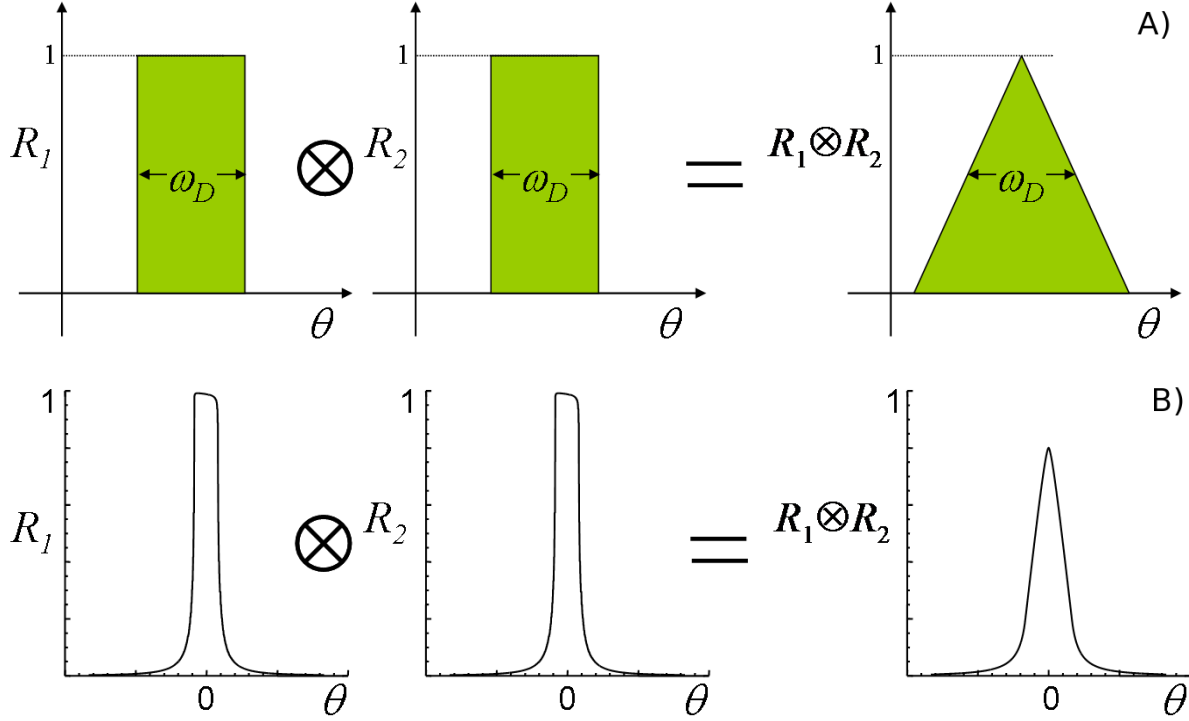


Figure 4.5: A) A simplified rocking curve were two rectangular reflectivities convolve to a triangle. B) Two single crystal reflectivity profiles convolved together result in a DCM rocking curve. It is convenient to think of this crystal system in terms of a Venn diagram. Each crystal has a range of angles where X-rays have a probability of being diffracted by the crystal. The rocking curve on the right hand side indicates the amount of overlap between the two angular ranges and the maximum is the case where the crystals are aligned to the exact same angle and the crystal reflectivities overlap completely.

To understand how the DCM rocking curve behaves it is useful to draw DuMond diagrams showing the behavior of each crystal involved. In figure 4.6 a) the Bragg curves using equation 4.1 are plotted for the Si[1,1,1] and Si[2,2,0] with the next harmonic, which shows how each reflection has a unique slope. These Bragg curves are not infinitely narrow, but have a finite width associated with them as seen in

figure 4.6 b) and is equal to the Darwin width. This means that for a plane wave of only one wavelength there is a small range of angles that will allow diffraction, which implies that Bragg's Law has some fuzziness to it. This is shown by the reflectivity plotted in figure 4.4 where the probability of diffraction is large at the Bragg angle and is also large one half the Darwin width away from the Bragg angle to either side. Similarly, for only one angle there is a small range of wavelengths that may diffract and is represented by the bandwidth $(\Delta\lambda/\lambda)$. It is the combination of these two affects that will determine the bandwidth for a crystal given that incident photons from either an X-ray tube or a synchrotron have variations in wavelength and angle [Als01].
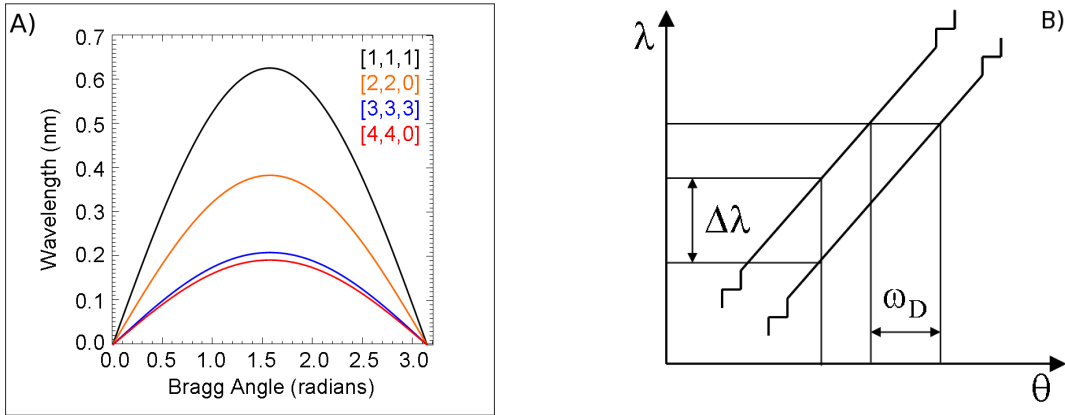


Figure 4.6: A) Crystal reflections have unique slopes and different wavelength ranges. B) A zoomed in view of every slope will reveal an intrinsic width and wavelength spread unique to each crystal reflection.

For a two crystal system the alignment of both crystals to the same Bragg angle must be accomplished if diffracted beam is to pass through. Before the crystals are aligned the Bragg curves of the crystals (assuming the same crystal composition and reflection) may be drawn as a sine wave with a phase shift, $\Delta\theta$, between them, which corresponds to the angle difference between the two crystals (See figure 4.7). As the lattice planes of the two crystals are aligned to the same angle the diffracting regions

36

of the two curves will start to overlap increasing the probability that a photon will pass through the system. The maximum occurs when there is no angle difference between the crystal diffraction planes.
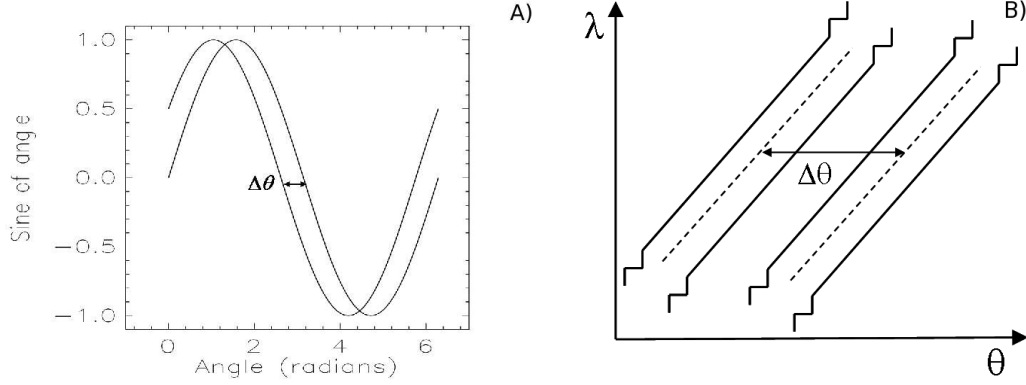


Figure 4.7: A) & B) For two like crystals with an angle difference between the diffraction planes the Bragg curves can be thought of as having a phase difference equal to the difference in angle $\Delta\theta$.

For figure 4.6a it should be noted that for a chosen wavelength on the Y axis there will be more than one intercept on the plot along the X axis for each reflection. This fact creates two separate cases for crystal orientation, the parallel crystal geometry (non-dispersive), and the anti-parallel crystal geometry (dispersive).

In the parallel crystal geometry the Bragg curves of two like crystals have the same slope. If a divergent polychromatic incident X-ray beam populates angles $\Delta\theta_{div}$ and the diffraction planes of the two crystals have no misalignment there is a maximum photon transmission at this one location (See figure 4.8). As the diffraction planes of the two crystals are misaligned in either direction the photon transmission would drop as the overlapping regions of the two curves is reduced. Assuming one crystal is fixed and the other is being rocked from smaller to larger angles position $\theta_{A1}$ is just before reflectivity overlap and $\theta_{A2}$ is when there is no longer any overlap. If the

two crystals were in a misaligned state and the angle was changed continuously to alignment and through to an equally misaligned state on the other angle side then the resulting measured photon intensity would be the double crystal rocking curve. It is the slope of the rocking curve that determines the amount of intensity variation associated with an angle change and hence provides contrast to the measured DEI image. For the parallel crystal geometry the slope of the analyzer crystal reflectivity is approximately the inverse of the Darwin width, $\frac{dR}{d\theta_A} \approx \frac{1}{\omega_D}$.
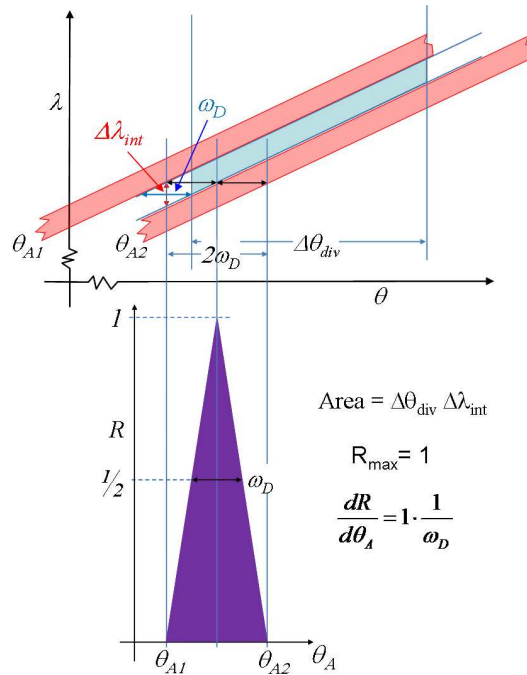


Figure 4.8: When two like crystals are in the parallel geometry the slopes of the Bragg curves are the same and for a diverging incident beam containing angles $\Delta\theta_{div}$ the entire populated region of both crystals may overlap at once to give the maximum amount of photons diffracted.

In the anti-parallel crystal geometry the Bragg curves of two like crystals have the same slopes with opposite signs. If a divergent polychromatic incident X-ray beam populates angles $\Delta\theta_{div}$ there is a range of angles, not just one point, where the Bragg curves have a maximum overlapping area leading to a measured intensity pro-

file which is flat over a range (See figure 4.9). Again one crystal is held fixed and another is rocked in angle. Assuming the crystal is being rocked from smaller to larger angles position $\theta_{A1}$ is when the reflectivities begin to overlap, position $\theta_{A2}$ is the first angle where maximum overlap has occurred, position $\theta_{A3}$ is the last position where there is maximal overlap, and position $\theta_{A4}$ is where there is no longer any overlap. It should be noted that the energy content passing through an anti-parallel crystal system varies with the angular location. For smaller angles the photon energies would be slightly higher than for the larger angles. For the anti-parallel crystal geometry the slope of the analyzer reflectivity is approximately the inverse of four times the angular divergence of the incident beam, $\frac{\mathrm{dR}}{\mathrm{d}\theta_A} \approx \frac{1}{4\Delta\theta_{\mathrm{div}}}$.
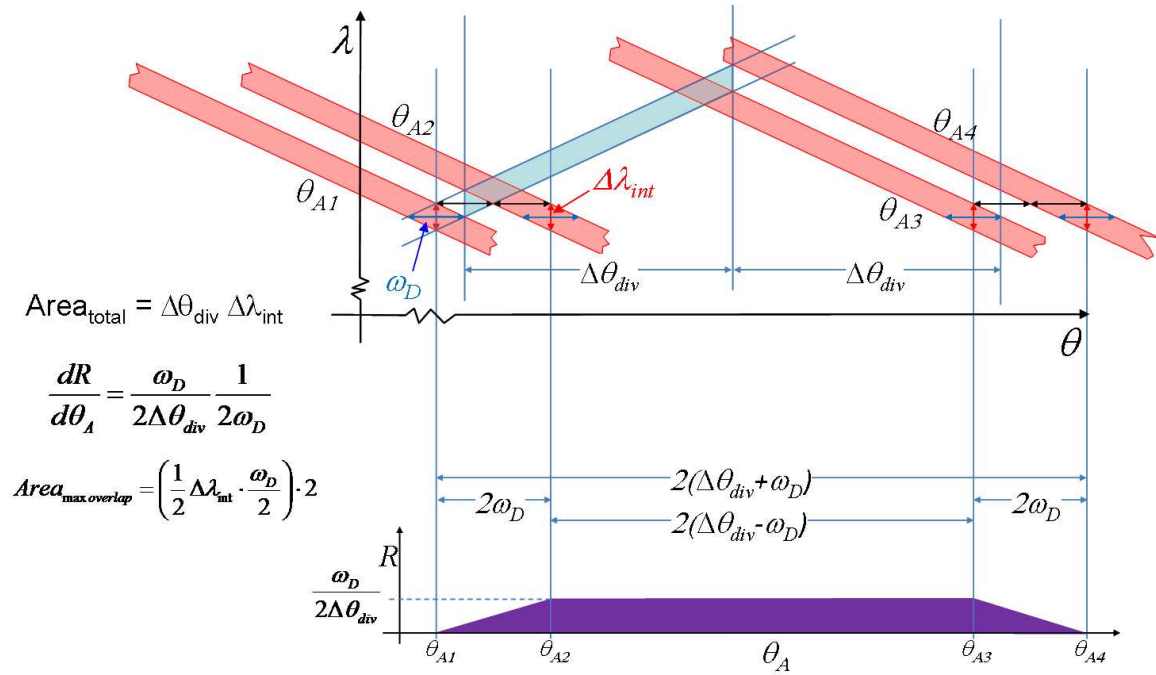


Figure 4.9: When two like crystals are in the anti-parallel geometry the slopes of the Bragg curves for the two crystals are different. This means that the populated region of angles $\Delta\theta_{div}$ does not completely overlap at once and a maximal photon transmission occurs over a region.

After reviewing the parallel and anti-parallel crystal systems it is apparent that for

analyzer based imaging the crystal arrangement necessary is a parallel system. The slope of the parallel crystal orientation gives $10^3 - 10^4$ times the sensitivity of the non-parallel crystal geometry depending on the X-ray energy used. Also, in the non-parallel geometry only a small region of the total angular divergence is overlapped by the crystals meaning the majority of the incident photons are not used to form the image, but still deliver dose.

## 4.3   Absorption and Refraction Angle Images

Using the DEI technique two images can be formed from the data, one for absorption, and another for refraction. Before deriving these formulas some variable definitions are needed and are given in Table 4.1.

| | |
|---|---|
| $\zeta = \sum_i \mu_i t_i$ | Coefficient sum for all absorption and scattering loss through the sample |
| $N(\theta_A)$ | Number of measured counts after the analyzer as a function of $\theta$ |
| $N_T$ | Total number of incident photons |
| $N_L$ | Number of counts on the low angle side of the rocking curve |
| $N_H$ | Number of counts on the high angle side of the rocking curve |
| $R(\theta)$ | Is the reflectivity of the monochromator and analyzer system as a function of angle |
| $R_L$ | Is the reflectivity on the low angle side of the rocking curve: $R(\theta_L)$ |
| $R_H$ | Is the reflectivity on the high angle side of the rocking curve: $R(\theta_H)$ |
| $R'_L$ | Is the slope of the reflectivity curve at the low angle position: $\frac{dR(\theta)}{d\theta}\Big|_{\theta=\theta_L}$ |
| $R'_H$ | Is the slope of the reflectivity curve at the high angle position: $\frac{dR(\theta_H)}{d\theta}\Big|_{\theta=\theta_H}$ |
| $\Delta\theta_Z$ | Is the deviation in angle due to refraction in the Z direction |

Table 4.1: Variables for the derivation of the DEI equations.

The two equations that are desired are those for an absorption image and a refraction angle image. To start towards these equations we consider one of the known relations. The photon counts measured in the detector will equal the total number of incident photons times the reflectivity of the crystal (the fraction reflected to the detector) times the amount transmitted through the sample (the fraction not absorbed or

scattered),

$$N(\theta_A) = N_T \cdot R(\theta_A + \Delta\theta_z) \cdot \mathrm{e}^{-\zeta}$$

The second relation known is that the reflectivity in the measurement is approximately equal to the reflectivity at the analyzer angle plus the product of the slope of the reflectivity curve at the analyzer angle and the size of the refraction deviation,

$$R(\theta_A + \Delta\theta_z) \approx R(\theta_A) + \left.\frac{dR(\theta)}{d\theta}\right|_{\theta=\theta_A} \Delta\theta_z$$

Using the relations above for the measured photon count and the crystal reflectivity it follows for the low and high angle side the photon count is given by,

$$N_L \approx N_T \left( R(\theta_L) + \left.\frac{dR(\theta)}{d\theta}\right|_{\theta=\theta_L} \Delta\theta_Z \right) \mathrm{e}^{-\zeta} = N_T(R_L + R'_L\Delta\theta_Z)\mathrm{e}^{-\zeta} \tag{4.6}$$

$$N_H \approx N_T \left( R(\theta_H) + \left.\frac{dR(\theta)}{d\theta}\right|_{\theta=\theta_H} \Delta\theta_Z \right) \mathrm{e}^{-\zeta} = N_T(R_H + R'_H\Delta\theta_Z)\mathrm{e}^{-\zeta} \tag{4.7}$$

Solving equation 4.6 for total number of incident photons ($N_T$) gives,

$$N_T = \frac{N_L}{(R_L + R'_L\Delta\theta_Z)\mathrm{e}^{-\zeta}}$$

Substituting the expression above for $N_T$ into equation 4.7 gives,

$$\Rightarrow N_H = \frac{N_L}{(R_L + R'_L\Delta\theta_Z)\mathrm{e}^{-\zeta}} \cdot (R_H + R'_H\Delta\theta_Z)\mathrm{e}^{-\zeta} = \frac{N_L(R_H + R'_H\Delta\theta_Z)}{(R_L + R'_L\Delta\theta_Z)}$$

Solving the previous expression for $\Delta\theta_Z$ has the result,

$$N_H(R_L + R'_L\Delta\theta_Z) = N_L(R_H + R'_H\Delta\theta_Z)$$

$$\Rightarrow N_H R_L - N_L R_H = (N_L R'_H - N_H R'_L)\Delta\theta_Z$$

$$\Rightarrow \Delta\theta_Z = \frac{N_H R_L - N_L R_H}{N_L R'_H - N_H R'_L} \tag{4.8}$$

which is the formula for the refraction angle image.

Using equation 4.8 and substituting this into the expression for $N_T$ allows the absorption image equation to be determined,

$$N_T = \frac{N_L}{\left(R_L + R'_L \cdot \frac{N_H R_L - N_L R_H}{N_L R'_H - N_H R'_L}\right) e^{-\zeta}}$$

$$\Rightarrow N_T \cdot e^{-\zeta} = \frac{N_L \cdot (N_L R'_H - N_H R'_L)}{R_L \cdot (N_L R'_H - N_H R'_L) + R'_L \cdot (N_H R_L - N_L R_H)}$$

$$\Rightarrow N_T \cdot e^{-\zeta} = \frac{N_L \cdot (N_L R'_H - N_H R'_L)}{R_L N_L R'_H - R_L N_H R'_L + R'_L N_H R_L - R'_L N_L R_H}$$

$$\Rightarrow N_T \cdot e^{-\zeta} = \frac{N_L \cdot (N_L R'_H - N_H R'_L)}{N_L \cdot (R_L R'_H - R_H R'_L)}$$

$$\Rightarrow N_T \cdot e^{-\zeta} = \frac{N_L R'_H - N_H R'_L}{R_L R'_H - R_H R'_L} \tag{4.9}$$

For a DEI measurement where data is collected at the half maximum points on either side of a Bragg double crystal rocking curve the following substitutions into equations 4.8 and 4.9 are valid if a simplified rocking curve as in figure 4.5a is assumed: 1) $R_H = R_L = 1/2$ ; 2) $R'_L = 1/\omega_D$ ; and 3) $R'_H = -1/\omega_D$. The absorption and refraction equations then simplify to,

$$N_T \cdot e^{-\zeta} = \frac{N_L \cdot -1/\omega_D - N_H \cdot 1/\omega_D}{1/2 \cdot -1/\omega_D - N_H \cdot 1/\omega_D} = N_L + N_H \tag{4.10}$$

$$\Delta\theta_z = \frac{1/2 \cdot N_H - 1/2 \cdot N_L}{N_L \cdot -1/\omega_D - N_H \cdot 1/\omega_D} = \frac{\omega_D}{2} \cdot \frac{N_L - N_H}{N_L + N_H} \tag{4.11}$$

## 4.4  Ultra Small Angle Scattering

To derive the equation for ultra-small angle X-ray scattering (USAXS) imaging the measured intensity at the detector for an analyzer Bragg angle $\theta$ will be redefined

as,

$$I(\theta; x, y) = I_R(x, y) \int R(\theta + \Delta\theta_R(x, y) + \Delta\theta_S) f(\Delta\theta_S; x, y) d(\Delta\theta_S)$$

Where $I_R(x, y)$ is the apparent absorption intensity, $R(\theta + \Delta\theta_R(x, y) + \Delta\theta_S)$ is the crystal reflectivity depending on the Bragg angle $\theta$, the refraction deviation angle $\Delta\theta_R(x, y)$, and the scattering angle $\Delta\theta_S$, and $f(\Delta\theta_S; x, y)$ is the vertical plane photon scattering probability density [Rig07]. Assuming the refraction deviation and scattering angles are smaller than the analyzer crystal Darwin width the reflectivity expression may be Taylor expanded, which will be taken to second order.

The resulting expression approximating the intensity is given by,

$$I(\overline{\theta}; x, y) = I_R(x, y) \left[ R(\overline{\theta}) + \left.\frac{\partial R}{\partial \theta}\right|_{\overline{\theta}} \Delta\theta_R(x, y) + \frac{1}{2}\left.\frac{\partial^2 R}{\partial \theta^2}\right|_{\overline{\theta}} \Delta\theta_R^2(x, y) + \frac{1}{2}\left.\frac{\partial^2 R}{\partial \theta^2}\right|_{\overline{\theta}} \sigma^2_{\Delta\theta_S}(x, y) \right]$$

Where $\sigma^2 \Delta\theta_S$ is the expectation value for the scattering angle, $\sigma^2 \Delta\theta_S = \int (\Delta\theta_S)^2 f(\Delta\theta_S; x, y) d(\Delta\theta_S)$. If three measurements at different locations on the rocking curve are acquired there will be three independent equations and three variables (absorptions, refraction, and scatter) allowing the system to be solved.
The equations for absorption, refraction, and scatter are given by,

$$I_R = \sum_{i,j,k=1}^{3} \varepsilon_{ijk} I_i \dot{R}_j \ddot{R}_k \left/ \sum_{i,j,k=1}^{3} \varepsilon_{ijk} R_i \dot{R}_j \ddot{R}_k \right. \tag{4.12}$$

$$\Delta\theta_R = -\sum_{i,j,k=1}^{3} \varepsilon_{ijk} I_i R_j \ddot{R}_k \left/ \sum_{i,j,k=1}^{3} \varepsilon_{ijk} I_i \dot{R}_j \ddot{R}_k \right. \tag{4.13}$$

$$\sigma^2_{\Delta\theta_S} = 2 \sum_{i,j,k=1}^{3} \varepsilon_{ijk} I_i R_j \ddot{R}_k \left/ \sum_{i,j,k=1}^{3} \varepsilon_{ijk} I_i \dot{R}_j \ddot{R}_k - (\Delta\theta_R)^2 \right. \tag{4.14}$$

where $\varepsilon_{ijk}$ is the totally antisymmetric tensor [Rig07].

In figure 4.10 if measurements 1 and 3 are at the half maximum points as in the previous section and measurement 2 is at the top of the rocking curve we have, $\ddot{R}_1 = 0$, $\dot{R}_2 = 0$, and $\ddot{R}_3 = 0$. Equations 4.12 and 4.13 will then reduce to equations 4.10 and 4.11 with 4.14 simplifying to $\sigma^2_{\Delta\theta_S} = 2(I_2/I_R - R_2)/\ddot{R}_2 - (\Delta\theta_R)^2$
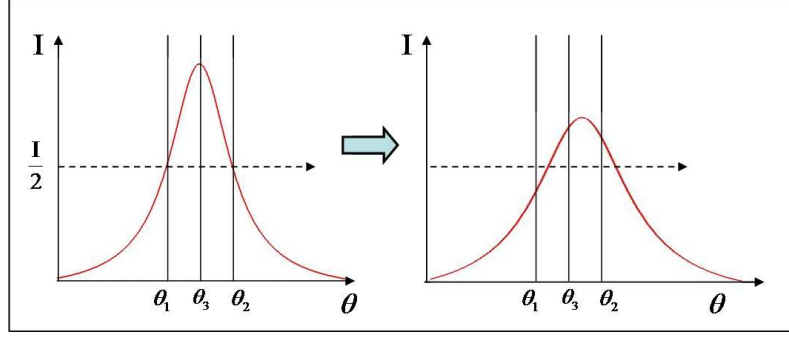


Figure 4.10: The DEI and MIR techniques give approximations to what has happened to the rocking curve by an object's presence in the X-ray beam.

It should be noted that the DEI method is a two point approximation of the rocking curve (positions $\theta_{1,2}$ in figure 4.10) returning absorption and refraction information, and the MIR method is a three point (or more) approximation of the rocking curve returning absorption, refraction, and USAXS information (See figure 4.10). If many points were taken through the rocking curve it would be possible to solve for the absorption, refraction, and USAXS effects of the object on the rocking curve by fitting a Gaussian to the measured points on the curve. If enough points are measured an accurate Gaussian fit of the rocking curve could be performed and the integrated area under the curve would represent the absorption $I_R$, the peak position would represent the refraction $\Delta\theta_R$, and the variance of the Gaussian fit will give an estimate of the USAXS $\sigma^2_{\Delta\theta_S}$.

# Chapter 5

# Gene Expression Mapping Using Synchroton Light Project

In large opaque animals, discovering where genes are expressed can be a long and expensive process. The Gene Expression Mapping using Synchroton light (GEMS) project develops a quick and non-destructive method to visualize gene expression in large whole animals. The GEMS method may in many cases replace both GFP and in-situ hybridization as the method of choice for localizing gene expression. Most diseases occur when the normal expression of genes is altered; the GEMS technique will enable researchers to follow disease progression and the efficacy of therapeutic drugs with ease through nondestructive imaging. The GEMS method can be applied to cancer, immunology, neuroscience, developmental biology and has the potential to be applied in any area where gene expression is important.

As an opportunity to develop and mature the motion control and DAQ software needed for the XRP project I became involved in the GEMS project as the lead developer of the imaging system. The software and hardware knowledge learned

during GEMS was then directly transferable to my own project with program debugging already completed.

## 5.1 System development

The two types of imaging methods used in GEMS were K-edge Subtraction (KES) imaging and Fluorescence Subtraction Imaging (FSI). Figure 5.1 shows the components of the GEMS apparatus, and figure 5.2 shows photographs of the constructed system. The tasks in need of development to perform the GEMS imaging were divided into two areas: 1) motor control; and 2) data acquisition. The software programming and hardware setup for these two categories are detailed in the next subsections.
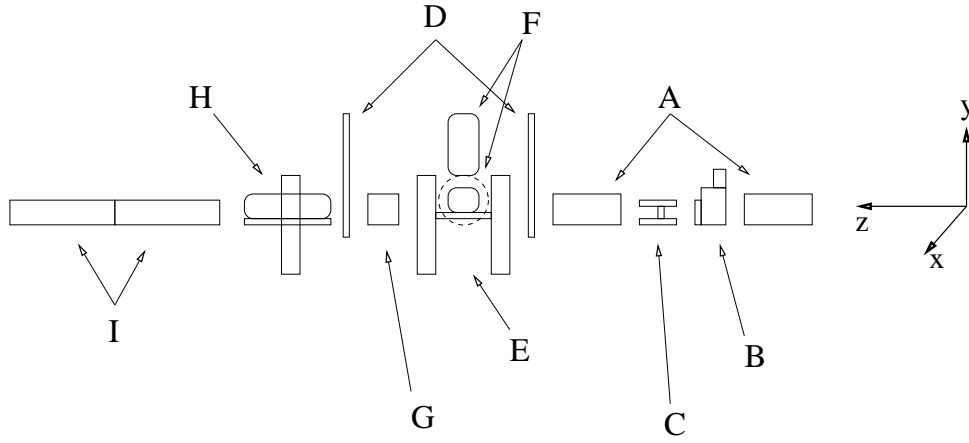
Figure 5.1: Outline of the components in the K-edge and fluorescence detection apparatus. (A) 150mm plate length non-pressurized argon gas filled ion chambers, (B) pneumatic filter assembly, (C) tungsten carbide horizontally aperturing slits, (D) scatter shielding, (E) motorized object scanning stage, (F) multi-element Ge detector, (G) 50mm plate length non-pressurized argon gas filed ion chamber, (H) X-ray camera and motorized stage, and (I) two 300mm plate length non-pressurized krypton gas filled ion chambers in series.
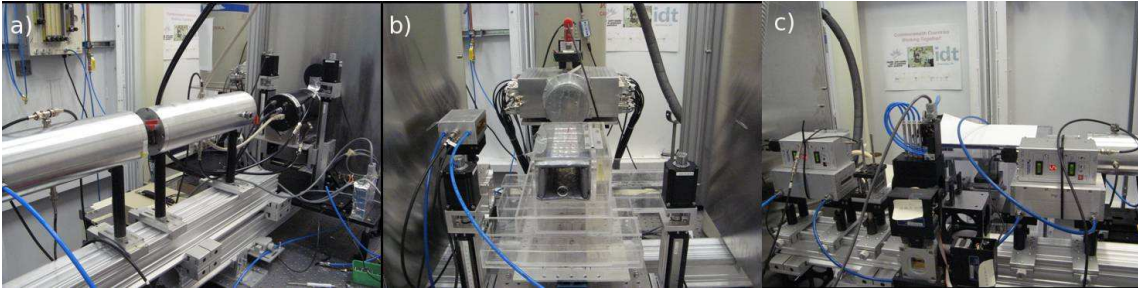
Figure 5.2: Apparatus pictures from the GEMS experiment. a) The down stream detector area, b) The sample area, and c) The upstream beam preparation area.

## 5.1.1 Motion Control

In the GEMS experiment a minimum of three axes of motion were needed to move the object and detector. Two of the axis were required to position the object in the center of the detector for KES imaging, and the same motions were needed to perform raster scans for FSI. The detector required a single vertical motion for KES imaging.

For the line beam KES scan an area detector was used and the object and detector were scanned vertically simultaneously. Two pairs of motorized stages were needed to vertically move the object and detector. If a single NEMA 23 (Parker, Parker Motion Catalogue, Chicago, IL) stepper motor driven stage were used there would be torque concerns for the anticipated loads of the object and detector and a single motorized stage would leave the object/detector cantilevered and susceptible to vibrations. The object and detector were connected with one vertical stage inboard of the beam and one outboard of the beam (See Figure 5.2a). These stages needed to move exactly the same distance and with the same velocity to ensure the platform holder was not damaged. LabVIEW was not able to move four stepper motors simultaneously, but had a maximum of 3 axis simultaneous motion in one vector space. The multi-axis

motion problem was solved in hardware by connecting each pair of vertical stages to a single stepper motor driver in parallel. This also removed concerns of a single motor of the pair losing power, missing steps, or being configured differently than its counterpart any of which would lead to equipment damage. For the pencil beam KES and FSI measurements the object was moved in a raster scan while the fixed ion chambers measured the KES data and the fixed germanium detector measured the FSI data.

## 5.1.2   Data Acquisition

The GEMS experiments required extensive data acquisition programming in the areas of multichannel scaling, shutter triggering, and TTL timing signals. Two versions of the program were required, one for wide beam KES, and another for pencil beam combined FSI/KES measurements.

For the wide beam KES imaging program scalar channels were required to record three ion chambers, which measured: 1) the photon flux entering the hutch; 2) the photon flux after collimation; and 3) the photon flux after the object (See Figure 5.1). The electrometer output from the ion chamber currents were connected to Voltage To Frequency (VTF) converters and the resulting 0 - 5MHz signal connected to the DAQ scalar channels. The object and the detector were moved simultaneously in the same direction either up or down vertically through a 50mm x 0.25mm wide beam. For a given velocity the exposure time for the beam height was calculated and the time bins of the scalars set to match. To reduce the dose delivered to the object a lead plate was placed in a pneumatic shutter assembly (See Figure 5.1). The shutter was triggered to open from LabVIEW when the scanning motion commenced by changing the RS232 connection from 0 to 5V. Between scans (flat field, above the

iodine k-edge, and below the iodine k-edge) the lead shutter was closed to reduce the dose delivered to the object. Other channels of the pneumatic shutter assembly held aluminum and copper plates for attenuating the beam and were operated through a LabVIEW interface which changed the voltage bias for each control channel. At the beginning of each scan a TTL trigger pulse was sent to the VHR-90 X-ray camera (Photonic Science, East Sussex, UK) to begin image capture.

During combined FSI/KES pencil beam imaging the program required three scalar channels for ion chambers that measured: 1) the photon flux entering the hutch; 2) the photon flux after collimation; and 3) two ion chambers in series which measured the absorption in the object (See Figure 5.1). Ion chamber signals were converted to frequencies and connected to the DAQ scalar channels. The object was moved in a horizontal raster scan and the fluorescence detector remained stationary. The line beam used in the KES imaging was changed to a 0.25mm x 0.25mm beam spot from inserting vertically collimating slits contained in the pneumatic shutter assembly. Time binning for the scalars was calculated by dividing the beam height by the raster scan velocity. As before the lead shutter was triggered open only for a measurement and kept closed otherwise to reduce the dose delivered to the object between the above and below Iodine k-edge scans. Attenuating the beam to the desired dose level was accomplished by raising and lowering aluminium and copper plates in the pneumatic shutter assembly [Bew08].

## 5.2   Results

The LabVIEW DAQ and motion control system for GEMS successfully perform both KES and FSI measurements. An image taken using the GEM apparatus is shown

in Figure 5.3. The object in the image is a step wedge phantom containing iodine solution with 2.5 - 22.5mM·cm (1mM·cm=0.127mg/cm2) projected concentrations of iodine in nine 2.5 mM·cm increments. Figure 5.3a shows the wide beam KES image and has two fiducial markers made of lead tape. One marker is a triangle that is above the iodine solution and the other is a square that is below the iodine solution. A white rectangle in the wide beam image marks a region of interest around the faint edge of iodine in the wide beam scan. Figures 5.3b and c are the KES and FSI images from the pencil beam scan of the region of interest and show an increasing projected concentration of iodine from bottom to top corresponding to the increasing projected concentration of iodine in the cuvette.
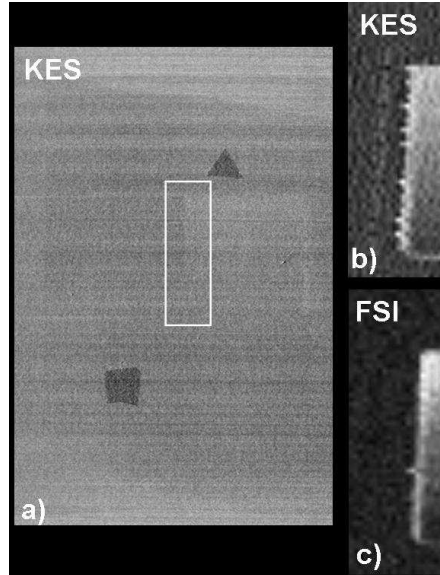


Figure 5.3: KES and FSI images of iodine test object. (a) Wide beam KES image of the test obect. (b) Pencil beam KES of region of interest. (c) Pencil beam FSI of region of interest. [Bew08]

The routines developed for GEMS and debugged during three rounds of experiments provided a collection of hardware functions for future projects during BMIT commissioning and the development of the XRP.

# Chapter 6

# Wide Angle X-ray Scattering Tests

The XRP system was designed with the intent of allowing other X-ray techniques to be performed concurrently with the XRP measurements. One of the X-ray techniques considered for combination with the XRP was WAXS as several groups have demonstrated the value of elastic scatter imaging particularly with biological samples [Har87, Bat06]. This technique was also chosen because it could be added to the system with no flux cost to either measurement unlike KES where both techniques would compete for the primary beam transmitted through the object. The DEI measurement uses only the transmitted beam through the object and WAXS only uses those photons scattered by a few degrees or more. Several tests were performed at the BMIT bending magnet beamline to determine if the technique combination was viable.

## 6.1 WAXS Apparatus

The samples tested at BMIT were water, polyethylene, polymethyl methacrylate (PMMA), and porcine specimens (grocery store pork). Either a 1mm x 1mm pencil beam or a 105mm x 1mm line beam, which could cover the whole sample, was used

for imaging. The energy of the beam was 41keV, which was prepared by a Si(3,3,3) DCM with a 3.5mm aluminum filter inserted into the beam to remove most of the lower energy harmonic at 13.7keV. Images of the DCM beam were taken using a Rad-Icon Remote RadEye $50\mu$m pixel size detector. They showed several inhomogeneities due to stressing of the crystal or surface imperfections not removed by the etching process (See Figure 6.1).
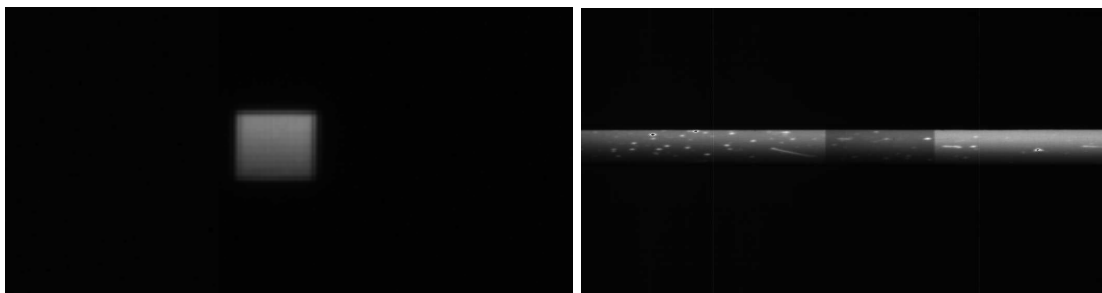


Figure 6.1: Left: An image of the 1mm x 1mm pencil beam. Right: Image of the line beam showing structure in the DCM beam. The shaded center region is due to a piece of PMMA in the beam.

These localized high flux spots in the beam were not an issue for the WAXS experiments as the measured samples were mostly homogeneous and the rings formed from scattering are not significantly altered by an increase in photon bandwidth. Samples were mounted on a vertical scanning stage and held in place with tape. Tungsten blocks were used as a beam stop before the 250mm x 175mm Agfa CR plate, which was used to record the scattering pattern (See Figure 6.2) [Joh09]. The beam stop was needed to ensure no damage was caused to the CR plate from over exposure during long scans. Samples were aligned to reference markers made after a pencil beam was used to expose burn paper to determine beam centre.
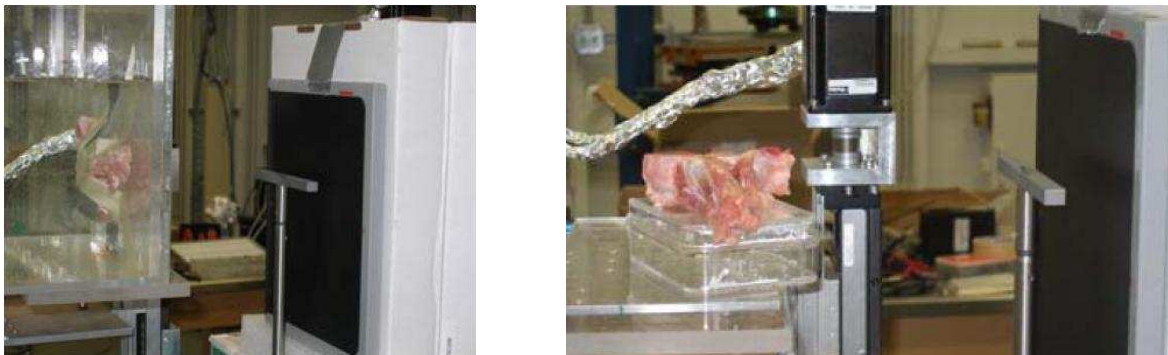
Figure 6.2: Images of the WAXS setup on BMIT with porcine samples

## 6.2 WAXS Measurements

The initial measurements used the 1mm x 1mm pencil beam to limit the sampling area and distortion from overlapping scattering rings. The theoretical photon flux given by equation 3.1 using a storage ring energy of 2.9GeV, and a Y value of 5.47 is $8.6 \text{x} 10^9 \frac{\text{Photons}}{\text{s} \cdot \text{mA} \cdot \text{mr}^2 \cdot 0.1\% \text{bandwidth}}$. The bandwidth of the Si(3,3,3) reflection at 41keV is $0.00826 \times 0.1\%$ bandwidth, and the 1mm x 1mm pencil beam at the rear table in BMIT POE2 has an angular area of $0.00147 \text{mr}^2$. This gives an expected photon flux of $1.04 \text{x} 10^5 \frac{\text{Photons}}{\text{s} \cdot \text{mA}}$.

A 15cm length air filled ion chamber was used to measure the photon flux at the beamline. The total mass attenuation coefficient for air at 41keV is $0.232 \text{cm}^2/\text{g}$, and the partial mass attenuation coefficient for energy deposition at 41keV is $0.053 \text{cm}^2/\text{g}$. The density of air at standard room temperature and pressure is $0.0012 \text{g}/\text{cm}^3$ and from Table 3.1 the average energy to create an electron-ion pair is 34.4eV. Using this information the ion chamber response value $\xi$ may be calculated from equation 3.7 and is $1.82 \text{x} 10^{-19}$C/photon. The voltage measured from the ion chamber electrometer was 2.13V with a gain of 1pA/V and at the time the storage ring held 239mA. Using equation 3.8 the number of photons is N = $1.17 \text{ x } 10^7$ photons/s. Dividing

by the storage ring current gives 0.49 x $10^5 \frac{\text{photons}}{\text{s·mA}}$. To compare with the theoretical value we must divide the measured value by 0.60 to account for the absorption by the 3.5mm aluminum filter, and divide by 0.85 to account for a 6 meter air path within the hutch. This results in a photon flux of 0.96 x $10^5 \frac{\text{photons}}{\text{s·mA}}$ or 92% of the expected value and is taken to be the true photon flux.

Given the low photon flux available it was decided to try exposure times ranging from 5 - 20 minutes to see if scattering rings could be discerned. No usable results were obtained with these parameters so the exposure time was increased to 40 - 60 minutes, which again yielded no usable results. The horizontal collimation of the beam was then removed allowing a 105mm x 1mm beam to cover the whole sample. This ensured that the entire horizontal width of the samples ($\sim$ 5mm diameter) would be involved in scattering and increase the scattering signal. For a nominal exposure time of 60 minutes scattering rings were measured for plastic and water during several exposures (See Figure 6.3). However the rings were blurred in the horizontal direction due to the line beam used on the samples.
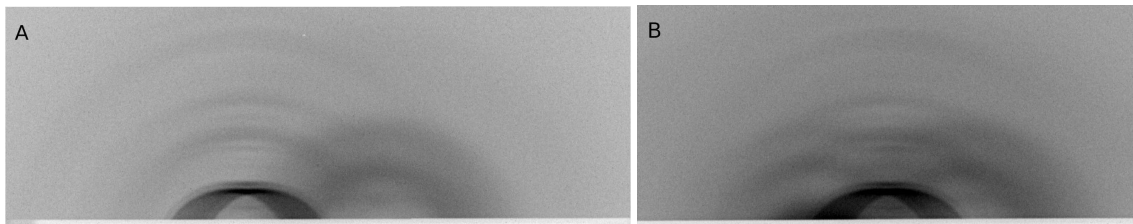


Figure 6.3: A) Polyethylene and water. B) PMMA, Polyethylene, and water

Once differences between water and plastic had been viewed an attempt was made to see the difference in scatter between bone, muscle, and fat. Porcine samples were purchased from a local grocery store and the 1cm cuvettes were filled with each type of porcine material. The scattering results for fat, muscle, and bone are below in

figure 6.4.
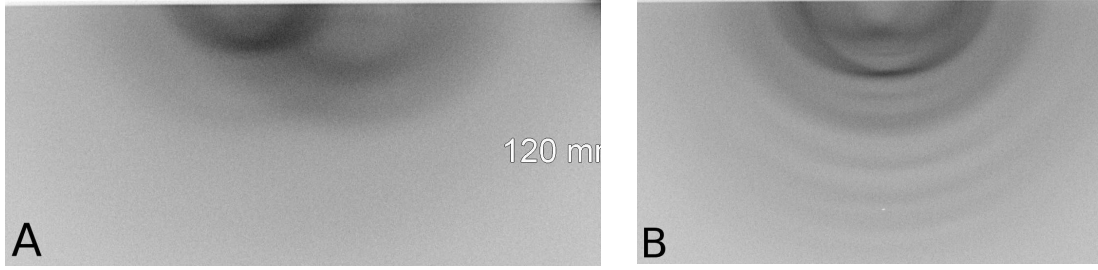


Figure 6.4: A) Scattering from porcine fat and muscle tissue each contained in a 1cm cuvette. B) Scattering from porcine bone contained in a 1cm cuvette [Joh09].

## 6.3  Conclusions

Differences in scattering rings between plastics, water, and porcine materials were evident, but long exposure times to collect images made adding this technique to the XRP system undesirable. The vast increase in exposure time is explained by the interaction cross section for elastic scattering and detector area differences between techniques. As mentioned above the photon flux reaching the object was approximately 50,000 photons per second in a 1mm x 1mm beam spot. Using equation 3.12 the dose rate was $\dot{D} = \frac{50,000 \times 41 \text{keV}}{1\text{mm} \times 1\text{mm}} \cdot 0.223 \text{cm}^{-1} = 7.5 \mu \text{Gy/s}$. For a planar imaging detector with $100 \mu$m pixel size this would suggest 500 photons per pixel in a one second exposure for a 1mm x 1mm detection area. If transmission through the object removes half of these photons from absorption and extinction the remaining 250 photons would give 6.3% statistical error in each pixel for a one second exposure. The interaction strength of elastic scattering is one tenth of the magnitude of the total mass attenuation coefficient and for water at 41keV it is $0.028 \text{cm}^2/\text{g}$ compared to $0.26 \text{cm}^2/\text{g}$ respectively. This means only one tenth of the photons, or five times less than the planar example, arriving at the target are used to form the image. The rest are either absorbed by the sample, hit the beam stop, or Comp-

ton scatter, which would add noise to the image. The difference in detection areas is 1mm x 1mm in the planar case, compared to approximately 71mm x 71mm to cover the scattering rings in the WAXS measurements. In the situation where one tenth of the WAXS detector area contains the elastic scatter rings this would still be 50 times the area as the planar imaging case. The expected photon flux arriving at a $100\mu$m pixel would then be 50,000 photons per second incident flux, divided by 10 for the amount elastically scattered, divided by an active detector area (the radially integrated region of pixels that the ring of WAXS scatter intersects) of $7.2\text{mm}^2 = 50.41\text{photons/mm}^2$ , divided by 100 for a $100\mu$m pixel size. This gives a result of $50,000\frac{\text{photons}}{\text{s}} * 0.1$ probability of elastic scatter$/50.41\frac{\text{photons}}{\text{mm}^2}/100\frac{\text{pixels}}{\text{mm}^2} = 1$ photon per second. Radially integrating the pixels to form the ring pattern would result in an error term that is equal to $\sqrt{\delta\text{x}_1^2 + \delta\text{x}_2^2 + ... + \delta\text{x}_\text{n}^2}$, where $\delta\text{x}_\text{n}$ is the error in pixel n. Thus to obtain an image with similar statistical error as the projection image a much longer exposure time would be needed.

After completion of the WAXS experiment it was decided to pursue fluorescence imaging as the second method to be combined with the XRP version of DEI. The success of the fluorescence imaging during GEMS and the low elastic scattering contribution compared to absorption made fluorescence a favorable choice.

# Chapter 7

# DEI Commissioning

Before the XRP could be included into a DEI system a working apparatus was needed. The BMIT bending magnet beamline where measurements were going to take place was in the construction phase and required several instrumentation and commissioning projects. The following chapter gives an overview of the DEI system commissioning and the imaging projects performed to confirm the reliability of the system.

## 7.1 Monochromator

The DCM for the BMIT bending magnet beamline was first tested in November 2007 at the construction site of the future Synchrotron Laboratory for Micro And Nano Devices (SyLMAND) beamline. Figure 7.1 shows the interior mechanism of the DCM and some of the motor connections. After load issues were temporarily resolved by adding force relieving springs to ensure Bragg and tilt angle motors in the monochromator did not stall, monochromatic beam was successfully passed to the analyzer crystal. Alterations to the monochromator components would be recorded for later implementation in an effort to find a permanent solution. This early test

allowed for LabVIEW control, motor connection issues, and piezo movements for fine angle Bragg adjustments to be resolved before installation on BMIT to reduce commissioning time needed on that beamline.
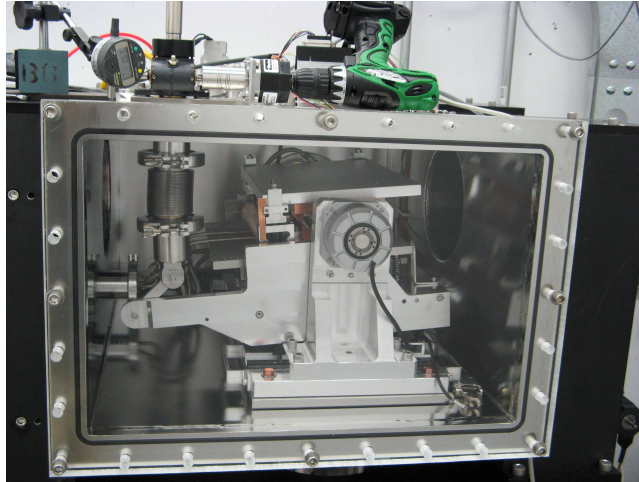


Figure 7.1: BMIT bending magnet DCM installed on the SyLMAND beamline.

In 2008 the monochromator was installed in the BMIT bending magnet beamline with the previous 25N Bragg and tilt motors replaced by a 50N version of the piezoelectric inchworm actuator. The monochromator performed well in the initial trials in December through February 2009. During the December trials, which occurred before water cooling had been installed on the beamline, a Proportional Integral Derivative (PID) control program was implemented in LabVIEW to keep the monochromator tuned at a desired level. It was not possible to keep the monochromator fully tuned at the top of the rocking curve due to stability issues, but 95% of the maximum value was achievable or less if detuning was desired. This monochromator feedback loop to keep the beam intensity stable was implemented in 24 hours. Problems later occurred when two of the new motors failed either from use in a vacuum, which they were not rated for, or from the high radiation levels caused by

the BMIT insertion device beamline commissioning. Even with the failures it was possible to keep the monochromator functional with the operational knowledge and instrumentation experience accumulated to that point.

## 7.2   Bragg Analyzer Setup

The analyzer crystal stand and crystal positioning by servo motors were also examined during the 2007 SyLMAND test. All of the Thorlabs servo motors on the analyzer crystal setup were controlled in LabVIEW using the ActiveX framework, which allowed synchronization between movements and data acquisition. The servo motors in the analyzer crystal setup had $0.1\mu$m position accuracy giving the 1m tangent arm a $0.1\mu$radian angular resolution (See Figure 7.2).
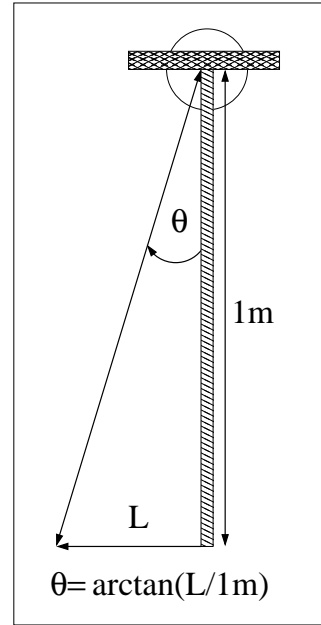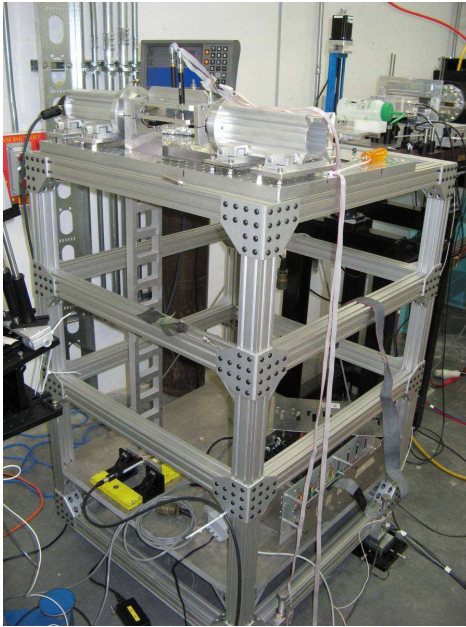


Figure 7.2: The analyzer crystal stand with central hub for holding the crystal plate and a 1m tangent arm for fine angular motions. The diagram on the right shows the design concept where small linear motions at the bottom of the tangent arm cause small angle changes.

After a few days of improving the control software the analyzer crystal was aligned
to diffract the beam prepared by the DCM. Measurements of the Si(1,1,1) at 22keV
and the Si(3,3,3) at 42keV were taken to compare with the theoretical values to de-
termine if any of the crystals were strained. The results shown in Figure 7.3 showed
good agreement between measured and theoretical values indicating the system was
ready for analyzer based imaging.
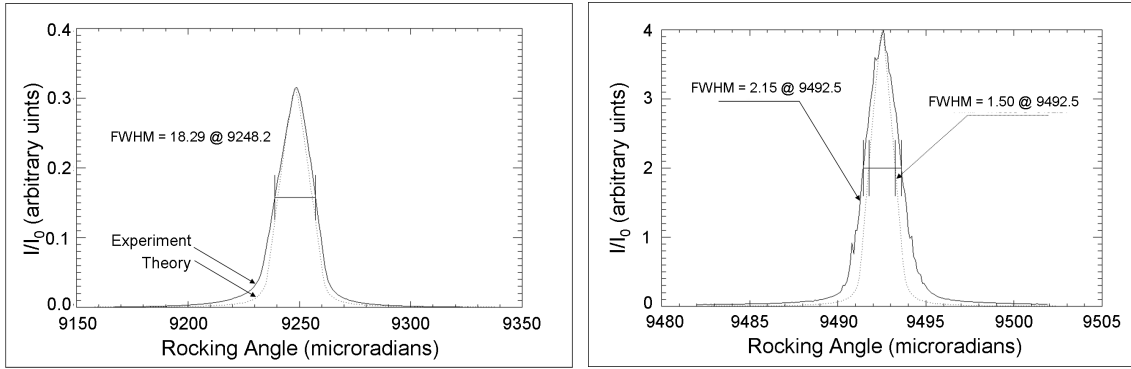


Figure 7.3: A) Comparison of the measured DCM + analyzer rocking curve (solid
line) to the theoretical DCM rocking (dotted line) for the Si(1,1,1) reflection at
22keV. B) Comparison of the measured DCM + analyzer rocking curve (solid line)
to the theoretical DCM rocking (dotted line) for the Si(3,3,3) reflection at 42keV.
Results are typical and show a measured curve slightly larger than the theoretically
predicted curve.

The first test image of the DEI setup was to take an image of a roll of tape at the top
of the rocking curve. This image turned out well (See Figure 7.4) and confirmed the
DEI system was ready whenever it was permitted to be installed at BMIT. Further
imaging tests performed at BMIT are described in the following section.

Additional tests were done in August of 2009 when replacement Si(2,2,0) crystals
were installed in the monochromator and analyzer stand. Again the rocking curve
was checked to confirm the widths were as predicted by theory. The line beam from
the monochromator was then imaged to determine if there were any irregularities

61

Figure 7.4: A picture of the first analyzer based imaging sample and the resulting x-ray image from the SyLMAND tests.

in the prepared monochromatic beam from the crystals (chips, cracks, or strains) used (See Figure 7.5). The beam intensity was uniform and superior to the Si(1,1,1) crystal set used during the WAXS experiments.
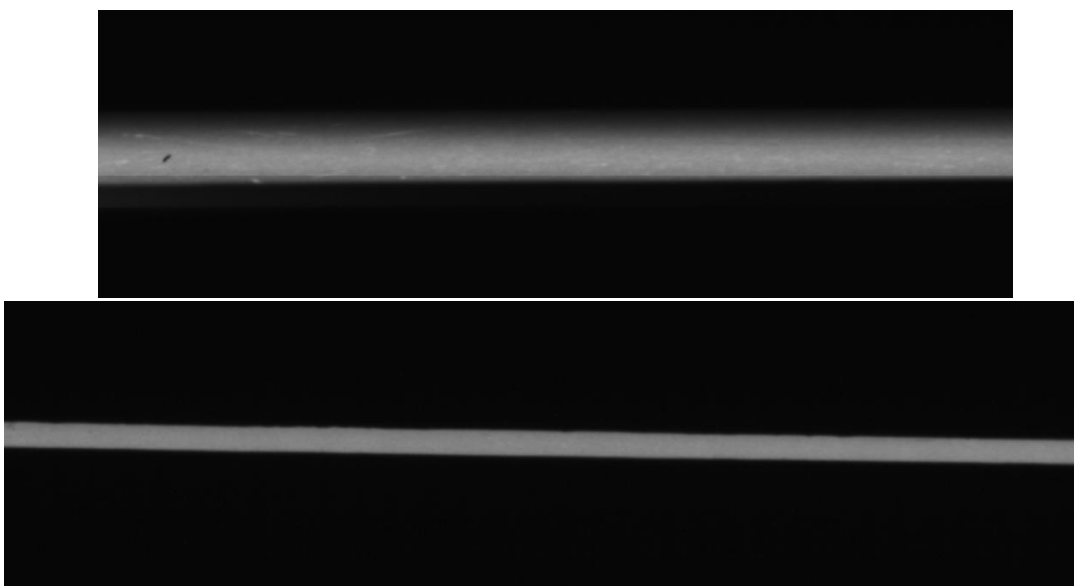


Figure 7.5: The top image is the unapertured beam from the monochromator measured by a $50\mu$m pixel size Rad-Icon detector. The bottom image is the monochromator beam apertured to a 1mm height also measured by the $50\mu$m pixel size Rad-Icon detector.

## 7.3   Images

During the commissioning of the monochromator and analyzer stand on BMIT two test imaging rounds were conducted. The first batch of images taken were of objects that did not require a Bio-safety permit and were convenient to mount in the DEI apparatus. Figure 7.6 shows four of the images acquired of different objects at the top of the rocking curve.
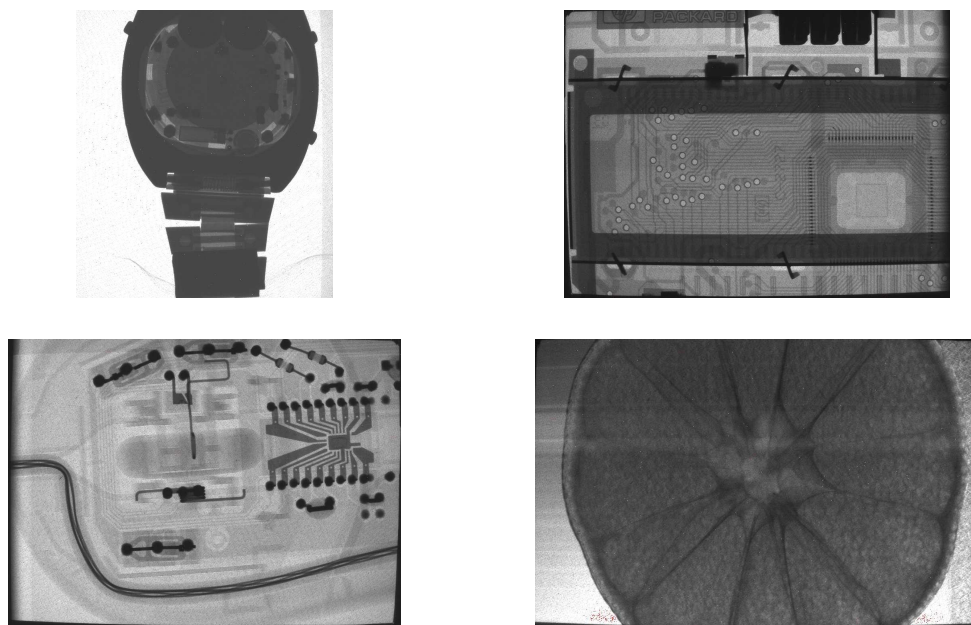


Figure 7.6: Images of commissioning samples. Top Left, a wrist watch. Top right, the display region of a HP calculator. Bottom Left, a computer mouse. Bottom Right, an orange.

The second round of samples were brought in to test the system with biological samples living and non-living. Figure 7.7 shows images from three different samples at the top of the rocking curve.

After successfully imaging at the top of the rocking curve experiments were performed with the crystal alignment on the sides of the rocking curve according to the DEI
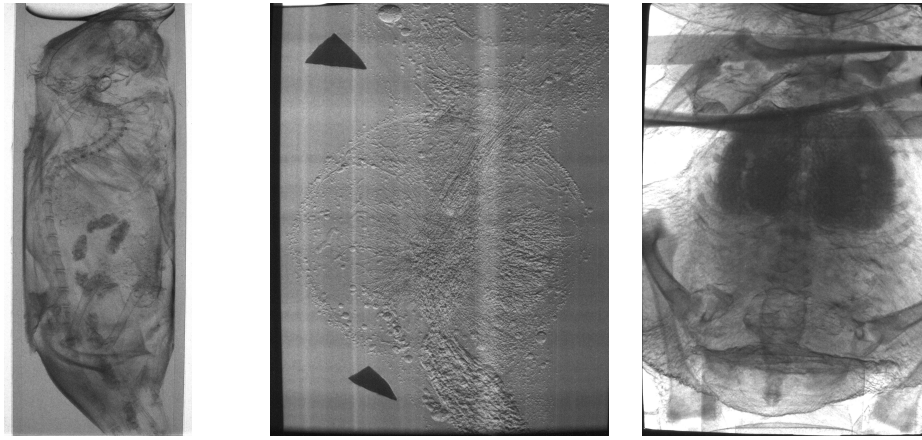
Figure 7.7: Images of biological commissioning samples. Left, a mouse. Middle, a canine prostate. Right, a small chicken.

and MIR methods outlined in Chapter 4. The system was confirmed to be fully operational with the successful completion of a bone density and bone structure study on the human distal radius [Coo10].

# Chapter 8

# X-ray Prism

Descriptions of light refracting through materials has been well established, and also holds true for X-rays [Jam62,Zac45]. X-ray refraction effects have led to the development of imaging techniques which use intensity changes via the reflectivity of crystals as a contrast mechanism and include DEI, ABI, and MIR [Cha97, Wer03]. The difficulty in all of these techniques is the precise alignment of the crystals involved so that the data points collected on opposite sides of the analyzer rocking curve are symmetric or at known asymmetric locations. If the analyzer crystal in such a measurement is out of alignment by a few $\mu$radians or less, the necessary adjustment can be achieved using an XRP to alter the path of X-rays by the appropriate refraction deviation. To date the only previous work with XRP's has been to remove harmonics from DCMs [Zho00,Rig02]. The application of an XRP may also be used to change the path of a particular X-ray energy by a refraction deviation angle that will achieve alignment of crystal rocking curves while simultaneously misaligning the harmonic energies contained in the X-ray beam. The amount of angular change at the XRP's surface can be calculated using Snell's Law, $n_1 \ \sin(\theta_1) = n_2 \ \sin(\theta_2)$, where $n_1$ and $n_2$ are the refractive indices of the two materials that form a surface boundary, and

$\theta_1$ and $\theta_2$ are the angles from the surface normals (Figure 2.5). If the boundary is between air and a second material the angle change predicted is closely approximated by equation 2.2, $\Delta\theta = \alpha \ \tan(\theta)$. Where $\Delta\theta$ is the angle deviation of the beam in the material from the path in air, and $\alpha$ is the real part of the refractive index correction for the second material. The index of refraction for a material is given by,

$$n = 1 - \alpha + i\beta \qquad (8.1)$$

Where n is the refractive index for the material, $\alpha$ is the real part of the refractive index correction, and $\beta$ is the imaginary part of the refractive index correction. In terms of a time independent plane wave the wave equation $\Psi(x)$ becomes

$$\Psi(x) = A_o e^{ikx} = A_o e^{ink_o x} = A_o e^{i(1-\alpha)k_o x} \cdot e^{-\beta k_o x}$$

where the first term is responsible for refraction and the second for absorption. The transmitted intensity through a material can be determined from

$$I(x) = \Psi(x)^* \cdot \Psi(x) = A_o^2 e^{-2\beta k_o x} = A_o^2 e^{-\mu x}$$

where $A_o$ is an amplitude constant, $k_o$ is the wavenumber, and $\mu$ is the linear attenuation coefficient for the material.

The real part of the refractive index correction can be expressed as $\alpha = r_e \lambda^2 \rho_e / 2\pi$. Where $\rho_e$ is the electron density, $r_e$ is the classical electron radius, and $\lambda$ is the X-ray wavelength [Als01]. The refraction index correction equation may also be written as $\alpha = \frac{r_e \lambda^2}{2\pi u} \frac{Z}{A} \rho$ as shown in equation 2.3 where Z is the atomic number, A the atomic mass, $\rho$ the mass density, and u the unified atomic mass unit. For a composite object

with n elements the equation becomes $\frac{\alpha}{\rho_{comp}} = \sum\limits_{i=1}^{n} f_i \frac{\alpha}{\rho_i}$ where $f_i$ is the mass fraction of element i, and $\frac{\alpha}{\rho_i}$ is the real part of the refractive index correction for the $i^{th}$ element divided by density of the $i^{th}$ element.

The following sections will describe the design, construction, and test measurements of an XRP for the purpose of aligning a DEI system using the fundamental principles reviewed above.

## 8.1 Design of the X-ray prism

### 8.1.1 Refraction Constraints

From equations 2.2 and 2.3 there are only two parameters that can be used to vary the refraction deviation angle $\Delta\theta$ at a given wavelength, the density composition (Z/A) of the prism, and the angle of incidence between the X-rays and the prism surface. The other terms are constant, or are held constant by using a monochromatic beam. Designing an X-ray prism using density changes to vary the angle of refraction has disadvantages: 1) the refraction deviation angle changes linearly with density so a large density change would be needed to cover a wide range of angles; 2) increasing the density of the prism object will cause increased absorption of X-rays for larger refraction deviation angles; and 3) a rigid object with a smoothly changing density gradient is difficult to construct. Thus changing the angle of incidence between the X-ray beam and the object is the simplest way to design the prism object. By increasing the $\theta$ angle between incoming X-rays and the prism surface the refraction deviation angle increases by the tangent of $\theta$. An object where X-rays can go from a small angle to angles close to $\pi/2$ radians would create a sizable range

of associated refraction deviation angles. This places the first constraint on the design, that the angle between the prism and the photon beam be adjustable and have a uniform angle across the area of the prism intersected by the incident photon beam.

## 8.1.2   Double Crystal Rocking Curve Constraints

For the XRP to be useful it must be able to cause a large enough angle deviation from the incident direction to span the range of analyzer angles that would be used in an Analyzer Based Imaging (ABI) system. The angular range of the monochromator and analyzer combination (monochromator crystal angles fixed) can be characterized by the Darwin width or the Full Width at Half Maximum (FWHM) of the analyzer rocking curve intensity, which are both dependent on the crystal reflection and X-ray energy. Equation 8.2 gives the calculation for determining the Darwin width.

$$\omega_D = \frac{2r_e \ \lambda \ d_{hkl} \ |F_{hkl}|}{\pi \ V_c \ Cos(\theta_B)} \tag{8.2}$$

Where $d_{hkl}$ is the crystal lattice spacing, $F_{hkl}$ is the structure factor, $V_c$ is the unit cell volume, and $\theta_B$ is the Bragg angle [Als01]. The FWHM of the analyzer rocking curve is determined from the calculated intensity profile as in figure 8.1 using dynamical perfect crystal diffraction theory. Table 8.1 lists the theoretical FWHM for several common crystal reflections in $\mu$radians for a silicon DCM and analyzer at 41keV and 25keV.

Since the intended purpose of the XRP is for DEI or MIR measurements the crystal reflections typically used are the Si(3,3,3) or the Si(4,4,0). Both reflections have
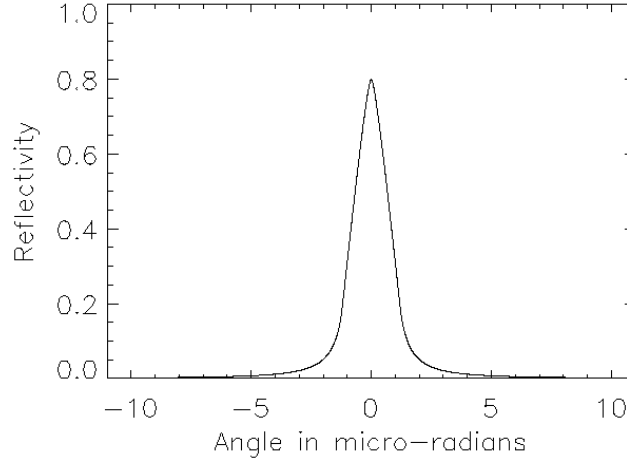
Figure 8.1: Rocking curve of a Si(3,3,3) double crystal monochromator at 41keV [Jam62, Zac45].

narrow peak widths, which provide sensitivity to density gradients in the object of interest by the rapid change in intensity with a small deviation in angle from refraction. These changes in intensity form the contrast in resulting DEI images. From table 8.1 the range that the XRP will need to cover is a minimum of $2.83\mu$radians for the Si(3,3,3) or $3.42\mu$radians for the Si(4,4,0). This will permit measurements to be taken at both sides of the analyzer reflection (at 25keV or higher) at the half maximum points, which is the minimum data set that is required for DEI. If possible the available range of refraction deviation angles should be larger such that twice the FWHM or more could be covered. This allows for measurements further down the analyzer rocking curve to be taken for DEI or MIR.

### 8.1.3 Geometric Constraints

It is necessary to determine the required size of the XRP. Figure 8.2 shows how the length of the XRP object can be calculated by taking the beam height and dividing

| Si | DCM FWHM | ($\mu$radians) |
|:---:|:---:|:---:|
| (hkl) | @ 41 keV | @ 25keV |
| 1,1,1 | 9.08 | 14.94 |
| 2,2,0 | 6.27 | 10.34 |
| 3,3,3 | 1.69 | 2.83 |
| 4,4,0 | 2.03 | 3.42 |

Table 8.1: Angular widths of various Silicon crystal reflections

by the cosine of the largest angle of incidence required to form the desired refraction

deviation angle range.
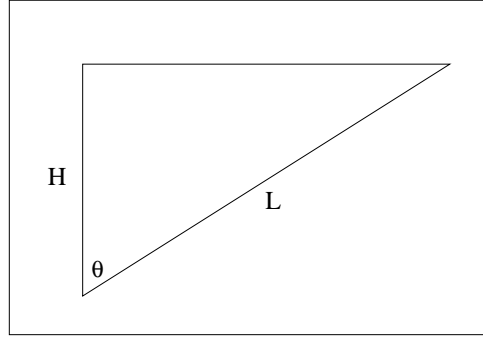


Figure 8.2: The length of X-ray prism needed for a given beam height can determined from the shown geometry. Where H in the diagram is the height of the incident beam. Length = Height$/\cos\theta$

For a 1mm tall beam, a refraction range of 6$\mu$radians, fixing the energy as 41keV, and using PMMA as the prism material the minimum length required can be calculated by $L = H/\cos\theta$ and the refraction range by equation 2.2 (See below).

$$\Delta\theta = \alpha \ \tan(\theta)$$

$$\Rightarrow \text{Refraction Range} = \alpha \ \tan(\theta)$$

$$= 0.159 \times 10^{-6} \cdot \tan(88.5°)$$

$$= 6.07 \times 10^{-6} \mu\text{rad}\Big|_{41\text{keV}}$$

70

$$\text{XRP Length} = \text{Beam Height} \: / \cos \theta$$

$$= 1\text{mm}/\cos(88.5°)$$

$$= 37.8\text{mm}$$

For a Si(4,4,0) DCM and analyzer combination the refraction range would cover 3.0 FWHM at 41keV or 1.8 FWHM at 25keV. For a Si(3,3,3) DCM and analyzer combination the refraction range would cover 3.6 FWHM at 41keV or 2.1 FWHM at 25keV. Figure 8.3 shows the width of the DCM rocking curves as a function of energy.
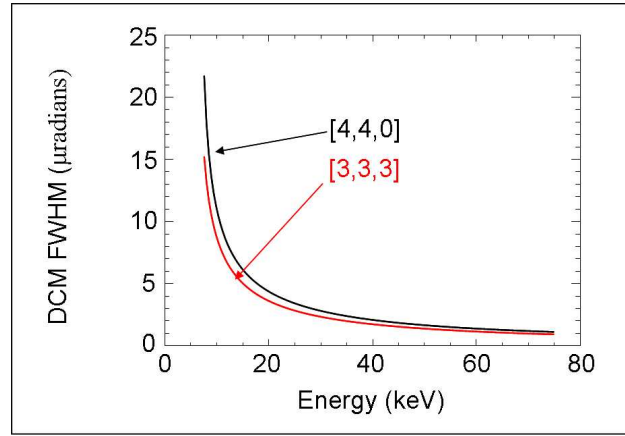


Figure 8.3: Plot of the theoretical DCM FWHM for Si[3,3,3] and Si[4,4,0] as a function of energy.

To allow for error in the centering of the beam on the XRP the total length was increased from 37.8mm to 50mm. The second geometric constraint is the width of the beam being used. If a pencil beam is used to raster scan across the object the XRP could have a small width, but if a large fan beam is used to measure the object the XRP will need to be wide enough to accept the full apertured beam. During the GEMS experiments a 5cm beam was used so the trial XRP was made to accommodate the same beam width.
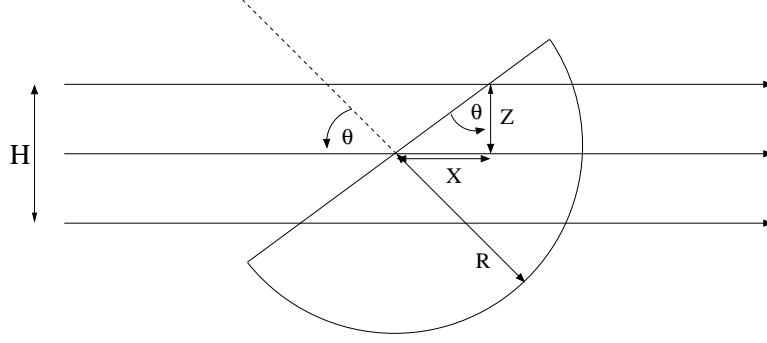
Figure 8.4: Diagram of rays passing through the XRP. It should be noted that X-rays pass through the circular portion of the XRP at or close to normal angles leading to minor or no refraction angle deviations.

Due to the half circle geometry of the XRP the average absorption will change slightly depending on the angle used. To determine the formula for the average absorption through the XRP an assumption is made that the beam height is much smaller than the diameter of the XRP (H≪R), and that the refraction angle deviation is small ($\Delta\theta_{\mathrm{ref}} \ll 1$). From Figure 8.4 the difference in path length is given by X, where $\tan\theta = \frac{X}{Z} \Rightarrow X = Z \cdot \tan\theta$. The number of photons that are transmitted through the XRP with radius R and angle $\theta$ is given by $N(\theta) = N_{\mathrm{o}}e^{-\mu\cdot(R\pm X)}$.

If the height of the beam is integrated over we find the expression for calculating the average number of photons transmitted through the XRP.

$$N = N_{\mathrm{o}} \int_{-h/2}^{h/2} e^{-\mu\cdot(R-Z\cdot\tan\theta)}dz$$

$$\overline{N} = \frac{N_{\mathrm{o}} \int_{-h/2}^{h/2} e^{-\mu\cdot(R-Z\cdot\tan\theta)}dz}{\int_{-h/2}^{h/2} dz} \Rightarrow \overline{N} = \frac{N_{\mathrm{o}}\cdot e^{-\mu R}}{h} \cdot \int_{-h/2}^{h/2} e^{\mu\cdot Z\cdot\tan\theta}dz$$

$$\overline{N} = \frac{N_{\mathrm{o}}\cdot e^{-\mu R}}{h\mu\tan\theta} \cdot e^{\mu Z\tan\theta}\Big|_{-h/2}^{h/2} = \frac{N_{\mathrm{o}}\cdot e^{-\mu R}}{h\mu\tan\theta} \cdot \left(e^{\mu h\tan\theta/2} - e^{-\mu h\tan\theta/2}\right) = \frac{2N_{\mathrm{o}}\cdot e^{-\mu R}}{h\mu\tan\theta} \cdot \sinh\left(\mu h\tan\theta/2\right)$$

For the constructed XRP and the photon beam used the values are: R = 2.5cm; h=0.1cm; and $\mu_{\mathrm{pmma}}(41\mathrm{keV})$=0.27335cm$^{-1}$. Using this information the expression may be evaluated at any rotation angle $\theta$. The maximum angle where the beam just fits on the XRP is given by, acos $\theta = \frac{0.1/2}{2.5} \Rightarrow \theta = 0.4936\pi$. The difference in average absorption between the minimum angle and the maximum angle is $\overline{N}(\theta = 0) = 0.5049 \cdot N_o$ compared to $\overline{N}(\theta = 0.4936\pi) = 0.5446 \cdot N_o$ or a change of approximately 8%.
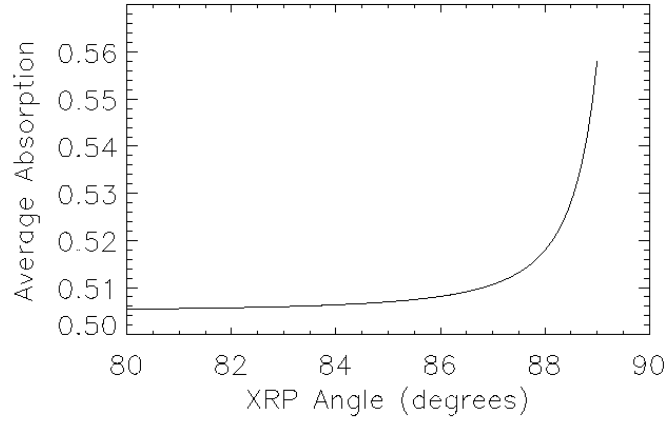


Figure 8.5: Plot of the average absorption of the XRP for different orientations at 41keV photon energy.

A plot of the average absorption for larger angles is shown in Figure 8.5. Smaller angles all have an approximate one half average attenuation value for the XRP made of PMMA and using a 41keV X-ray energy. If local variations of intensity within the height of the beam are considered there is a significant change across the beam for large angles. At the largest possible angle where the whole surface of the XRP is intersected by the beam X-rays will travel through 5cm of PMMA at one edge and approximately zero thickness at the other edge. This will cause a significant range

of intensity values over the height of the beam, which is plotted in figure 8.6 for a 1 mm tall beam and a 5cm diameter XRP.
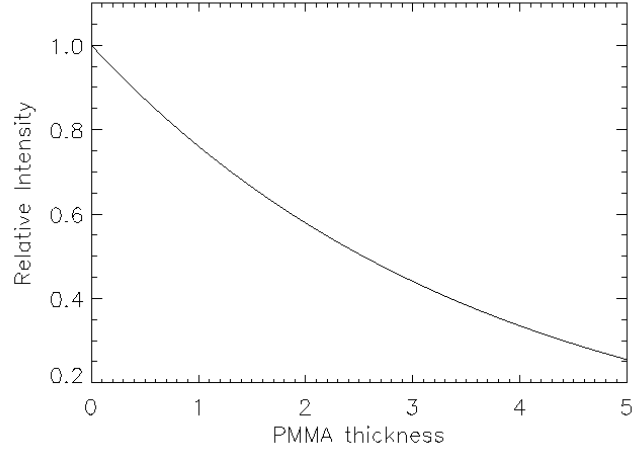


Figure 8.6: Path length through the XRP from 0 to 5cm versus the relative transmitted intensity at each location.

It is therefore favorable to use a vertical raster scan or vertical line scan so that the beam intensity over the object is averaged. Otherwise the number of photons probing the sample vertically will depend on the XRP angle and the vertical distance of the sample location from center of the beam height. To minimize this effect of the XRP on the beam profile the radius of the XRP should be as small as possible thereby reducing the difference between the maximum and minimum path length through the XRP. The trial XRP design was for a 1mm tall beam, but a 0.5mm tall beam height would allow the XRP radius to be halved and still keep the same range of angle deviations with less absorption of the incident photon beam.

## 8.1.4 Construction Material Constraints

Candidate materials for the XRP are required to be solid, easily molded or machined, and should have a density as low as possible so that absorption does not become excessive. In figure 8.7 several materials are compared to find the best possible XRP material. The plot shows which material absorbs the least and still delivers an angle range of three times the FWHM of the DCM rocking curve as a function of energy. At low imaging energies (<30keV) the best XRP material would be beryllium, and at higher imaging energies (>30keV) the best XRP material is beryllium oxide. For the following figures the color code for materials is;1) Black = Be; 2) Magenta = BeO; 3) Green = BN; 4) Blue = PMMA; 5) Red = $Si0_2$; 6) Cyan = Al; and 7) Yellow = Cu.
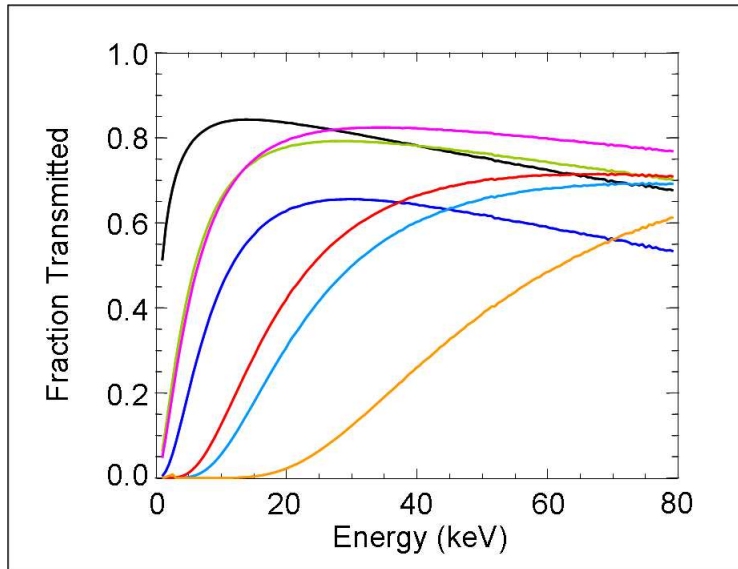


Figure 8.7: Transmission through an XRP giving three times the DCM FWHM in angle range for various materials.

To determine the size of XRP that would be needed for each material figure 8.8 shows the minimum diameter of a half circle necessary to achieve three times the [4,4,0] DCM FWHM angle range, and figure 8.9 plots the real refractive index correction

divided by the linear attenuation coefficient for the each material.
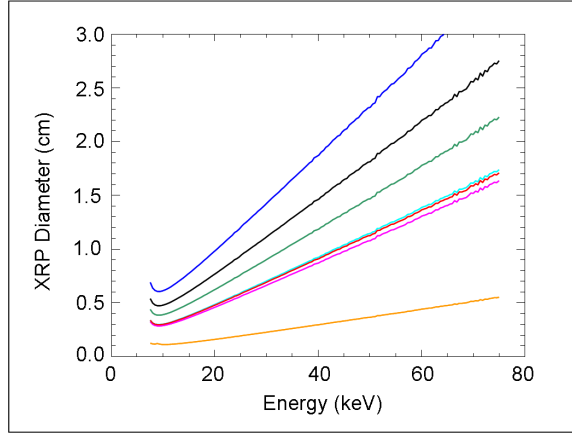


Figure 8.8: Comparisons of the XRP diameter needed for three times the [4,4,0] DCM FWHM angle range as a function of energy for several materials.
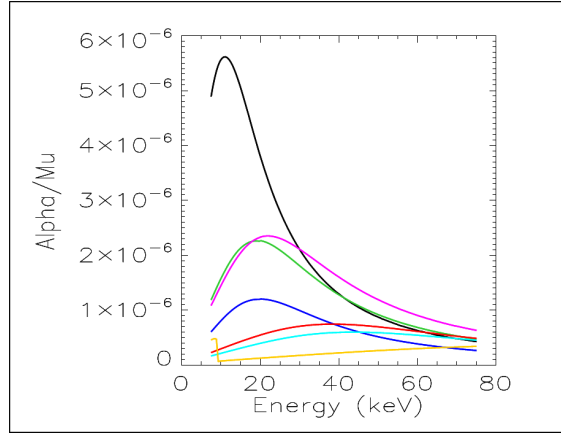


Figure 8.9: Comparison of real refractive index corrections divided by the linear attenuation coefficient as a function of energy for several materials. Materials with a higher value get a larger refraction deviation for the transmission loss caused by X-rays going through the XRP.

After considering the predictions for various materials plastic was chosen as the best candidate. Plastic provided a versatile range of operational energies for imaging and is easy to form into the necessary shape. The material considered next best would be aluminum as it is also an excellent construction material and would provide better transmission values than plastic above 45keV. Other materials with larger transmission values would be much more expensive and difficult to machine into the desired XRP shape, but do have the potential for a superior angle deviation for the amount of X-ray attenuation occurring in the prism. The mass attenuation coefficient of PMMA for several X-ray energies and the real part of the refractive index correction for the same energy range is plotted in figure 8.10.
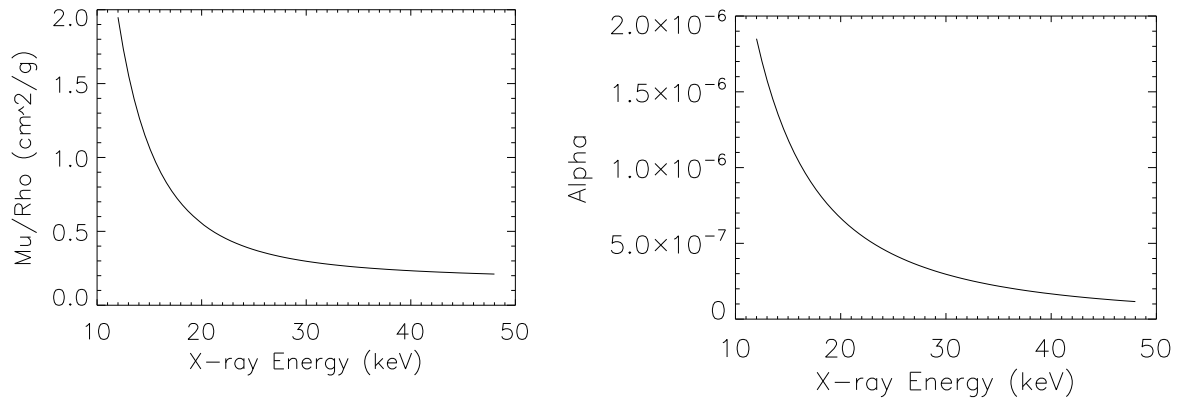


Figure 8.10: Left: Mass attenuation coefficient for polymethyl methacrylate for X-ray energies between 12keV and 48keV. Right: Real refractive index corrections for polymethyl methacrylate for X-ray energies between 12keV and 48keV.

### 8.1.5 Computer Assisted Design and Printing of the X-ray Prism

With the material and range of incident angles required for a DEI measurement determined the XRP was constructed. The software package SolidWorks (Dassault

Systèmes, SolidWorks Corp.) was used to design the XRP. The last important consideration is to ensure X-rays leave without any additional refraction deviation at the exiting surface once they have been deviated to the desired angle by the entrance surface of the XRP. It is possible to construct an XRP that uses the combined refraction deviations from several surfaces to define the final angle, however the current design is restricted to a single surface for the simplicity of determining the total refraction deviation by measuring the angle of one surface to the direction of the incident beam using equation 2.2. To achieve as little refraction deviation as possible on the exiting surface the design incorporates a half circle so that X-rays leaving (or entering) this surface will be incident to the surface at, or close to, a right angle giving a negligible refraction deviation. Figure 8.11 shows the XRP and consists of a half circle 50mm in diameter and a hub for rigid coupling with a Thorlabs NR360S/M rotation stage (Thorlabs Inc.). The XRP was fabricated using a Eden500VTM rapid prototyper (Objet Geometries Inc.) with FullCure720, an acrylic-based transparent photopolymer material. The 3D print of the XRP was then polished to ensure a uniform surface and mounted. The tangent arm system design that the XRP will replace is shown in figure 8.11 on the right.

## 8.2 Measurements with the XRP at fixed angles and the analyzer moving in angle

### 8.2.1 XRP viability test

The original print of the XRP using the rapid prototyper was in an opaque plastic resin that appeared white. Concern arose that this plastic would cause considerable
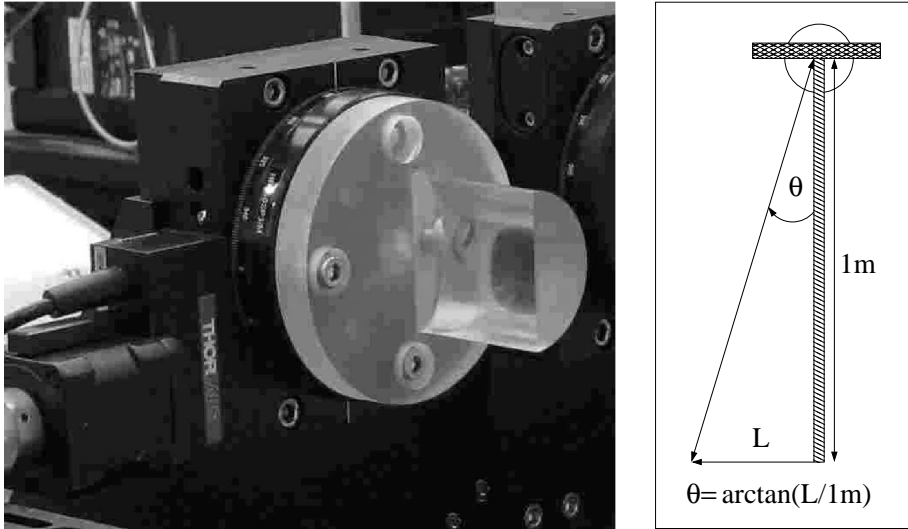
Figure 8.11: Left: The completed XRP after printing, polishing, and mounting to a Thorlabs NR360S/M Nanorotator stage is 19cm x 11.5cm x 5cm. Right: The tangent arm system that the XRP will replace stands 132cm x 56cm x 60cm.

scattering of X-rays through the XRP so a second XRP print was done in a transparent plastic as DEI imaging of transparent plastic rods in previous work showed negligible scattering. Before the XRP was used in an ABI system it was decided to confirm that the XRP was not going to be a significant source of scattering, which would degrade image quality. The Bragg geometry DEI setup at BMIT was used to image the XRP to look for significant extinction of the primary beam through the XRP. Images were taken using a VHR-90 X-ray Camera (Photonic Science, East Sussex, UK) with gadolinium oxysulphide scintillator layer having a density of 7.5mg/cm$^2$ and area of 74.9mm x 49.9 mm (4008 x 2672 pixels) with optical pixel size of 18.7$\mu$m. Figure 8.12A shows an image of just the XRP, and Figure 8.12B shows the XRP with a piece of polystyrene foam for scatter comparison. Unlike the polystyrene foam the XRP does have uniform grey scale absorption levels for regions in the image with similar thickness. Additional measurements with an angular alignment several FWHM away from the peak of the rocking curve showed no intensity reversal in the XRP images like in the polystyrene foam where scattered photons are

79

dominant in the image.
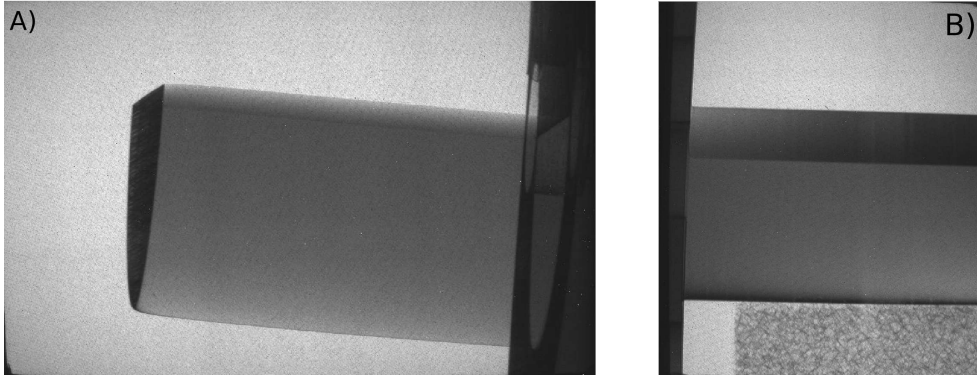


Figure 8.12: A) Image of the XRP at the top of the rocking curve with Bragg crystal geometry. B) Image of the XRP and polystyrene at a 1/2 FWHM point on the rocking curve.

## 8.2.2 Refraction measurements

To determine if the XRP produced the theoretically predicted refraction the following experimental setup was used: 1) the Si(3,3,3) DCM from the BMIT (1.34T bending magnet) beamline at the CLS to prepare a 41keV X-ray beam; 2) a 15cm plate length ion chamber detector filled with Argon gas at atmospheric pressure to measure the incident flux; 3) the XRP mounted to a NR360S/M Nanorotator motorized stage (Thorlabs, Newton, NJ, USA); 4) a single Si(3,3,3) analyzer crystal (in Bragg diffraction geometry) mounted to a 1m long tangent arm driven by a Z625B 25mm encoded motion servo motor (Thorlabs, Newton, NJ, USA); and 5) a 15cm plate length ion chamber detector filled with Argon gas at 1atm pressure to measure the transmitted flux (See Figure 8.13).

Measurements began by tuning the monochromator using the first ion chamber. A reference position of the analyzer crystal rocking curve peak was then measured by
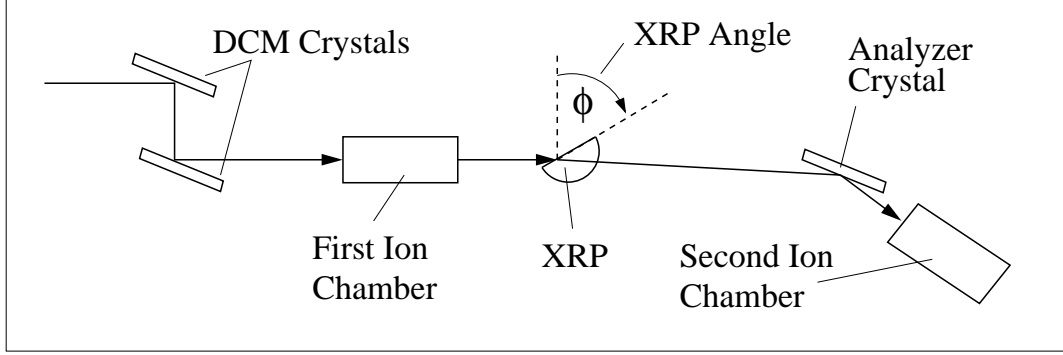
Figure 8.13: Apparatus outline for the refraction measurements on the BMIT bending magnet beamline.

scanning the servo on the tangent arm in $0.1\mu$m steps providing $0.1\mu$radian increments in Bragg angle. At each servo position the ion chamber voltages were recorded so that the rocking curve peak position could be determined by fitting the voltage data with respect to the servo motor coordinate reference frame. The same servo scan and voltage data fit was performed when the XRP was put into the X-ray beam at a variety of angles to measure the X-ray deviation using the servo position as the reference frame. Complete separation of the Si(3,3,3) (FWHM 1.69$\mu$radians @41keV) and Si(4,4,4) (FWHM 0.98 $\mu$radians @54.7keV) harmonic only occurs at angles larger than 85 degrees (See figure 8.14), but angles smaller than this were still tested relying on the eight fold intensity difference between the Si(3,3,3) and the Si(4,4,4) reflections to ensure that the Si(3,3,3) dominated the measured peak position. The lower 13.7keV Si(1,1,1) reflection would be removed by attenuation, and higher harmonics would be progressively less intense than previous ones due to the decrease in spectral content from the 7.5keV critical energy source and ever decreasing bandwidths from higher order reflections.
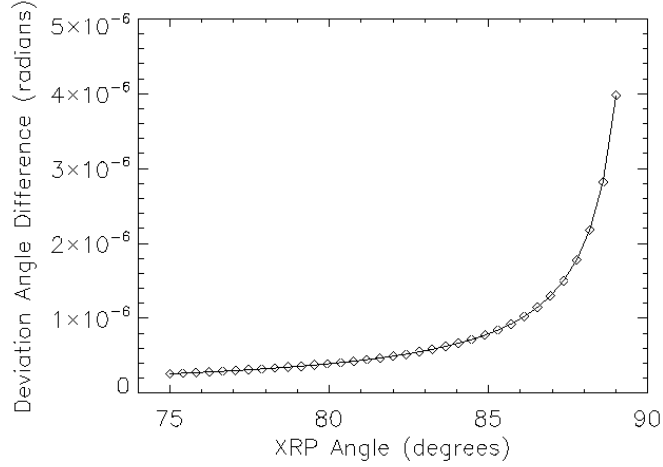
Figure 8.14: Plot of the XRP angle versus the refraction deviation angle difference between the Si(3,3,3) [41keV] and Si(4,4,4) [54.7keV] crystal reflections.

For the first set of refraction measurements analyzer rocking curve peak position was measured with the XRP moved out of the X-ray beam before each angle of the XRP was measured. This reference measurement was done to track any drift in the DCM, which was not temperature controlled. The refraction caused by the XRP is taken as the relative difference of the peak position from the reference measurement before each angle and the subsequent XRP measurement. A Gaussian $\left(G(x) = \frac{1}{\sqrt{2\pi}\sigma}\exp(-\frac{(x-\mu)^2}{2\sigma^2})\right)$ and a Lorentzian $\left(L(x) = \frac{1}{\pi}\frac{\frac{1}{2}\cdot\Gamma}{(x-x_o)^2+(\frac{1}{2}\cdot\Gamma)^2}\right)$ were fitted to the voltage data and servo position to find the analyzer rocking curve peak. This is because the crystal rocking curve is best described as a combination of the two types of curves. It was found however, that the center of the two curves differed by $0.1\mu$radians or less, so that any combination of the two curves would lead to the same peak center. Therefore the results will be reported using only the Gaussian fits of the second ion chamber voltage versus the servo position.

Figure 8.15 shows the absorption corrected refraction deviation data of the first mea-

82

surement and a line which represents the theoretically predicted angle change for a PMMA XRP at 41keV for the respective angles. There is good agreement between the measured values represented by crosses and theoretical values shown by the line through the data.
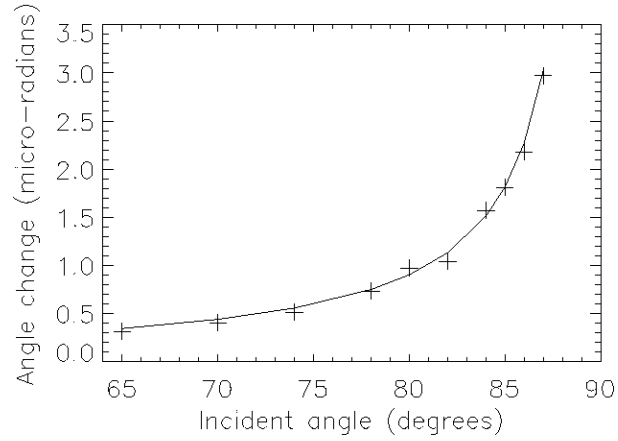


Figure 8.15: Measured refraction from the first refraction data set and the theoretically predicted curve.

The second set of refraction measurements had only one reference measurement of the analyzer rocking curve with the XRP removed and was taken at the beginning of the data set. All of the different angular positions for the XRP were then measured rapidly in turn. As before, ion chamber voltages and servo position were recorded and a Gaussian fit determined the center of the measured rocking curve peak. The difference between the reference position taken at the beginning and each XRP position is plotted in figure 8.16, as well as a line showing the theoretical values for each position. Again there is good agreements between the measured and theoretical predicted values.
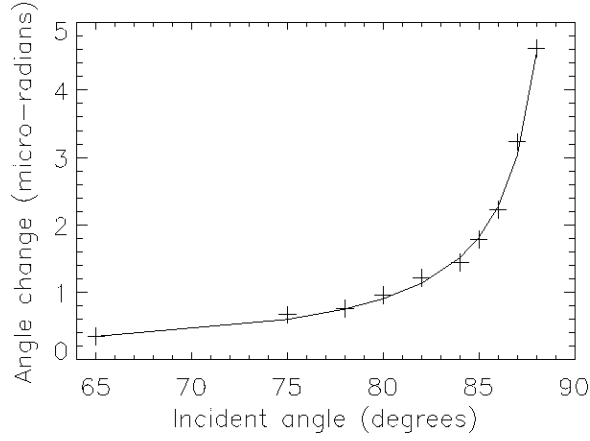
Figure 8.16: Measured refraction from the second refraction data set and the theoretically predicted curve.

## 8.3 Measurements with the XRP moving in angle and the analyzer angle fixed

### 8.3.1 Scanning through the DCM Si(3,3,3) rocking curve

The next test was to confirm that the XRP can cause enough refraction to scan through several FWHMs of the Si(3,3,3) reflection at 41keV as was calculated during the design. For this measurement the XRP was rotated to the starting position and then the analyzer crystal and XRP system was detuned to the desired spot on the side of the rocking curve using analyzer fine angle adjustments. The XRP was then rotated with a constant velocity of 1.25 degrees from 86.85 to 88.85 degrees measured from the surface normal while the voltages of the ion chambers were measured. This scan range at large angles was used because a small motion of 2.0 degrees caused a $5.0\mu$radian change or 3.0 FWHM travel over the DCM rocking curve. The expected reflectivity at each position of the XRP in angle is plotted in figure 8.17. The

theoretical reflectivity was calculated from $\text{Ref}(\theta_{\text{XRP}}) = \text{RefDC}(\theta_{\text{i}} + \Delta\theta)\big|_{\Delta\theta = \alpha \cdot \tan\theta_{\text{XRP}}}$,

where the Ref is the reflectivity of the DCM and analyzer system with XRP set at the angle $\theta_{\text{XRP}}$, RefDC is the Bragg double crystal reflectivity, $\theta_{\text{i}}$ is the starting point on the side of the rocking curve, and $\Delta\theta$ is the refraction deviation angle. The second plot of figure 8.17 is the voltage data from the second ion chamber after the analyzer crystal versus the position in angle of the XRP. It is apparent that the asymmetry in the measured peak is due to the tangent dependence in the refraction deviation angle seen in equation 2.2.
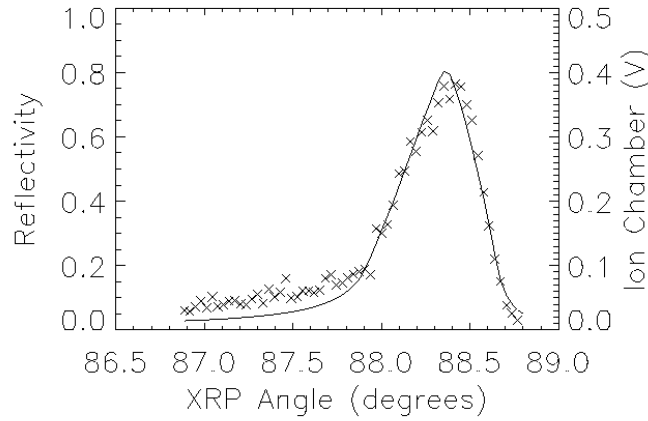


Figure 8.17: Measured asymmetric data of the analyzer rocking curve plotted versus the theoretically predicted curve.

To check that the asymmetry in figure 8.17 was entirely from the tangent dependence the XRP was rotated from a X-ray incident angle starting position of 45 degrees on the flat refracting surface to a 135 degree angle where the X-rays now entered the XRP through the circular portion of the device and exited through the flat surface of the XRP (See figure 8.13). First the analyzer crystal was tuned to the top of the reflection peak before the motion started. The resulting refraction during the rotation caused the alignment to go from the top of the peak down the side of the

rocking curve and then back up the same side returning to the peak. Figure 8.18 shows the plot of the measurement with the peak in the center being the X-rays that passed over top of the XRP while the surface was parallel with the beam. When the same range of angles are used to measure each side of the DCM reflection, as in figure 8.18, the measured peak had the expected symmetry.
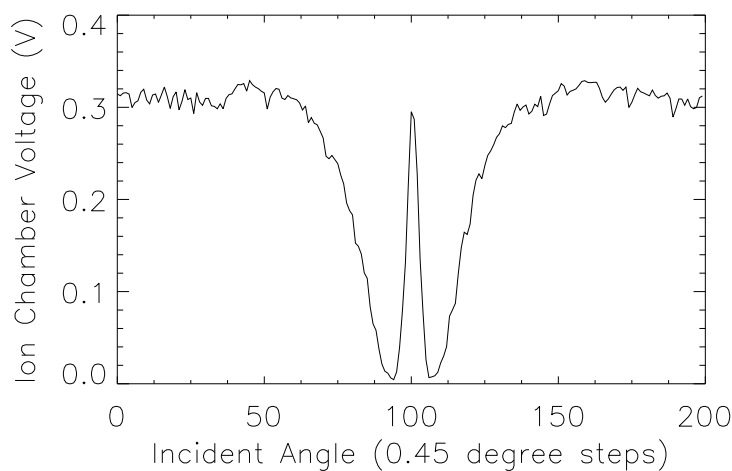


Figure 8.18: A scan down and back up the Si(3,3,3) rocking curve starting with the monochromator tuned. The XRP rotation causes movement down the side of the rocking curve peak and then back up the rocking curve.

## 8.3.2   Few point versus many point analysis for rocking curve measurements

To compare the errors associated with using an increasing number of points on the rocking curve in relation to the traditional method of using only a few points to approximate the rocking curve a simulation was completed using IDL (ITT, Boulder, CO, USA). The imaging dose was kept constant regardless how many points on the

rocking curve were measured by keeping the integrated number of photon counts constant. This means that if only a few points were used the photon count value would be large at each point. However, if many points were used the average photon count per point would be lower.
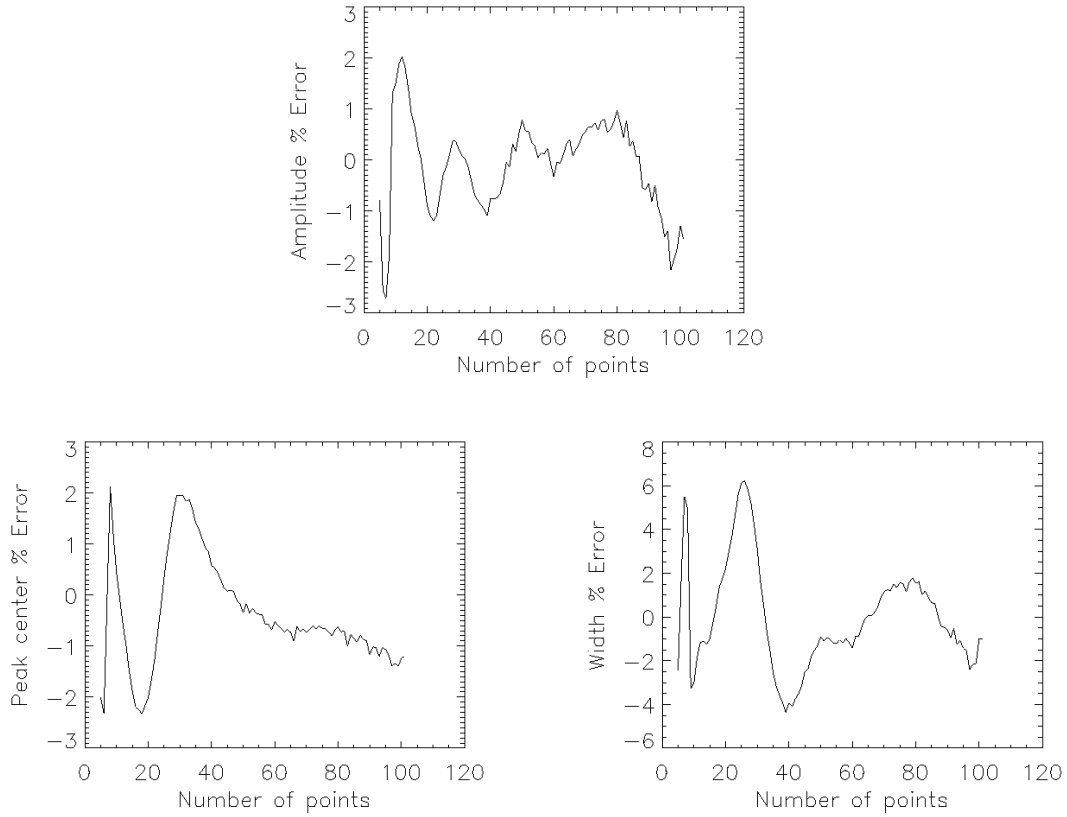


Figure 8.19: The percent error in the Gaussian fit amplitude compared to the actual amplitude. The percent error in the gaussian fit peak center compared against the width of the rocking curve. The percent error in the Gaussian fit width compared to the intended width.

To approximate detector noise a random Poisson distributed variation was added to the amplitude factors for the calculated rocking curve data centered around a magnitude of $N = N_{total}/n_{points}$. Where $N_{total}$ was 10,000 photons, and $n_{points}$ ranged from 5 to 100 measurement positions on the rocking curve. A total photon count value of 10,000 was chosen to simulate a low dose situation were there are not many

87

photons available to form the image, as these are the most difficult cases. In figure 8.19 the relative errors of the Gaussian fit parameters are shown versus the number of measurement locations on the rocking curve. The errors shown in the plots were calculated using the formula,

$$\text{Error} = \frac{\text{True Value} - \text{Fit Value}}{\text{True Value}} \times 100\%$$

with the exception of the peak center since the true value is zero. For the peak center parameter the fit value was compared against the width of the Gaussian.
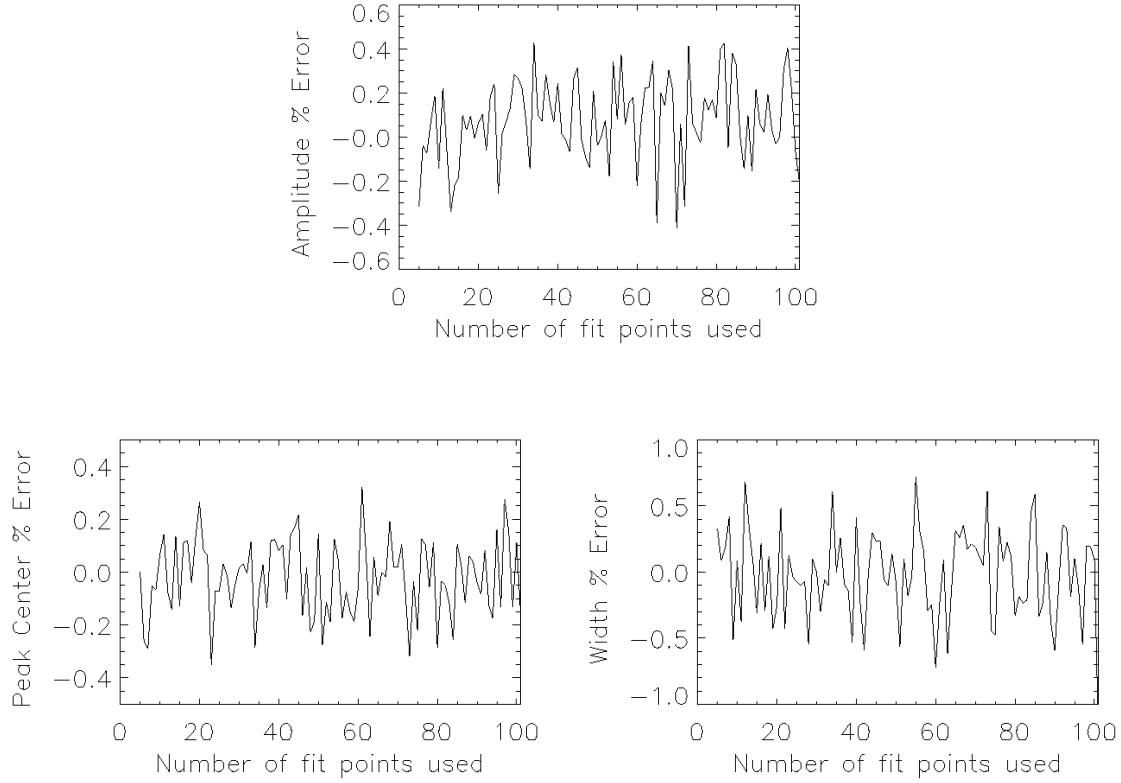


Figure 8.20: The percent error in the Gaussian amplitude, peak center, and width values compared with the true values averaged over 100 simulations.

All three error plots showed variations in the amount of error depending on the

number of measured points used. To determine if this result was real or a random occurrence the same simulation was run 100 times and the errors averaged (See figure 8.20). The errors were significantly reduced for all fitting parameters regardless of how many measurement points were used indicating that there is no benefit or penalty to image reconstruction for using more or fewer rocking curve positions.
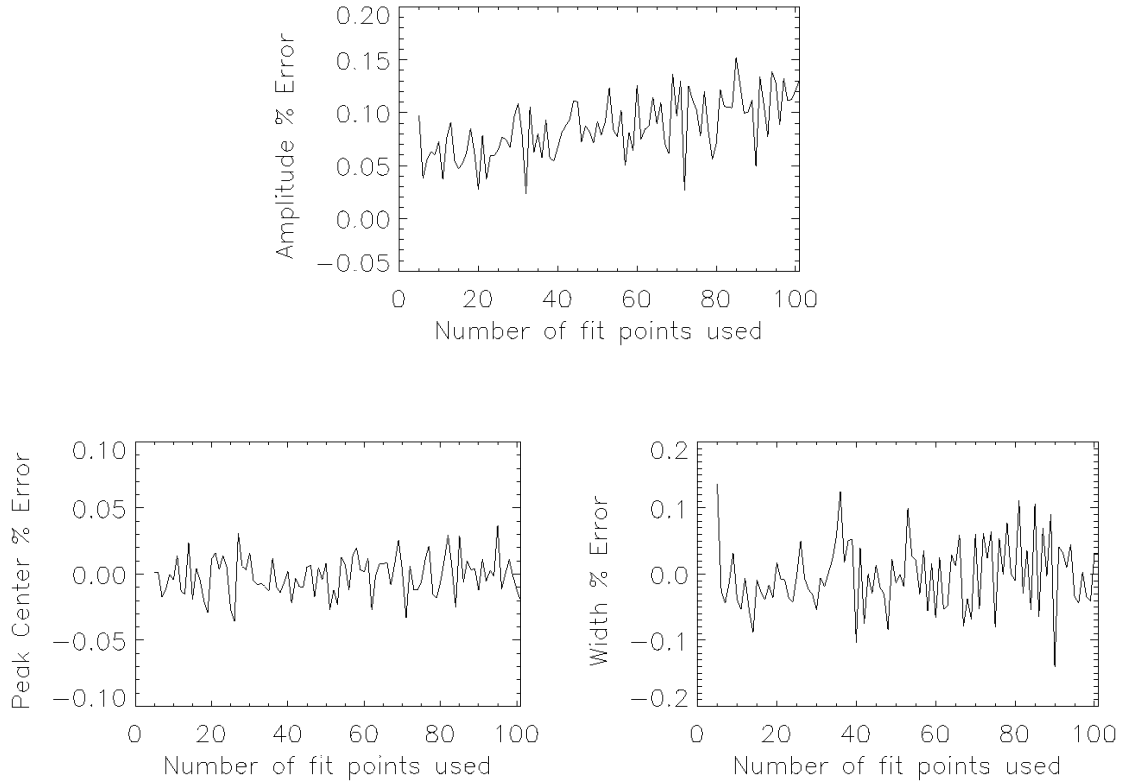


Figure 8.21: The percent error in the Gaussian amplitude, peak center, and width values compared with the true values averaged over 10,000 simulations.

To further confirm that the fitting error did not depend on the number of points measured on the rocking curve a simulation was run which averaged 10,000 fits (see figure 8.21). The amplitude parameter did show a trend where the fitting value is over estimating the true amplitude of the Gaussian by a small amount. The width and peak center values were centered around zero error indicating that regardless

89

how many points were used on average the true value would be returned. Thus for five or more points (five being the minimum number of points needed for the IDL four variable fitting routine) the Gaussian fit of the rocking curve would be equally good for all cases for the same number of photon counts or dose.

### 8.3.3   Using the XRP to measure absorption and extinction

The following measurements were taken using a DCM Si(4,4,0) pencil beam (1.0mm X 1.0mm) at 40.4keV, a 15cm plate length ion chamber, the XRP, a Laue Si(4,4,0) analyzer crystal, and a NaI scintillation detector. Using this new apparatus configuration the absorption and scatter of three types of materials were measured (see Figure 8.22). X-rays traversed the target material and then passed through the XRP, which was rotated from 79 degrees to 89 degrees. The amplitude and width of the crystal rocking curve was measured by recording the photon count at each XRP angle. The resulting refraction deviation angle range was 8.51$\mu$radians, which is equivalent to 4.13 times the FWHM of the Si(4,4,0) DCM at 40.4keV. This range of angles is wider than the previous measurements to account for peak broadening of the rocking curve by passing through the sample materials. As with the previous set of measurements harmonics are ignored, as the lower harmonic is removed by attenuation and the next higher order harmonic has ten times less intensity.

The absorption and scattering (peak broadening) was measured for 1mm of aluminum, 1/80 inches (0.32mm) of copper, and 10 sheets (1.02mm) of paper, and a measurement with no target for comparison. The measured data was XRP angular position with photon counts and what is needed is the refraction deviation angle versus photon count. To determine the refraction deviation the tangent of the XRP angle is taken in product with the real part of the refractive index correction for
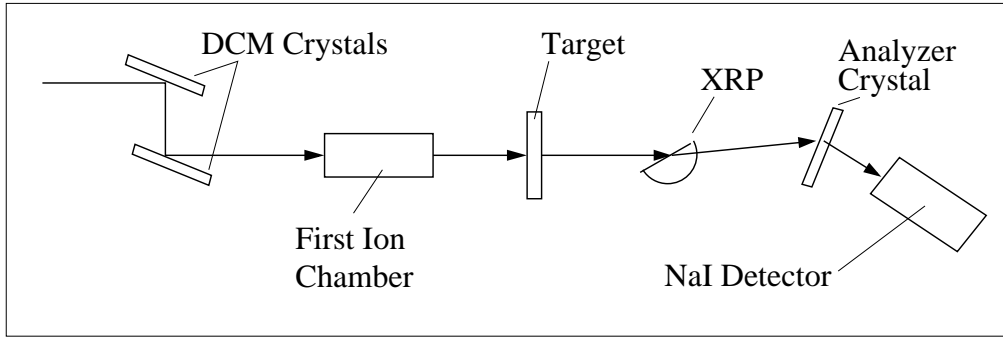
Figure 8.22: Apparatus outline for the absorption and scatter measurements.
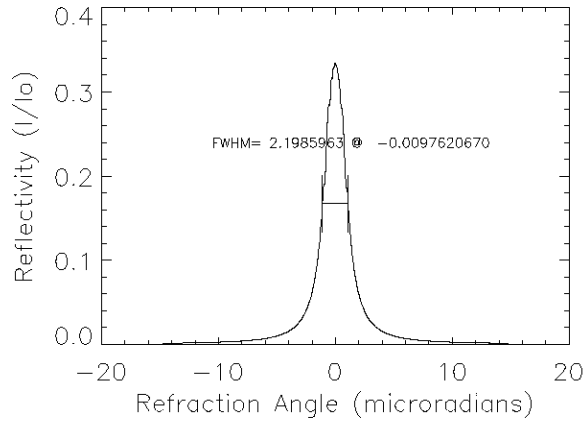


Figure 8.23: The predicted rocking curve for a Bragg Si(4,4,0) DCM and a Laue Si(4,4,0) analyzer [Jam62, Zac45].

PMMA for each XRP position. Using the calculated refraction deviation angle and the photon count data the amplitudes, peak centers, and standard deviations were calculated by a Gaussian fit using IDL (ITT, Boulder, CO, USA) (See Figure 8.24). For each target four measurements were taken and averaged. After accounting for the gain and filter changes made to keep the counting rate for each sample similar the amplitude and width of the measured curves are presented in Table 8.2.

The measured width of the Si(4,4,0) rocking curve was $2.31\mu$radians (See Table 8.2) and is close to the theoretical value of $2.2\mu$radians (See Figure 8.23). Causes of the
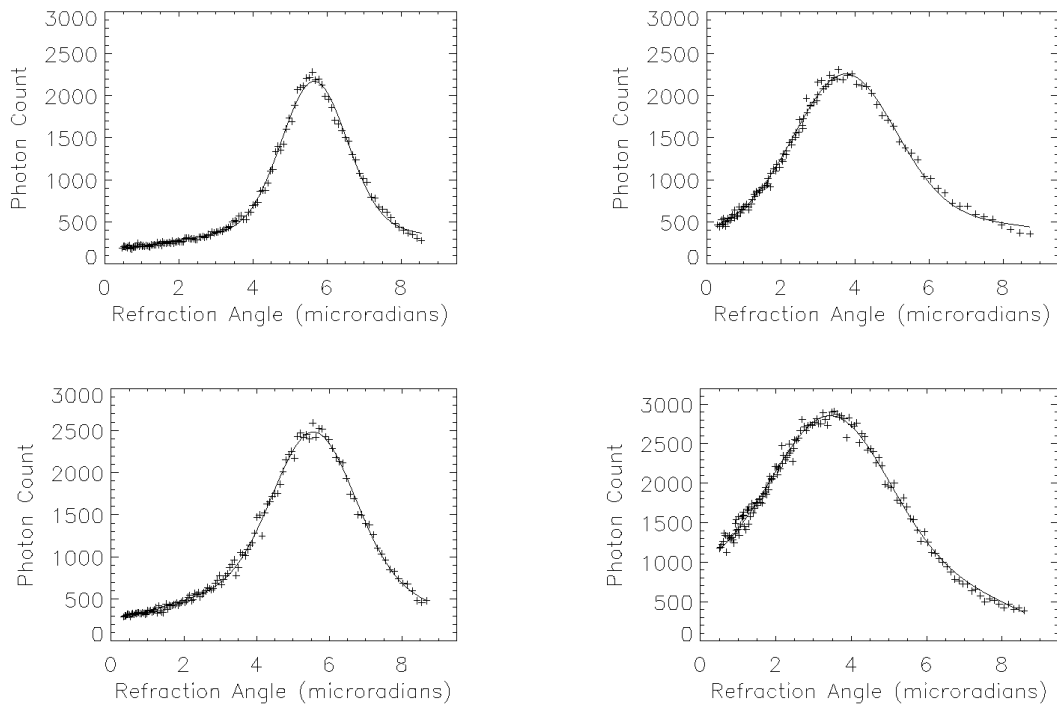
Figure 8.24: Measured rocking curves during the material tests. Top Left: No target, Top Right: 1.0mm of Paper, Bottom Left: 1.0mm of Aluminum, Bottom Right: 0.32mm of Copper

difference in values include broadening due to the path through the XRP, crystal alignment error from the crystals not oriented perfectly parallel, and broadening due to beamline filters, ion chambers, and the air path in the experimental hutch. To ensure the remaining values for each material are reasonable the integral of each Gaussian curve was be calculated to determine the absorption. This assumes that any photon that is not stopped in the material by absorption is either slightly refracted in angle or undergoes USAXS and is countable by the detector if a wide enough angle range is measured. Hence if the objects did not absorb at all and only refraction and USAXS occurred the total number of counts would be the same for every sample, but there would be variations where the photons were scattered and refracted to in

| Target material | Peak Amplitude (arbitrary units) | FWHM ($\mu$radians) | Standard Deviation of FWHM ($\mu$radians) |
|---|---|---|---|
| None | 1745 | 2.31 | 0.16 |
| 1mm Al | 1319 | 2.94 | 0.12 |
| 0.32mm Cu | 388 | 4.16 | 0.18 |
| 1mm of Paper | 1395 | 3.57 | 0.28 |

Table 8.2: Averaged values for the amplitude, full width at half maximum, and standard deviation of the FWHM for each material.

angle.

$$A = \int\limits_{-\infty}^{+\infty} r(\theta)d\theta \approx \sum_{i=1}^{n} r(\theta_i)\Delta\theta_i$$

where A is the integrated photon intensity, $r(\theta)$ is the measured intensity at rocking curve angle $\theta$, and $r(\theta_i)$ is the photon count for the $i^{th}$ discrete position in angle on the rocking curve with $\Delta\theta_i$ angle separation between measurements.

To include the attenuation effects for each sample the calculated area A was multiplied by a correction factor equal to $C_i = 1/N_o \exp(-\mu_i t_i)$ to account for attenuation in the material, where $C_i$ is the correction factor for the $i^{th}$ material, $N_o$ is the incident number of photons, $\mu_i$ is the attenuation coefficient for material i, and $t_i$ is the thickness of the $i^{th}$ material. With absorption effects removed the different widths of the curves must account for all photons that were not absorbed. Thus the integrated area of each curve should be similar for every sample.

The results of calculating the area under the curve for each material using a Gaussian fit is shown in Table 8.3, using the equation

$$A_i = C_i \int\limits_{-\infty}^{+\infty} \frac{N_{amp}}{\sqrt{2\pi}\sigma} \cdot \exp\left(\frac{-(\theta - \theta_o)^2}{2\sigma^2}\right) d\theta \bigg|_{\theta_o=0} \tag{8.3}$$

| Material | Curve Area ($A_i$) | Correction factor ($C_i$) |
|----------|--------------------|---------------------------|
| None | 4.3 | 1.0 |
| 1mm Al | 4.4 | 0.86 |
| 0.32mm Cu | 4.9 | 0.27 |
| 1mm of paper | 4.5 | 0.98 |

Table 8.3: List of the calculated curve areas for each material's Gaussian fit integrated from negative infinity to infinity using equation 8.3, parameters from table 8.2, and the $C_i$ value from the correction factor column.

where $N_{amp}$ and $\sigma$ are the amplitude and width parameters determined from Table 8.2, and $C_i$ are the absorption correction factors for each material listed in Table 8.3. The factor for no target is 1.0 as there is no correction necessary. The remaining materials have absorption loss through the material: 1) the aluminum target transmission is 0.86; 2) the copper target transmission 0.27; and 3) for paper the correction factor was approximated by calculating the absorption through cellulose $C_6H_{10}O_5$ at 40.4keV giving a transmission value of 0.98.
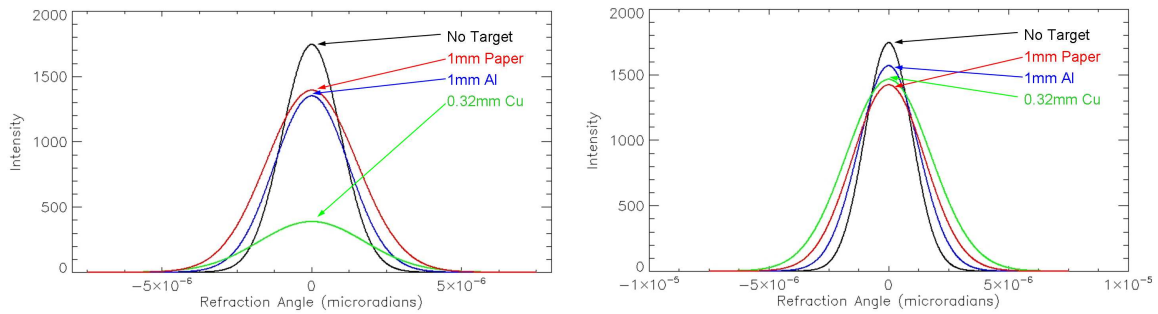


Figure 8.25: Left: Measured material curves. Right: Material curves after absorption adjustment.

The calculated areas under the Gaussian curve for each material are similar, but not the same. The differences in values are due to thickness variations of the material, impurities in the material, and scattering of photons outside the measurable angle

range. However, the results do confirm the potential to measure differences in absorption and scatter by scanning through the DCM rocking curve using an X-ray prism [Bew10].

## 8.4   XRP Discussion

The advantage of the XRP based system over the previous crystal motion based system is the ability to quickly sweep through the rocking curve, and the increase in the number of data points on the rocking curve when the XRP is scanned. Traditional analyzer based imaging methods use only a few angle positions on the rocking curve and long dwell times at each angle. Because of this the traditional DEI or MIR systems are more susceptible to motion artifacts as all the points on the rocking curve are acquired during separate scans. This means that measuring additional angular positions on the rocking curve to better determine changes from adding an object invites more chances for motion artifacts with every additional scan. Figure 8.26 diagrams the situation in traditional crystal motion based systems. In the case of DEI only positions $\theta_{1,2}$ are measured and the changes from adding an object are approximated from these two points using equations 4.10 and 4.11. In DEI there is no information on USAXS because by using the two data points shown in figure 8.26 any broadening of the curve would be indistinguishable from absorption effects. In MIR where the minimum data set is three points, $\theta_{1,2,3}$, figure 8.26 again shows how little information is used to define the rocking curve. However, MIR does give estimates on absorption, refraction angle deviation, and USAXS using equations 4.12 - 4.14.
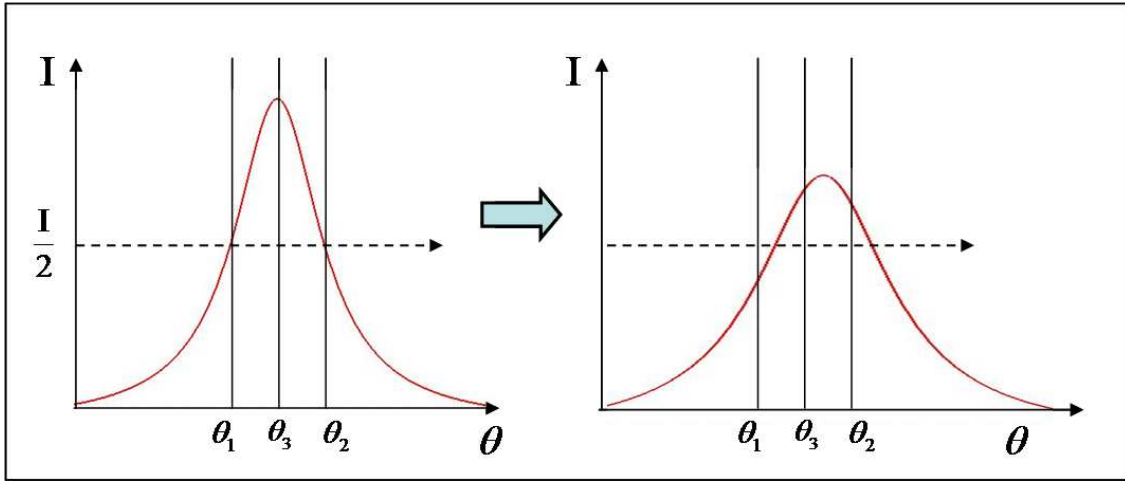
Figure 8.26: The current DEI and MIR techniques take limited data points ($\theta_{1,2}$ for DEI and $\theta_{1,2,3}$ for MIR) on the rocking curve and approximate what changes to the curve occured when an object was placed in the path.

The XRP improvement makes it possible to measure many positions along the rocking curve quickly. The majority of the measured points are always on one side of the curve as the tangent dependence with angle gives a non-uniform distribution of positions on the rocking curve. The advantage of measuring additional points using the XRP is that a Gaussian fit of the rocking curve is possible which returns amplitude, peak center, and variance. These are the very quantities that are approximated in the MIR technique: 1) absorption, $I_R$ in equation 4.12; 2) refraction angle deviation, $\Delta_{\theta_R}$ in equation 4.13; and 3) USAXS, $\sigma^2_{\Delta_S}$ in equation 4.14, but now come from a more detailed sampling of the rocking curve close together in time at the expense of high counting statistics for each point. This satisfies one of the project goals by improving the DEI/ABI/MIR techniques by removing some of the sensitivity to object motion, and by offering a better approximation of the rocking curve than the two or three point techniques. The rapid scanning of the rocking curve gives the XRP technique of analyzer based imaging great potential in the area of biological imaging.

Other project goals satisfied are the size and weight reduction from the tangent arm system to the XRP. Another project goal was that the current angular resolution would not be sacrificed by XRP design. The direct mechanical control of the original apparatus had a $0.1\mu$radian angle minimum step size, which was set by tangent arm servo motor's minimum step size of $0.1\mu$m. The XRP has a minimum angle step size of $\frac{360^{\circ}}{66\cdot200\cdot256} = 0.1065 \times 10^{-3}$ degrees (66 motor turns per full revolution of the stage, 200 steps per motor revolution, 256 micro-steps per full step). At the maximum designed angle of 88.5 degrees the angle deviation is $6.07166\mu$radians (see section 8.1.4) one step back would change the angular alignment to $0.159 \times 10^{-6} \cdot \tan(88.5 - 0.1065 \times 10^{-3})) = 6.07123\mu$radians. The difference between angle deviations is $4.3 \times 10^{-10}$radians and sets the lowest angle positioning resolution in the operational range. Additional steps away from the high angle limit of operation will have increasingly finer step sizes. This increase in position sensitivity satisfies the project goals for the XRP. The only remaining project goal is to test the XRP in a combined imaging system and is discussed in the next chapter.

# Chapter 9

# Testing of a Combined Diffraction Enhanced Imaging and Fluorescence Imaging System

Once the XRP was proven to effectively align an x-ray beam by using the adjustable refraction angle deviation it was incorporated into a bench-top system that could be inserted and withdrawn easily from the BMIT bending magnet beamline. This meant that a new analyzer crystal and detector would be needed to replace the large tangent arm crystal system and ion chamber used previously.

## 9.1 Laue Analyzer

A pair of Laue diffraction 1cm x 2cm strain relief cut crystals with thickness of 0.10cm were chosen. The crystals were mounted to aluminum plates with a tapped bolt pattern to couple with a Thorlabs rotation stage. Care was required to ensure

that the crystal was at the center of rotation when mounted (See Figure 9.1). This involved careful alignment of the base plate, mounting post, and crystal.
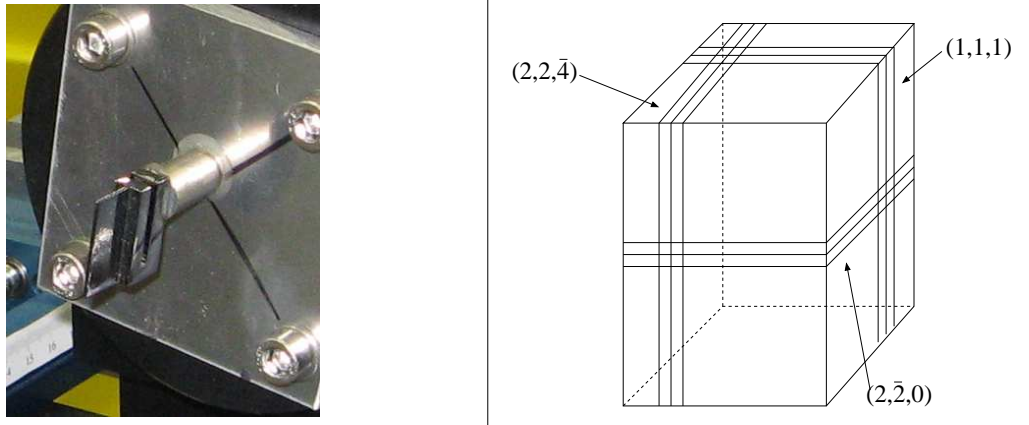


Figure 9.1: Left: The Laue analyzer crystal epoxied to a post and mounted to a rotation stage. Right: The orientation of the lattice planes in the analyzer crystal.

It was necessary to confirm the orientation of the diffraction planes in the Laue analyzer as they needed to be compatible with both the BMIT Si(1,1,1) DCM and the replacement Si(2,2,0) DCM crystal sets. Transmission Laue images were acquired of the crystal using the BMIT bending magnet beamline to prepare a monochromatic beam of x-rays and a fluorescence screen with video camera setup to record the diffraction pattern.
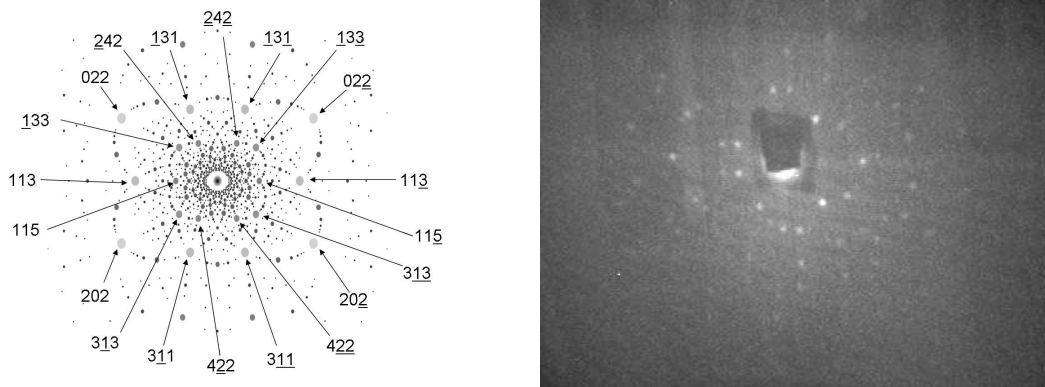


Figure 9.2: Left: The predicted transmission Laue diffraction pattern from a Silicon $(2, \bar{2}, 0), (1, 1, 1), (2, 2, \bar{4})$ oriented crystal. Right: The observed diffraction pattern from the crystal, which agreed with the prediction.

There was agreement in the observed diffraction pattern with the predicted pattern

99

for a transmission Laue image of a crystal having $(2, \bar{2}, 0), (1, 1, 1), (2, 2, \bar{4})$ oriented lattice planes (See Figure 9.2). When the BMIT DCM crystal set was switched all that was required to keep the Laue analyzer properly oriented was to rotate it by 90 degrees going from the Si(1,1,1) to the Si(2,$\bar{2}$,0) lattice planes.

## 9.2 Matching the measured and predicted rocking curves

Before the combined DEI and FI system was used the rocking curve was measured and compared with the theoretical prediction from dynamical diffraction theory, which is appropriate for the perfect crystals used in the BMIT DCM and for the analyzer [Bat64, Jam62, Zac45]. The rocking curve was acquired by slowly scanning the Laue analyzer crystals Bragg angle while the DCM was tuned and measuring the diffracted beam using a NaI detector. The measured curve was then scaled to the same reflectivity amplitude as the theoretical curve so that the widths could be compared (See figure 9.3).
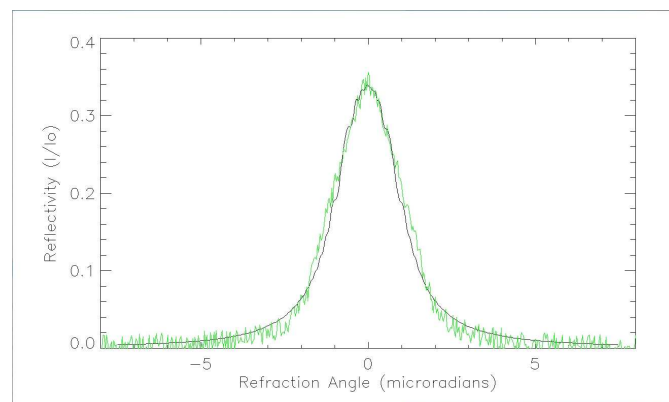


Figure 9.3: Plot of the measured rocking curve (green line) and the theoretically predicted rocking curve (black line).

For a Si(4,4,0) double crystal Bragg diffraction monochromator convoluted with a Laue Si(4,4,0) diffraction analyzer at 40.4keV theory predicted a FWHM of 2.20 $\mu$radians and the measured value was 2.31$\mu$radians. The slopes of the measured and predicted curves need to match because they will be used to calculate the DEI images using equations 4.8 and 4.9. To broaden the predicted curve slightly so the width would also be 2.31$\mu$radians the energy of the theoretical curve was lowered to 40.05keV causing the necessary broadening. Once a calculated curve matched the measured curve the amplitude and width of any DEI detune setting could be determined using numerical approximations. For instance when images were acquired half way down from the top of the rocking curve the reflectivity is taken to be one half the calculated maximum reflectivity and the slope is determined by using the central difference formula (equation 9.1) at this point,

$$f(\theta_{i+1}) = f(\theta + h) = f(\theta) + f'(\theta)h + \frac{f''(\theta)h^2}{2!} + \frac{f'''(\theta)h^3}{3!} + ...$$
$$f(\theta_{i-1}) = f(\theta - h) = f(\theta) - f'(\theta)h + \frac{f''(\theta)h^2}{2!} - \frac{f'''(\theta)h^3}{3!} + ...$$
$$\Rightarrow f(\theta + h) - f(\theta - h) = 2f'(\theta)h + 2\frac{f'''(\theta)h^3}{3!} + ...$$
$$\Rightarrow f'(\theta) \simeq \frac{f(\theta+h)-f(\theta-h)}{2h} \tag{9.1}$$

where $\theta$ is the angular alignment and h is the increment between measurements. By using a 2000 point array representation of the calculated curve the error in the numerical derivative and reflectivity amplitude was less than one percent.

## 9.3   Flux Calculations

Before beginning measurements the photon flux available using the two reflections and energies of interest were calculated. These predicted flux intensities would then

be compared to the measured value from an ion chamber using the process detailed in section 3.2 to determine if the beamline was operating properly.

### 9.3.1 Si(2,2,0) at 20.2keV

For the BMIT bending magnet beamline the predicted photon flux is calculated using equation 3.1 with E=2.9, I=0.001, and y=20.2/7.5=2.69 gives $7.13\times10^{10}$ $\left[\frac{\text{Photons}}{\text{s}\cdot\text{mr}^2\cdot0.1\%\text{bandwidth}\cdot\text{mA}}\right]$. The beam spot size is 1mm x 1mm and is at the middle of the second table in the second primary optical enclosure (POE2), which is 26.1m from the source of x-rays. The angular size is then $(0.0383\text{mr})^2 = 0.00147\text{mr}^2$. The bandwidth from the unstrained Si(2,2,0) crystal reflection at 20.2keV is 0.0566·0.1%bandwidth. The maximum flux available in a 1mm x 1mm beam spot when 250mA is in the storage ring is $7.13\times10^{10}$ $\left[\frac{\text{Photons}}{\text{s}\cdot\text{mr}^2\cdot0.1\%\text{bandwidth}\cdot\text{mA}}\right]$ $\times 0.00147\text{mr}^2 \times 0.0566 \cdot 0.1\%\text{bandwidth} \times 250\text{mA} =$ $1.48 \times 10^9 \frac{\text{Photons}}{\text{s}}$.

### 9.3.2 Si(4,4,0) at 40.4keV

For the BMIT bending magnet beamline the predicted photon flux is calculated using equation 3.1 with E=2.9, I=0.001, and y=40.4/7.5=5.39 gives $9.19\times10^9$ $\left[\frac{\text{Photons}}{\text{s}\cdot\text{mr}^2\cdot0.1\%\text{bandwidth}\cdot\text{mA}}\right]$. As before the beam spot size is 1mm x 1mm and is at the middle of the second table in POE2 giving an angular size of $(0.0383\text{mr})^2 = 0.00147\text{mr}^2$. The bandwidth from the unstrained Si(4,4,0) crystal reflection at 40.4keV is 0.00911. The maximum flux available in a 1mm x 1mm beam spot when 250mA is in the storage ring is $9.19\times10^9$ $\left[\frac{\text{Photons}}{\text{s}\cdot\text{mr}^2\cdot0.1\%\text{bandwidth}\cdot\text{mA}}\right]$ $\times 0.00147\text{mr}^2 \times 0.00911 \cdot 0.1\%\text{bandwidth} \times 250\text{mA} =$ $3.07 \times 10^7 \frac{\text{Photons}}{\text{s}}$.

### 9.3.3 Beam Filtering

For the DEI measurements the 40.4keV harmonic is needed. Due to the difference in incident photon flux between the fundamental and the first harmonic, filters must be used to attenuate the fundamental by several orders of magnitude so that the first harmonic is dominant in the remaining photon beam. This was achieved by a 0.32mm copper filter. Table 9.1 shows a list of aluminum and copper filters and how they affect the photon beam.

| Filter | 20.2keV | 40.4keV |
|--------|---------|---------|
| 2mm Al | 0.166 | 0.741 |
| 3mm Al | 0.068 | 0.638 |
| 0.16mm Cu | 0.009 | 0.512 |
| 0.32mm Cu | 0.0001 | 0.2626 |

Table 9.1: Calculated X-ray transmission through various aluminum and copper filters at 20.2keV and 40.4keV.

## 9.4 Description of the combined imaging system

The experimental apparatus for the combined DEI and FI system is illustrated in figure 9.4. The incident beam or $I_o$ was measured by an IC Plus 15cm ion chamber (Oxford-Danfysik, Oxford, UK) filled with air. The current of the ion chamber was measured by a model SR570 electrometer (Stanford Research Systems, Sunnyvale, CA, USA) and was converted to a frequency using a VTF converter NIM module (NOVA, Riverside, CA, USA). The beam was vertically collimated to 1mm tall entering the ion chamber using tungsten carbide blocks, and horizontally collimated exiting the ion chamber to 1mm wide.
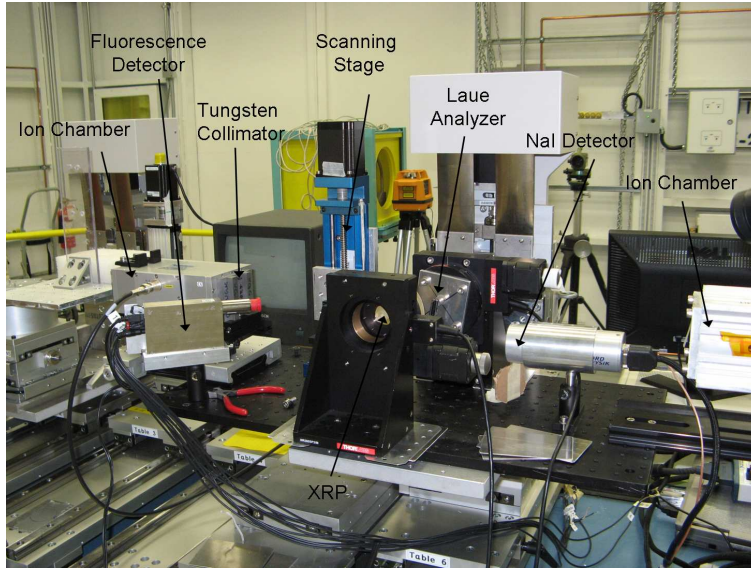
Figure 9.4: The prototype DEI and FI imaging system.

The fluorescence spectrometer used was an X-123 Si detector with 25mm$^2$ detection area (AmpTek, Bedford, MA, USA), 500$\mu$m thick, and covered by a 25$\mu$m beryllium window. The onboard single channel analyzers (SCA) were used to define windows for Mn, Fe, and Compton scattering events using ranges of bin numbers. Raster scanning the sample in the horizontal (inboard-outboard) and vertical (up-down) directions was accomplished using two 20mm travel 1/8inch lead screw pitch stages with NEMA 23 (Parker, Parker Motion Catalogue, Chicago, IL) two phase stepper motors and MID-7604 24V micro-stepping drivers (National Instruments, Austin, TX, USA). The MID-7604 driver was operated at a micro-stepping setting of 50 micro steps per full step for smooth motion and a 1A drive current setting to ensure the stages would not stall. The positioning accuracy of the sample in both directions was $\frac{3.175\text{mm/rev}}{200\text{step/rev}\cdot50\mu\text{step/step}} = 0.3175\mu$m. The XRP and the Laue analyzer crystal were driven by Thorlabs NanoRotator stages using the MID-7604 driver at a 256 micro-steps per full step setting with 1A drive current. This gave the maximum possible angular resolution of the NanoRotator/MID-7604 system at

$$\frac{\frac{360^{\circ}}{66\text{rev}}}{200\text{step/rev} \cdot 256\mu\text{step/step}} = 0.107 \times 10^{-3}\text{degrees} = 1.86\mu\text{radians}.$$ The diffracted beam from the analyzer crystal was measured using an 3cm diameter NaI scintillation detector (Oxford-Danfysik, Oxford, UK). Signal pulse processing from the NaI detector was handled by a Cyberstar x2000 NIM module (Oxford-Danfysik, Oxford, UK). The pulse counting for the ion chamber and NaI detector was recorded by the National Instruments LabVIEW DAQ. In addition to acting as a multi-channel scalar using PXI-6602 counter timer cards, the DAQ also contained PXI-7350 motion controller cards to coordinate the motion of all translation and rotation axes.
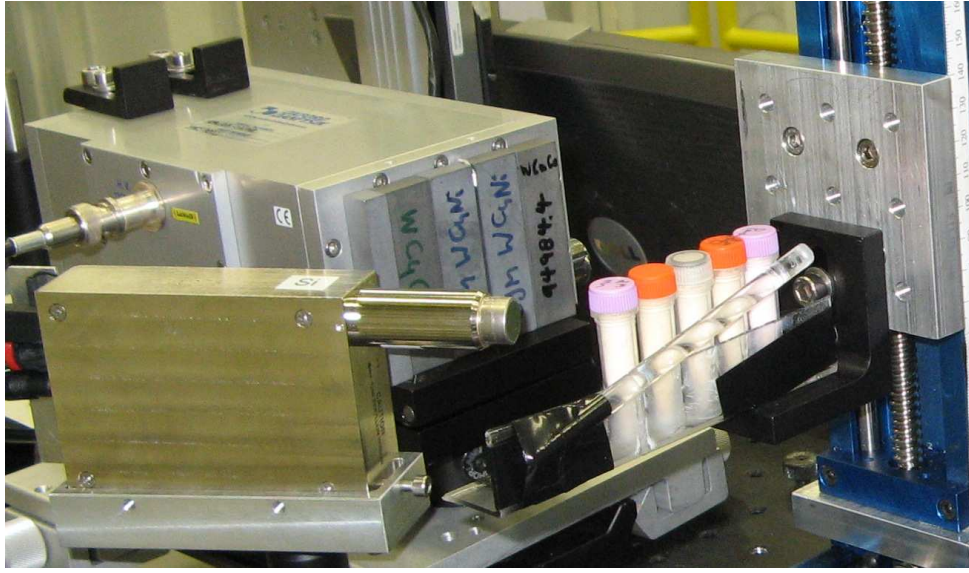


Figure 9.5: Image of the phantom sample containing cuvette sample holders and the acrylic rod.

The phantom sample with three cuvettes is shown in figure 9.6. The left cuvette contained $MnCl_2 \cdot 4H_2O$ powder, the middle cuvette $Fe_2(SO_4)_3 \cdot H_2O$ powder, and right cuvette contained gelatin powder, which should not contribute to either the Mn or Fe image. There was no dilutions of any of the powders, but each was used in its pure form. The region of the phantom raster scanned during the fluorescence

105

and DEI imaging is highlighted by a white box in figure 9.6 and an absorption and refraction angle image of the phantom are given for later comparison in figure 9.7.
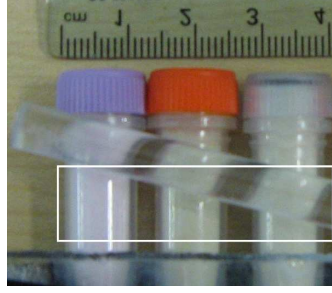


Figure 9.6: Image of the measured phantom sample with a ruler showing a 1cm scale. The box in white shows the region measured by the fluorescence raster scan.
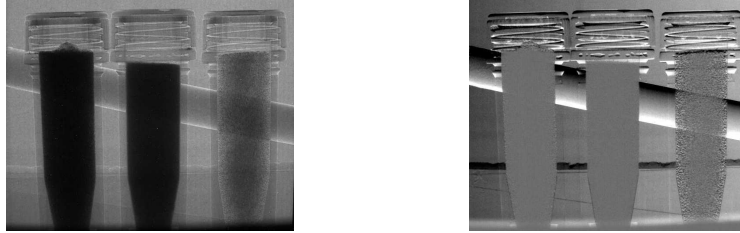


Figure 9.7: Images taken using an VHR-90 area detector for comparison with the raster scan images. Left: Absorption image. Right: Refraction angle image.

## 9.5   Analysis and results

The FI and DEI scans were done separately and results will be presented individually in the next two subsections. The scans were done separately so that a slower 20.2 keV scan using the Si(2,2,0) reflection could be used for the FI imaging and a faster 40.4keV scan using the Si(4,4,0) reflection could be used for the DEI imaging. The slower scan and lower energy were necessary for the FI imaging as: 1) the geometry of the sample and the Si detector probe size required the detector to be placed in a back scatter position 50mm from the sample and at 153 degrees from the incident direction giving $\sim$0.1% coverage of $4\pi$Sr; 2) using a lower energy would result in

higher absorption of the beam and hence increased fluorescence, which helped offset the loss of usable signal due to the overlap of the $K_{\alpha 1}$ of Fe and the $K_{\beta 1}$ of Mn; and 3) the slower scan speed and energy both helped compensate for the 84% absorption loss of fluorescence from Mn and Fe due to the 1mm thick plastic cuvette wall. The plastic cuvette used was necessary due to the degradation over the many months of testing of previous samples that were prepared in gelatin and sealed with tape. Pure powder samples were used to help increase signal and decrease scan time, but only the surface layer of the sample would contribute to the signal as fluorescence from beneath the surface would be quickly attenuated within $100\mu$m. For the DEI imaging the higher order reflection of the Si(4,4,0) was necessary for image quality. This is because the resolution was set by the beam spot size (which was 1mm) so edge features in the image would be only a fraction of the total pixel, thus the change in counts from the small edge would need to be significant to affect the total pixel average.

## 9.5.1 Fluorescence Imaging

Before fluorescence imaging using the Si detector could commence the SCA windows for Mn, Fe, Compton, and Coherent scatter were set. The gain of the detector was chosen to use as much of the 1024 bin range as possible without moving any of the peaks of interest off scale. Spectra were then acquired for each of the three cuvettes that were to be imaged, which contained $MnCl_2 \cdot 4H_2O$, $Fe_2(SO_4)_3 \cdot H_2O$, and gelatin (See figures 9.8-9.10). These spectra were then plotted together to determine if the detector energy calibration was consistent, and what bin windows could be used for the SCA settings.
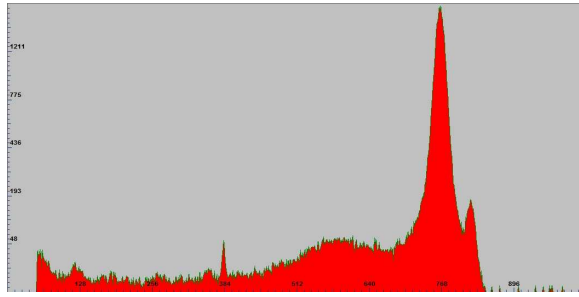
Figure 9.8: Spectrum from the control cuvette with gelatin.
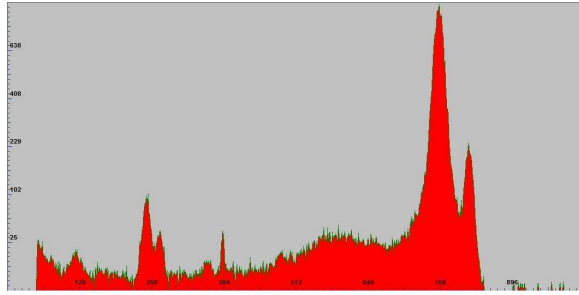


Figure 9.9: Spectrum from the cuvette containing $MnCl_2 \cdot 4H_2O$.
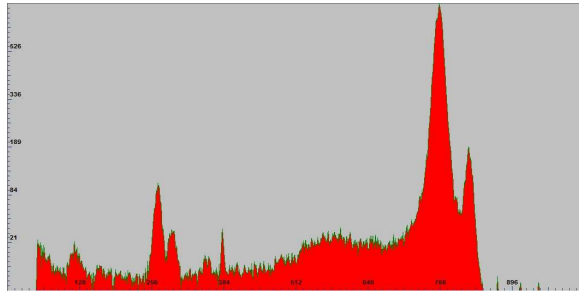


Figure 9.10: Spectrum from the cuvette containing $Fe_2(SO_4)_3 \cdot H_2O$.

The SCA windows for manganese and iron were constrained by the overlap in peaks between the $K_{\beta 1}$ of manganese at 6,490eV and the $K_{\alpha 1,2}$ of iron at 6,403eV and 6,390eV respectively. In the region of overlap the elemental identity is ambiguous and was ignored by the system. During the fluorescence scans SCA 1 was windowed around the $K_{\alpha 1,2}$ peaks of manganese, SCA 2 was windowed around the $K_{\beta 1}$ peak of iron, and SCA 3 was windowed around the Compton and Coherent scatter (See figure 9.11). The scatter window was implemented so as to provide a reference image to determine the alignment of cuvettes in the scan.
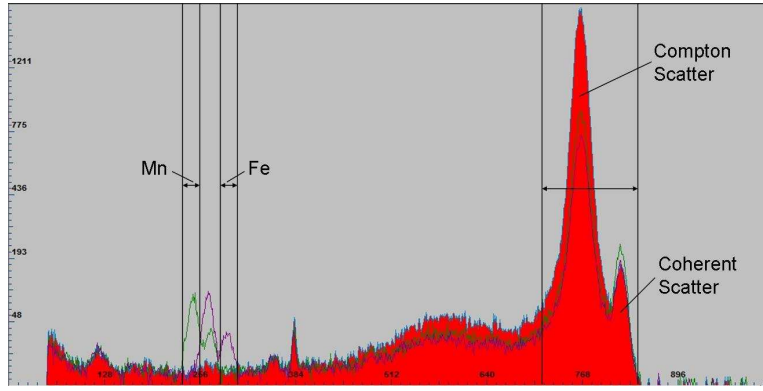
Figure 9.11: Overlay of Mn, Fe, and gelatin control spectrum.

The typical scan time for a fluorescence image was several hours compared to the 16 minute scan time of the DEI portion of the system. Due to the length of the scan time there was typically significant drift due to electron current decay in the synchrotron storage ring. Using the $I_o$ value the counts from the Si detector ($N_{Si}^i$) were corrected for the storage ring decay by multiplying by the ratio of the storage ring current value at the beginning of the scan ($I_{max}^i$) with the ring current at the time of measurement ($I_o^i$),

$$\text{Intensity Corrected Counts } = \frac{I_o^{max}}{I_o^i} \times N_{Si}^i.$$

**Fluorescence system test**

The first set of fluorescence raster scans tested the motion control, alignment, SCA windows, and multichannel scalars of the system. The images from scans 8 and 9 are shown in figures 9.12 and 9.13 respectively. The scattering images for both scans showed that the cuvettes were too low in the imaging area as the tops of the cuvettes could be seen. The consequence of this height misalignment was that the Mn and Fe images showed only a portion of the cuvette depending on the level to which the

cuvette was filled.
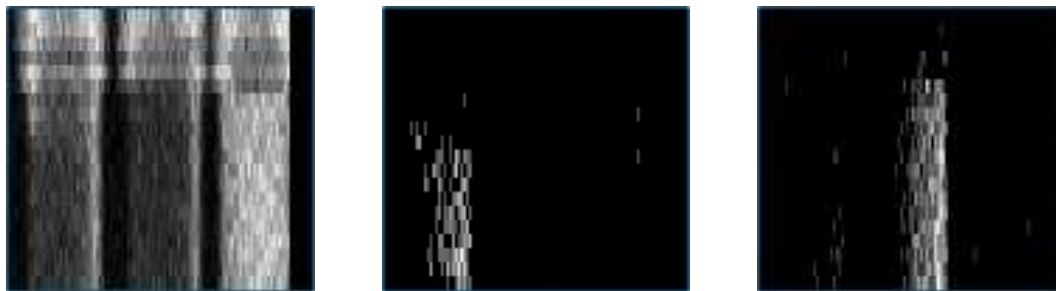


Figure 9.12: From left to right: the scatter image, the Mn image, and the Fe image for scan 08
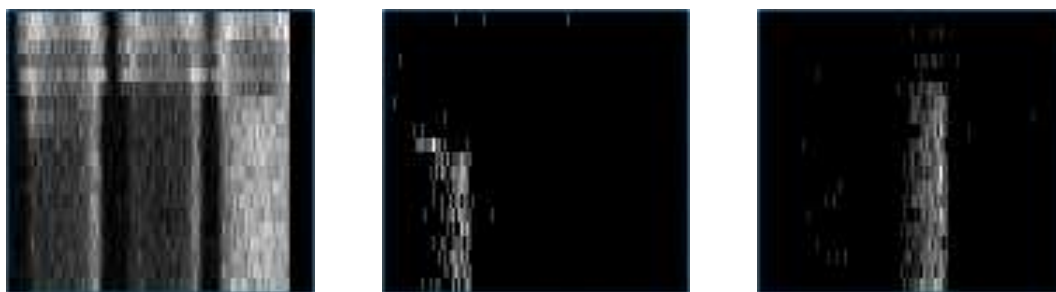


Figure 9.13: From left to right: the scatter image, the Mn image, and the Fe image for scan 09

The absence of motion artifacts in all three images indicated that the motion control and multichannel scalars of the DAQ were functioning properly. The images also indicated that the SCA windows for Mn and Fe were functioning well as only trace amounts of the elements were misidentified at the location of the other sample cuvette or throughout the image. Due to the relatively low signal in the images at the location of the powder sample the SCA windows were widened slightly so fewer counts would be rejected. Before the next set of measurement the necessary adjustments to positioning were made and an acrylic rod was added as a refraction phantom for the DEI measurements acquired between FI scans.

**Fluorescence scans 17 and 29**

In figure 9.14 the images for scan 17 are shown. The acrylic rod added to the phantom sample is clearly visible in the scatter image, but is not present in the Mn or Fe images as expected. The concentrations of Mn and Fe coincide with the cuvettes and have few element misidentifications. In the Mn image there is a trace amount of misidentified manganese over the iron cuvette due to the SCA window allowing part of the $K_{\alpha 1,2}$ fluorescence peaks to be counted. No such misidentifications are visible in the Fe image as the increased energy separation between the $K_{\beta 1}$ of Mn and the $K_{\beta 1}$ of Fe allowed for more stringent windowing without rejecting an unreasonable amount of signal.
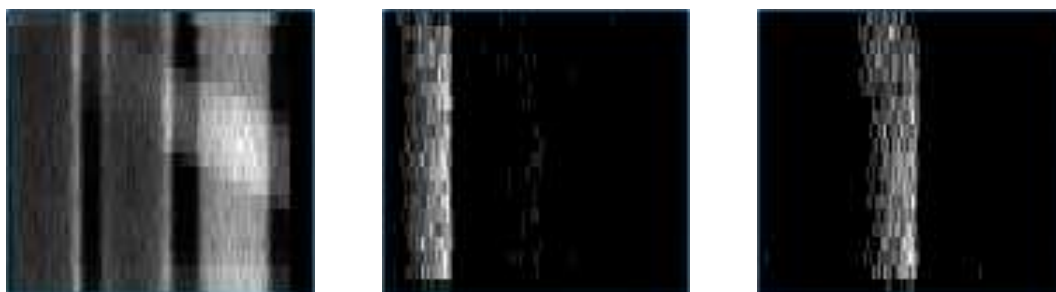


Figure 9.14: From left to right: the scatter image, the Mn image, and the Fe image for scan 17

The alignment of scan 17 is an improvement from the previous attempts and the entire vertical field of view is filled with signal from the powder in the cuvettes. By raising the cuvettes up in the field of view the sample holder appeared in the scatter image as a bright band at the bottom of the image.

The last successful fluorescence scan was 29 and was very similar in appearance to scan 17 discussed above. The only substantive difference was at the end of this measurement when an error in the multi-channel scalar buffering led to the loss of data

and appears as a dark region in the bottom right hand corner of the scatter image. Additional scans were attempted, but did not reach completion due to storage ring dumps.
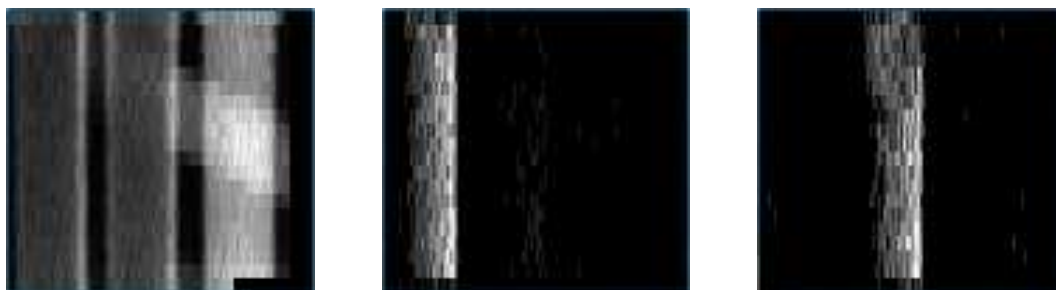


Figure 9.15: From left to right: the scatter image, the Mn image, and the Fe image for scan 29

**Summary**

The fluorescence imaging portion of the system performed satisfactorily mapping the areas where the two elements of interest were present. The challenging task of distinguishing between the emission lines of Mn and Fe led to a small amount of element misidentification in the Mn image. Due to the $\sim0.1\%$ coverage of $4\pi$ Sr and the 84-85% absorption loss of fluorescence in the cuvette wall the SCA windowing could not be too restrictive without filtering out large portions of the available signal. The original objective of making the XRP version of a DEI system compatible with other imaging methods was met with this system. Discussion of possible improvements are presented in the final chapter.

## 9.5.2 Diffraction Enhanced Imaging

For the following images the data was acquired with the XRP at a fixed angle which was chosen to cause a system alignment to the low or high side of the rocking curve.

During data acquisition for DEI the recorded values were VTF pulses from the $I_o$ channel and counting pulses from the NaI detector. The intensity correction was done by taking the maximum $I_o$ value in the pair of images divided by the $I_o$ value for the current bin times the NaI detector count for the current bin,

$$\text{Intensity Corrected Counts} = \frac{I_o^{max}}{I_o^i} \times N_{NaI}^i.$$

All of the following images were formed using IDL (ITT, Boulder, CO, USA).

**Scans 48 and 49**

The scan pair 48 and 49 were set to acquire at the half maximum points of the rocking curve on the high and low side respectively. Figure 9.16 shows the scans after correcting for intensity changes using $I_o$.



Figure 9.16: Left: the low angle side scan #49. Right: the high angle side scan #48.

In scan 48 on the high angle side of the rocking curve image refraction effects can be seen on the bottom of the acrylic rod as the brightens increases on the edge. In both the low and high angle side scans the cuvette containing only gelatin on the right hand side of the image causes less absorption than the other cuvettes containing the powder samples of Mn (left hand side) and Fe (middle) as expected. In scan 49 on the low angle side of the rocking curve the amount of brightness of the gelatin cuvette would indicate that the location on the rocking curve may have shifted away from the intended place on the rocking curve.

The absorption image from scans 48 and 49 using equation 4.9 is shown in figure 9.17

113
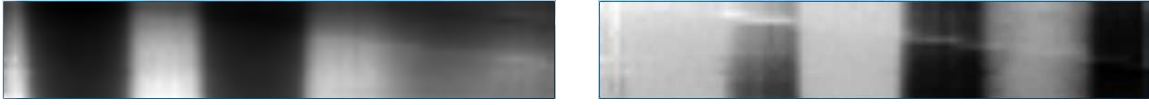
Figure 9.17: DEI images from #48 & 49. Left: Absorption image. Right: Refraction angle image.

on the left. The absorption image is as expected clearly showing three cuvettes with the gelatin control cuvette on the right hand side of the image slightly more bright than the other two. The diagonal acrylic rod can also be seen in the absorption image.
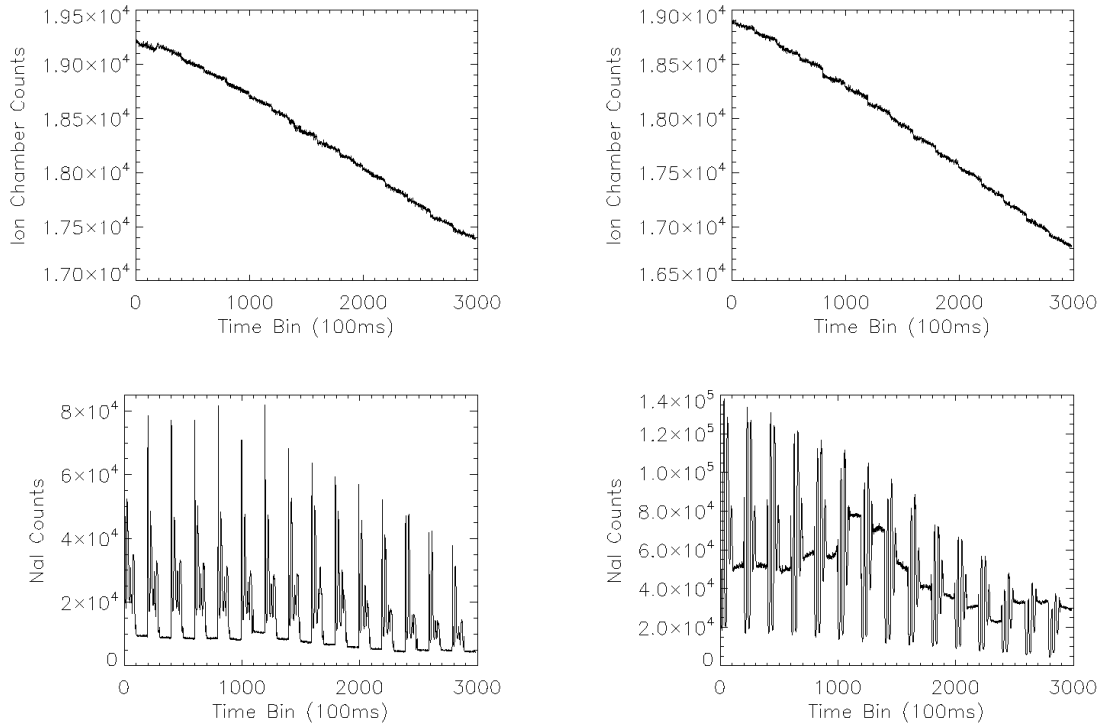


Figure 9.18: Left: The $I_o$ counts and the NaI detector counts for run 48. Right: The $I_o$ counts and NaI detector counts for run 49.

The refraction angle image from using equation 4.8 with scans 48 and 49 is shown in figure 9.17 on the right. The refraction angle image is not as expected for data collected on the half angle points. The cuvettes all appear bright in the image when they are not expected to be visible as they do not cause any refraction deviations in

114

the plane of the analyzer crystal, and refraction effects on the bottom of the acrylic rod appear more faint than in the high angle side image. This indicates: 1) that the system drifted and the difference of the low and high angle images did not cancel out as they should have in this region; 2) that the scatter from the powder sample broadened the rocking curve in this region enough so that there was more intensity than expected; or 3) both analyzer angle drift and contrast mixing between scatter and refraction occurred. A comparison with DEI images collected with a VHR-90 $18.7\mu m$ pixel size X-ray camera (Photonic Science Limited, East Sussex, UK) in figure 9.7 shows a similar effect of the powder filled cuvettes having some contrast, but not to the same extent as the pencil beam system. This indicates that both contrast mixing between USAXS and refraction occurred and drift in the system during scans 48 and 49 as well.
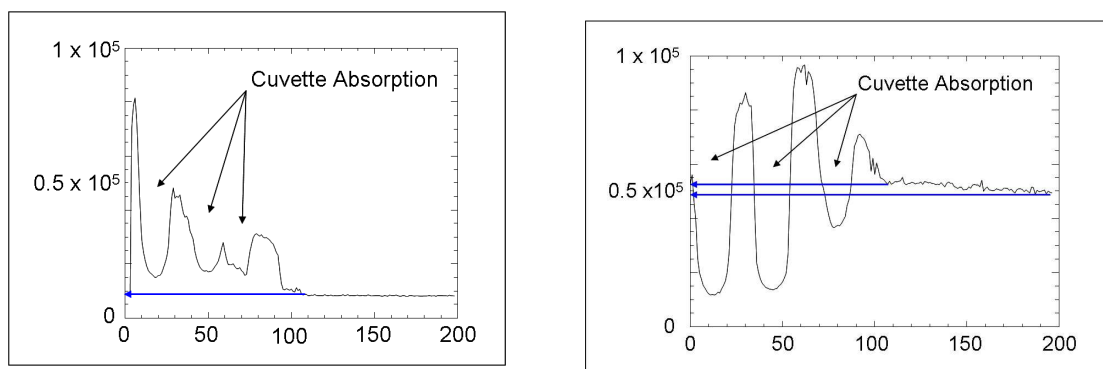


Figure 9.19: Left: A single image row from scan 48 with the XRP DEI system. The background counts after the cuvette scan is constant indicating no drift. Right: A single image row from scan 49 with the XRP DEI system. The background counts after the cuvette scan shows significant change indicating drift in the analyzer alignment.

To investigate the cause of the abnormalities in the absorption and refraction angle images the $I_o$ values and NaI detector counts for these scans were plotted and are shown in figure 9.18. The $I_o$ plots for both 48 and 49 show a steady uniform drop in

incident flux as expected for the decay of the ring current, but also shows that the BMIT monochromator feed back loop, which keeps the monochromator tuned at a fixed angle on the rocking curve, was functioning during the scans. The plots of the raw counting data from the NaI detector show peaks and valleys corresponding to the position of the cuvettes and the acrylic rod but also uniform area where there is no obstruction of the beam. These areas should remain constant and only vary slightly in value between lines in the raster scan corresponding to the storage ring decay. The NaI detector plot for 48 looks as expected with one unexplained feature from the sixth scan where an increase occurs in the unobstructed region. The unobstructed regions themselves are close to being horizontal lines and indicate a slowly changing flux (see figure 9.19). The NaI detector raw data for scan 49 has several features in the data and some of the unobstructed regions are not horizontal lines, but have significant slopes showing that the flux was changing (see figure 9.19). This indicates there was a change of position on the Laue analyzer rocking curve and explains the abnormalities observed in the refraction angle image.

**Scans 55 and 57**

The scan pair 55 and 57 were set to acquire at the one sixth of maximum points of the rocking curve on the low and high side respectively. Figure 9.20 shows the scans after correcting for intensity changes using $I_o$.
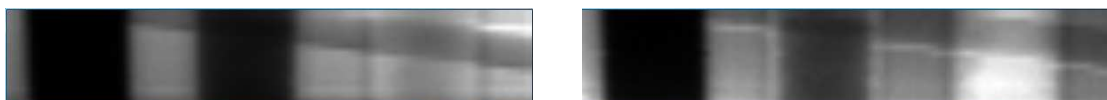


Figure 9.20: Left: the low angle side scan #55. Right: the high angle side scan #57.

In both scans refraction effects can be seen on the edges of the acrylic rod, on the upper edge for the low angle image, and on the lower edge for the high angle image.

116

The control cuvette at the right hand side of the image looks brighter than the other cuvettes in both images. There is an apparent mismatch in analyzer positions as the high angle side image shows the control cuvette very bright indicating more scatter contrast for this scan, which may occur from being further down the rocking curve than the low angle side scan setting. The calculated absorption and refraction angle images using equations 4.9 and 4.8 and are shown in figure 9.21 and all three cuvettes and the acrylic rod clearly visible. The dark over bright pattern visible on the acrylic rod in the refraction angle image is what is expected for refraction contrast as x-rays pass from a less dense material (air) into a more dense material (acrylic).
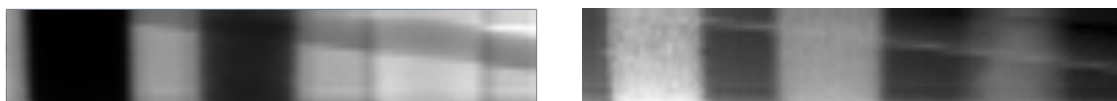


Figure 9.21: DEI images from #55 & 57. Left: Absorption image. Right: Refraction angle image.

The absorption and refraction angle images do have some artifacts in them with intensity variations over the area of the cuvettes and between the cuvettes. As with the previous scans a comparison to VHR-90 X-ray camera images are shown (see figure 9.6) and the $I_o$ and NaI detector raw data are plotted to look at the beam stability during these measurements (see figure 9.22). The $I_o$ plot for scan 55 shows that the monochromator feed back loop to keep it aligned was not functioning properly as the intensity goes through regions where it increases and decreases rather than following the storage ring decay. The $I_o$ plot for 57 shows a trend that does follow the storage ring decay, but also has a few small variations in intensity that should have been removed. These variations in intensity could not have produced all of the observed artifacts, as the size of the variations in the incident intensity are small.

The NaI detector data for scan 55 has variations in intensity evident between lines of the raster scan and the regions with the beam unobstructed are not horizontal, but several have positive or negative slopes. The data for scan 57 is similar showing intensity changes between raster scan lines and during individual lines. These changes explain the artifacts in the absorption and refraction angle images and indicates that the Laue analyzer crystal did not stay in the set position as seen before in the previous data set.
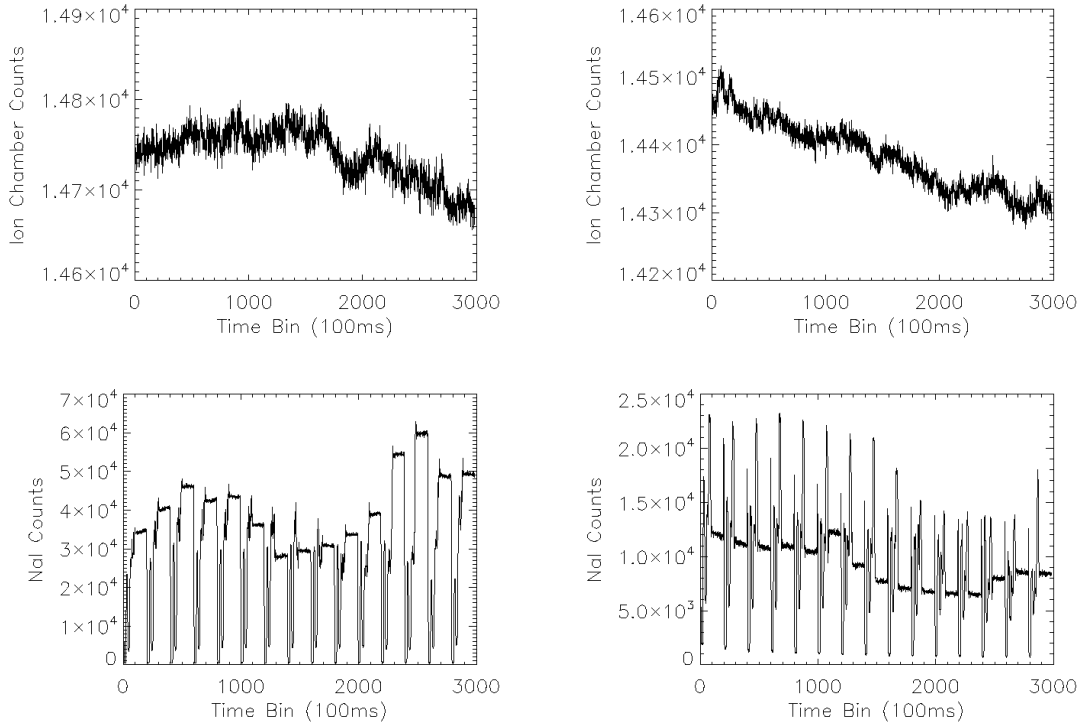


Figure 9.22: Left: The $I_o$ counts and the NaI detector counts for run 55. Right: The $I_o$ counts and NaI detector counts for run 57.

**Summary**

The system was able to acquire DEI images using the XRP and the Laue analyzer. The resulting images had artifacts in them due to drift in the alignment of the

118

Laue analyzer crystal and contrast mixing between USAXS and refraction from the powder sample. It is unlikely that the XRP would be responsible for the drift as several milliradians of motion are required for the XRP to have a significant impact on the position of the beam on the rocking curve. Reasons for drift of the Laue crystal alignment are: 1) thermal drift of the monochromator and a failure in the DCM feedback loop to keep the system stable; 2) vibration from the stepper motor driven raster scanning stages changing alignment; 3) mechanical instability in the rotation stage due to play in the joint allowing the orientation to drift slightly; or 4) weakening of the epoxy which mounts the crystal post to the stage allowing the crystal to change position slightly and unperceivable to the naked eye. The simple imaging tests did confirm however, that DEI imaging is possible with the XRP system and does not require the large space needed by tangent arm based systems.

# Chapter 10

# Conclusions and Future Work

In the following section the research goals and objectives for the project will be reviewed in brief and conclusions drawn from the information detailed in the previous chapters. Future work in the design and possible implementation of XRP imaging systems will be outlined.

## 10.1    Conclusions

X-ray imaging techniques require complex motion control, filter and shuttering, data acquisition, and data processing systems. An objective of this thesis project was to create such a system for use in combined x-ray imaging research programs. In Chapter 5 the description of such a system was presented for combined x-ray imaging using KES and FSI. This system allowed the successful completion of trial experiments for the GEMS research project [Bew08].

The feasibility of combining a DEI/MIR system with other x-ray techniques with preference to those that do not compete for the same photon flux signal was investigated in Chapter 6. Due to limitations on photon flux from a bending magnet source

at the CLS in the hard x-ray energy range as well as the small coherent scattering signal at these energies it was determined that WAXS was not a favorable candidate for use in the combined imaging system. Due to the findings in this chapter it was determined that fluorescence imaging would be a better match for the project's combined system.

For the proposed DEI/MIR imaging system a monochromatic beam would be needed. At a synchrotron facility the monochromatic beam is typically prepared by a Bragg orientation double crystal monochromator. In Chapter 7 the commissioning of the BMIT bending magnet monochromator and DEI apparatus was described. Before the use of the BMIT DEI system, which was needed to test the refraction deviations of the XRP, several tests were performed to ensure the proper operation of the components. This included imaging test objects at the top of the rocking curve and trial experiments on the human distal radius [Coo10].

The objective of replacing tangent arm crystal positioning systems by something less bulky, easy to position, with equal or better angular resolution, and compatible with other x-ray imaging techniques was realized with the invention of the XRP. The design of the XRP including constraints on building materials, absorption loss, refraction ranges, and geometry was presented in Chapter 8.1. Confirming that operation of the XRP agreed with the theoretical predictions for refraction deviations at angle positions to the incident beam was presented in Chapter 8.2. Using the XRP to improve upon the current DEI and MIR methods was another thesis objective and confirmation that the XRP could do so was presented in Chapter 8.3. By scanning through the rocking curve using the XRP enough points were collected to perform a Gaussian fit of the curve and directly determine the absorption, refraction, and

scattering values for three materials that previously would have been approximated using the DEI and MIR equations [Bew10].

The objective of testing the XRP in a DEI style imaging system combined with fluorescence x-ray imaging was presented in Chapter 9. The XRP was used to align the crystal position on the side of the rocking curve. The scans were taken in a traditional way with fixed XRP and analyzer angle for the high and low angle sides of the rocking curve. The same phantom that was imaged with the DEI system was also scanned by the fluorescence imaging component of the system. Due to instabilities in the beamline, monochromator drift caused artifacts to appear in the resulting DEI images, but proved the principle of XRP analyzer based imaging.

## 10.2 Future Work

To use the XRP method of analyzer crystal imaging to its full potential the system must be upgraded from the current form of using the prism as a replacement for the tangent arm crystal positioning system to a rapid scanning system where many rocking curve points are measured at each pixel in the image. Such a rapid XRP scanning system could take two different forms: 1) as a pencil beam scanning system using a tightly collimated high intensity beam where samples are raster scanned and the XRP rotated quickly to acquire the rocking curve data at each position; or 2) a line beam system with a segmented detector and wide XRP where biological samples could be rapidly scanned and some motion artifacts removed because all the necessary data to form the image is captured during one scan line by line. In either form of the system high resolution low backlash motion stages would be needed as well as fast counting or line reading detectors. For a pencil beam system a counting

detector would suffice with a multichannel scalar DAQ recording ion chamber values and the counts reaching the detector. In the case of a line beam XRP system the multichannel scalar DAQ would be needed as well as a segmented detector that can acquire many frames in millisecond time bins. Such an upgraded system could outperform current x-ray imaging techniques on living specimens.
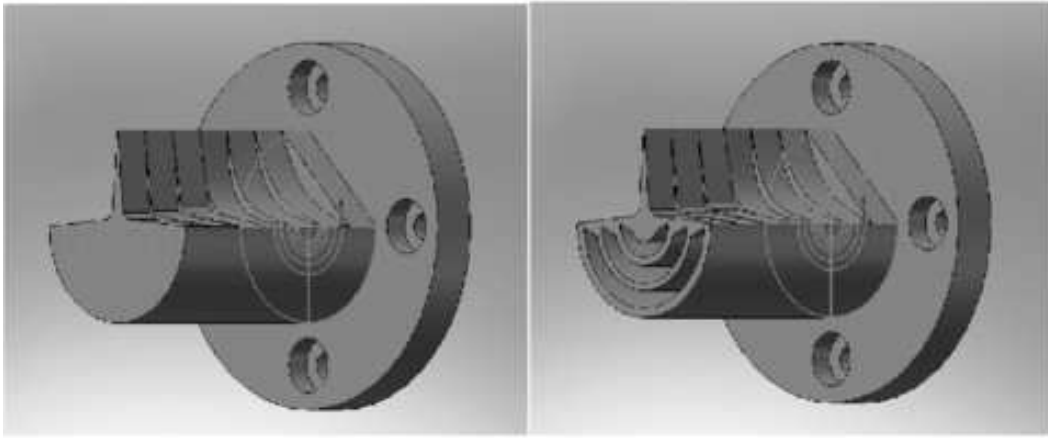


Figure 10.1: More advanced designs for XRPs with varying linear slopes and non-linear designs.

Other work for future investigation should focus on alterations of XRP design parameters. The choice of the beam height which determined the size and the curvature of the XRP was made due to the expected photon flux from a CLS bending magnet beamline at energies between 35-45 keV where low dose imaging of small animals would take place. If a narrower beam height could be used the thickness of the XRP and hence the absorption loss through it could be reduced substantially. The smaller beam height would also allow for non-linear surfaces where curvatures are used to deviate the beam so as to prolong the time spent on the low reflectivity areas of the rocking curve to acquire more data there and better counting statistics. Figure

10.1 shows two SolidWorks design drawings for an XRP intended for a narrow pencil beam. Every centimeter of length has a new XRP surface where the slope or curvature changes so that the desired profile can be selected. For the most extremely curved regions on this XRP the beam height would need to be in the 100-200 micron range so that all the photons are incident on a similarly curved region. Otherwise the photon beam would be spread out over a range of angles on the rocking curve. An additional absorption reducing design is to put circular voids in the XRP, which do not cause any unwanted refraction deviations (See figure 10.1). XRP designs could also be investigated which use refraction deviations at many surfaces to create the intended total refraction deviation required.
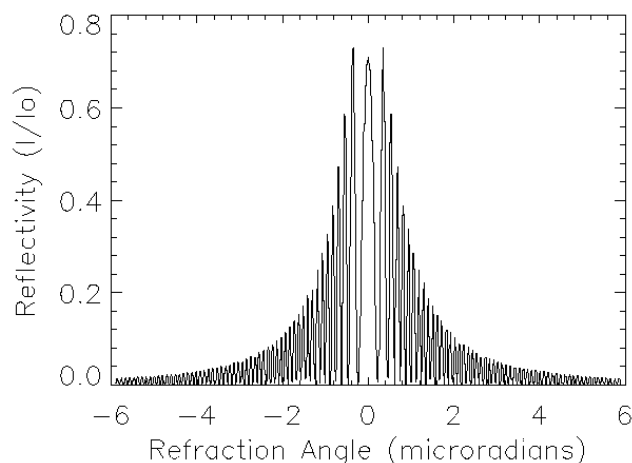


Figure 10.2: Reflectivity of a single 1mm thick Laue Si[4,4,0] crystal at 40keV.

For further research using the XRP system it would be desirable to replace the Laue analyzer crystal with a Bragg analyzer. This would remove the front back oscillations that occur in Laue diffraction (See figure 10.2), which may cause a distortion in the Gaussian fit of the rocking curve when absorption, refraction, and scattering parameters are being determined. The reason for using the Laue reflection to begin

with was to allow for more possible x-ray technique combinations and crystal pieces available. With Laue diffraction the transmitted beam through the object does not get removed so CT and KES imaging are possibilities. Due to the competition of these techniques for parts of the transmitted beam the quality of the resulting images will never be as high in quality as using the entire beam to form one image. It is therefore favorable to use x-ray techniques that do not compete for the same photon signal, in which case a Bragg analyzer crystal could replace the Laue analyzer.

# References

[Als01]  Als-Nielsen, Jens and Des McMorrow. "Elements of Modern X-ray Physics",
Wiley, Toronto, 2001.

[Bee65]  Beer, August. "Einleitung in die Elektrostatik die Lehre vom Magnetismus
und die Elektrodynamik." Druck und verlag von Friedrich Vieweg und Sohn,
Braunschweig, 1865.

[Bat06]  Batchelar, D.L., M.T. Davidson, W. Dabrowski, and I.A. Cunningham.
"Bone-composition imaging using coherent-scatter computed tomography"
Medical Physics 33 (2006), 904-915

[Bat64]  Batterman, Boris, and Henderson Cole. "Dynamical Diffraction of X-rays
by Perfect Crystals." Reviews of Modern Physics 36 (1964): 681-717

[Bew08]  Bewer, Brian, Honglin Zhang, Ying Zhu, Limei Zhang, Graham N. George,
Ingrid J. Pickering, and Dean Chapman. "Development of a combined K-edge
subtraction and fluorescence subtraction imaging system for small animals."
Review of Scientific Instruments 79 (2008): 085102

[Bew10]  Bewer, Brian, and Dean Chapman. "Development of an X-ray prism for
analyzer based imaging systems." Review of Scientific Instruments 81 (2010):
085108

[Bus02]  Bushberg, J, A Seibert, M Leidholdt, and J Boone. "The Essential Physics
of Medical Imaging." 2nd ed. Philadelphia: Lippincott Williams and Wilkins,
2002.

[Cha97]  Chapman, D, W Thomlinson, R Johnson, D Washburn, E Pisano, N Gmur,
Z Zhong, R Menk, F Arfelli, and D Sayers. "Diffraction Enhanced X-Ray Imag-
ing." Physics in Medicine and Biology 42 (1997): 2015-25.

[Cha98]  Chapman, D, E Pisano, W Thomlinson, Z Zhong, R Johnson, D Washburn,
D Sayers, and K Malinowska. "Medical Applications of Diffraction Enhanced
Imaging." Breast Disease 10.3,4 (1998): 197-207.

[Con05]  Connor, D.M, D. Sayers, D.R. Sumner, Z. Zhong. "Identification of fatigue
damage in cortical bone by diffraction enhanced imaging." Nuclear Instruments
and Methods in Physics Research A 548 (2005): 234-239

[Coo10] Cooper, David, Brian Bewer, Sheldon Wiebe, Tomasz Wysokinski, and Dean Chapman. "Diffraction enhanced X-ray imaging of distal radius: a novel approach for visualization of trabecular bone architecture." Canadian Association of Radiologists Journal, July 2010

[Cul56] Cullity, B.D. "Elements of X-ray Diffraction." Addison-Wesley Pub. Co., Reading, 1956

[Eld47] Elder, F.R., A.M. Gurewitsch, R.V. Langmuir, and H.C. Pollock. "Radiation from electrons in a synchrotron." Phys. Rev. 71, (1947), 829

[Har87] Harding, G, J. Kosanetzky, and U. Neitzel. "X-ray diffraction computed tomography." Medical Physics, 14 (1987), 515-525

[Hen02] Hendee, William, and E. Russell Ritenour. "Medical Imaging Physics : fourth edition." Wiley-Liss, New York, 2002

[Jam62] James, R.W. "The Optical Principles of the Diffraction of X-rays", Ox Bow Press, 1962

[Joh09] Johns, P.C., B.E. Bewer, and L.D. Chapman. "Initial Experiments in Monoenergetic X-ray Scatter Imaging at the BioMedical Imaging and Therapy facility of the Canadian Light Source." Proceedings of the 55th Annual Meeting of the Canadian Organization of Medical Physicists, Medical Physics 36, 4306

[Kis03] Kiss, M, D Sayers, and Z Zhong. "Measurement of Image Contrast Using Diffraction Enhanced Imaging." Physics in Medicine and Biology 48 (2003): 325-40.

[Kit86] Kittel, Charles. "Introduction to Solid State Physics : sixth edition." John Wiley and Sons, Toronto, 1986

[Li04] Li, J, Z Zhong, R Lidtke, K Kuettner, C Peterfy, E Aliyeva, and C Muehleman. "Radiography of Soft Tissue of the Foot and Ankle with Diffraction Enhanced Imaging." Journal of the American Podiatric Medical Association 94.3 (2004): 315-22.

[Mue04] Muehleman, C, S Majumdar, A Issever, F Arfelli, R Menk, L Rigon, G Heitner, B Reimes, J Metge, A Wagner, K Kuettner, and J Mollenhauer. "X-Ray Detection of Structural Orientation in Human Articular Cartilage." Osteoarthritis and Cartilage 12 (2004): 97-105.

[Nob67] "Nobel Lectures." Physics 1901-1921. Amsterdam: Elsevier Publishing Company, 1967

[Opp05] Oppelt, Arnulf. "Imaging Systems for Medical Diagnostics." Siemens & Publicis Corporate Publishing, Erlangen, 2005

[Pis00]  Pisano, E, R Johnson, D Chapman, J Geradts, M Iacocca, C Livasy, D Washburn, D Sayers, Z Zhong, M Kiss, and W Thomlinson. "Human Breast Cancer Specimens: Diffraction Enhanced Imaging with Histologic Correlation-Improved Conspicuity of Lesion Detail Compared to Digital Radiography." Radiology 214 (2000): 895-901.

[Rig02]  Rigon, Luigi, Zhong Zhong, Fulvia Arfelli, Ralf-Hendrik Menk, and Alessandra Pillon. "Diffraction Enhanced Imaging Utilizing Different Crystal Reflections at Elettra and NSLS." Proceedings of SPIE, Vol. 4682 (2002)

[Rig07]  Rigon, Luigi, Fulvia Arfelli, and Ralf-Hendrik Menk. "Three-image Diffraction Enhanced Imaging Algorithm to Extract Absorption, Refraction, and Ultrasmall-angle Scattering." Applied Physics Letters 90 (2007) : 114102

[Ron96]  W. Röntgen. "On a new kind of rays." Nature, 53 (1896), 274-276

[Tho01]  Thompson, Albert : Editor. "X-ray Data Booklet". Lawrence Berkeley National Laboratory, Berkeley, CA, USA (2001)

[Wer03]  Wernick, Miles N, Oliver Wirjadi, Dean Chapman, Zhong Zhong, Nikolas P Galatsanos, Yongyi Yang, Jovan G Brankov, Oral Oltulu, Mark A Anastasio and Carol Muehleman "Multiple-image radiography." Physics in Medicine and Biology, 48 No 23 (2003), 3875-3895

[Zac45]  Zachariasen, W.H. "Theory of X-ray Diffraction in Crystals", John Wiley, 1945

[Zho00]  Zhong, Z."Using a prism to reject or select harmonic reflections in an X-ray monochromator." Journal of Applied Crystallography, 33 (2000), 1082-1087